Astronomy Reports, Vol. 47, No. 8, 2003, pp. 621–636. Translated from Astronomicheskiĭ Zhurnal, Vol. 80, No. 8, 2003, pp. 675–691.

Light Curve Interpretation for "Quiescent" X-ray Novae in a Model with Noncollisional Interaction between the Flow and Disk. The System GU Mus = GRS 1124–68

T. S. Khruzina[1], A. M. Cherepashchuk[1], D. V. Bisikalo[2], A. A. Boyarchuk[2], and O. A. Kuznetsov[2,3]

[1] *Sternberg Astronomical Institute, Universitetskiĭ pr. 13, Moscow, 119992 Russia*

[2] *Institute of Astronomy, Russian Academy of Sciences, ul. Pyatnitskaya 48, Moscow, 119017 Russia*

[3] *Keldysh Institute of Applied Mathematics, Russian Academy of Sciences, Miusskaya pl. 4, Moscow, 125047 Russia*

Received March 5, 2003; in final form, March 14, 2003

Abstract—We have analyzed optical and infrared light curves of GU Mus obtained during the system's quiescent state and carried out computations for "hot-line" and "hot-spot" models. The hot-line model describes the optical variability of GU Mus better than the hot-spot model. Season-to-season variations of the shape, amplitude, and mean levels of the optical and infrared light curves of GU Mus are due to changing parameters of the hot line and, to a lesser degree, of the accretion disk. Taking into account the contribution of the variability of the disk + hot line system to the variability of the system as a whole, we are able to reliably estimate the orbital inclination, $i = 54^\circ \pm 1\overset{\circ}{.}3$, and the mass of the black hole, $M_X = (6.7\text{–}7.6)\,M_\odot$.

1. INTRODUCTION

Among the numerous stellar X-ray sources, there exists a small group of stars whose members exhibit characteristic X-ray variations in which their X-ray luminosity increases by a factor of several hundred thousand within days, after which the luminosity returns to its original value over several months (cf., for example, [1, 2]). This behavior strongly resembles the light curves of classical novae, leading to these variable X-ray sources being named "X-ray novae." Subsequent optical observations of these objects have confirmed the novalike character of their outbursts.

Spectroscopic observations of such objects demonstrate that they were binaries, like classical or dwarf novae. The secondary, whose light dominates in the optical during quiescence, is usually a main-sequence star, subgiant, or even late-type giant. In contrast to the primaries of classical novae, which are white dwarfs, the primary is now a neutron star or black hole. Consequently, most of the gravitational energy released during accretion is emitted in the X-ray. More detail on the physics of X-ray novae can be found in the reviews [3–6] and the recent monograph [7].

The X-ray outbursts are accompanied by optical outbursts due to X-ray heating of the accretion disk and optical star, making it possible to identify X-ray novae very reliably. At the same time, the quiescent optical spectra of X-ray novae contain absorption lines of the optical star, enabling measurement of their mass function and estimation of the mass of the relativistic object (cf., for instance, the reviews [8, 9]).

During quiescence, the luminosity of the optical star is comparatively low. When interpreting the optical light curves of X-ray novae, it is necessary to take into account the effect of the optical star's ellipsoidal shape, the contribution of the accretion disk's radiation, and variability due to the contribution of light from the region where the disk interacts with the gas flow. The three-dimensional gas-dynamical computations of gas flows in interacting binary systems [10–13] have demonstrated that, in self-consistent flow models, the major region of energy release is located outside the disk, in a shock wave due to interaction of the flow with matter of the circumstellar envelope; this is the "hot-line" model. Application of the hot-line model to the interpretation of the optical and infrared light curves of dwarf novae [14–16] have illustrated its advantages over hot-spot models.

The current study is aimed at analyzing the light curves of the X-ray nova GU Mus in quiescence using the hot-line model.

1063-7729/03/4708-0621$24.00

2. GENERAL INFORMATION ABOUT THE X-RAY NOVA GU Mus

The X-ray nova Muscae 1991 GU Mus = XN Mus 1991 = GS 1124−683 = GRS 1124−68) was independently discovered in sky surveys by the GRANAT and GINGA space telescopes on January 9, 1991 [17, 18]. Four days later, it was identified with an optical star ($V = 13^m.0$) located near the X-ray source [19]. After another several days, the flux from the system had decreased to $V \sim 13^m.4$, and it had decreased to its pre-outburst level, $V \sim 20^m.5$, in about a year.

Remillard *et al.* [20] acquired photometric and spectroscopic observations of GU Mus at 4900−6500 Å and in the I filter 15 months after the outburst, when the system had returned to quiescence ($V \sim 20^m.5$). The spectrum appeared to correspond to a K0−K4V star. The half-amplitude of the secondary's radial-velocity curve exceeded 400 km/s ($K_2 = 409 \pm 18$ km/s). From the radial-velocity curve, Remillard *et al.* [20] determined the system's orbital period ($P_{orb} = 0^d.43325(58)$) and computed the mass function of the compact object, $f(M) = 3.07 \pm 0.40\ M_\odot$. The spectrum of the nova reveals broad Hα and Hβ emission lines, testifying to the presence of an accretion disk around the compact object in the quiescent state. The full widths at half maximum of the Balmer lines reach 1500−2500 Å. Both the line intensities and profiles vary in time, and the line profiles are asymmetric.

In both filters, the system's light curve forms a double wave during the orbital period. The brightness minima coincide with the transitions of the radial velocity of the optical star through the γ velocity, providing evidence for the dominance of ellipsoidal variability of the K star in the optical variations. The I light curve is fairly symmetric, with the variation amplitude being lower than in V ($\Delta I \sim 0^m.15$).

The V light curve is characterized by a higher variability amplitude and appreciably unequal maxima at the quadratures, with the system being brighter at phase $\varphi \sim 0.25$.

Antokhina and Cherepashchuk [21] interpreted the more symmetric I light curve of GU Mus in a standard X-ray binary model with a thin accretion disk around a relativistic object [22], with the disk's radius being ∼0.6 of the maximum size of the Roche lobe of the primary (compact object). They demonstrated that the orbital inclination i showed a weak dependence on the component-mass ratio over a wide range of $q = M_1/M_2$. However, it is not possible to derive a reliable mass ratio for the system solely based on the shape of the infrared light curve. They estimated the lower limit for the orbital inclination $i > 39°$. They also were not able to adequately describe the V light curve's shape and amplitude using this standard model.

Based on observations of GU Mus three years after its outburst, Orosz *et al.* [23] improved the values found in [20] for the system's orbital period ($P_{orb} = 0^d.4326058(31)$), the half-amplitude of the secondary's radial-velocity curve ($K_2 = 406 \pm 7$ km/s), and the compact object's mass function ($f(M) = 3.01 \pm 0.15\ M_\odot$). According to this study, the secondary is a K3−K5 main-sequence star. After subtracting the standard spectrum of a K5V star from the total spectrum, the disk spectrum shows strong Balmer, HeI, and FeII emission lines against a flat continuum. The light-curve modeling of Orosz *et al.* [23] using an ellipsoidal-variability model could not fit the unequal light-curve maxima or the depth of the minimum corresponding to the upper conjunction of the optical star. Based on the absence of eclipses of the disk in the system, Orosz *et al.* [23] estimated the upper limit for the orbital inclination $i_{\max} \sim 65°$. A lower limit was estimated from the minimum amplitude of the V light curve, $i_{\min} \sim 54°$. For the mass ratio $q = M_1/M_2 = 6.5$−8.8, the mass of the primary will be $M_1 \sim 5.0$−$7.5\ M_\odot$.

Casares *et al.* [24] observed the Hα line in the spectrum of GU Mus, confirmed that the secondary has spectral type K3−K4V, and demonstrated that the secondary contributed 85−88% of the integrated R flux. Based on the rotational broadening of the photospheric absorption lines together with the $v \sin i$ value obtained for the secondary with limits based on the system's geometry, they estimated the component-mass ratio to be $q = 7.5$−8.1. They also present Hα Doppler tomography maps revealing a considerable flux from the secondary, probably related to the star's chromospheric activity, with the flux from the hot spot being absent or weak.

Shahbaz *et al.* [25] analyzed the H light curve of GU Mus to derive the orbital inclination $i = 54° \pm 15°$, distance $d \sim 2.8$−4 kpc, and mass of the compact object $M_1 \sim (4$−$11)\ M_\odot$.

Gelino *et al.* [26] acquired infrared light curves of GU Mus in the J and K bands and analyzed their J and K light curves using the code of Wilson and Devinney [27], without taking into account the accretion disk around the compact object or the hot spot. These computations considered only the ellipsoidal variability of the secondary, which was taken to be slightly evolved, since a normal K4V star does not fill its Roche lobe. However, the secondary cannot be a giant: in this case, the star's size would be larger than the orbit corresponding to the orbital period of $0^d.43$. Their analysis of the J and K light curves confirmed the conclusion of Antokhina and Cherepashchuk [21] that the model light curves were fairly insensitive to

input parameters such as the component-mass ratio, the limb darkening and gravitational-darkening coefficients, and the effective surface temperature of the secondary. An exception is the orbital inclination, for which Gelino *et al*. [26] found the best-fit value $i = 52°–56°$. Taking into account additional sources of radiation in the system (the disk and hot spot) increases the admissible orbital inclination by $\sim 4°$. They estimated the mass of the compact object to be $M_1 = 6.95 \pm 0.6\ M_\odot$; the corresponding distance to the system is $d \sim 5.1$ kpc.

3. THE MODEL OF THE SYSTEM

The light curves of GU Mus obtained by various authors show a significant light excess near quadrature, $\varphi \sim 0.25$, which cannot be reproduced in the standard models (phase $\varphi = 0.0$ corresponds to upper conjunction of the compact object). Such models likewise cannot reproduce the deeper minimum at phase $\varphi \sim 0.0$. Heating of the secondary by X-rays from the compact source, which could make the minimum at phase $\varphi \sim 0.5$ shallower, is not strong in this system. For the distance $d \sim 5$ kpc, the X-ray luminosity of the source in its low state does not exceed $L_X < 1.5 \times 10^{32}$ erg/s, but no more accurate value is known. The bolometric luminosity of the optical K3–5V star is $\sim (6–9) \times 10^{32}$ erg/s, so that the ratio of the components' bolometric luminosities is $L_X/L_{\rm opt} \leq 0.2$. The secondary can also receive some fraction of the hot ultraviolet radiation from the inner parts of the disk if this radiation propagates symmetrically. The ultraviolet light could be invisible to an observer on Earth due to absorption in the circumstellar envelope and interstellar medium. However, if the angular distribution of the X-ray flux is not uniform, as is characteristic of black holes [28], the heating of the secondary by this radiation will remain insignificant. In addition, considerable heating of the secondary would lead to variations of the star's spectral type with orbital phase, which are not observed.

To compute the theoretical light curve and derive the X-ray nova's parameters, we used a mathematical model taking into account the contribution of the additional radiation from the shock wave outside the accretion disk. The radiation of this shock is strongest at phase $\varphi \sim 0.25$, but, depending on the conditions for its radiative cooling, it may also be observed at phases $\varphi \sim 0.75$. We successfully used this model earlier in our analysis of light curves of cataclysmic variables [15]. Below, we briefly describe its main features; a more detailed description of the model can be found in [15, 29].

(1) The donor star (secondary) completely fills its Roche lobe.

(2) We take into account the tidal and rotational distortion of the secondary.

(3) The surface of the secondary is subdivided into 648 area elements, and the intensity of the radiation emitted toward the observer is computed for each, taking into account gravitational darkening and limb darkening (applying a nonlinear limb-darkening law). We consider occultations of the area elements on the star by the body of the star itself and by the bodies of all the components of the system. When allowing for the effects of heating of the stellar surface by hot radiation from inner regions of the disk, we use two models, with isotropic and anisotropic angular flux distributions. It was demonstrated in [30] that, for disk accretion onto a neutron star, the star's rotation makes the propagation of radiation from this central source isotropic; i.e., this radiation will not be attenuated in the orbital plane of the system. In the case of a black hole, there is no such central source, and the radiation flux from the flat surface of the accretion disk possesses considerable anisotropy, leading to reduced heating of the companion. However, due to a number of instabilities that accompany high accretion rates [31], the inner parts of the disk can become more spherical, making the radiation from the accretion disk more isotropic. Note that the accretion rates during the quiescent states of X-ray novae are probably low, making it unlikely that the inner parts of the accretion disk become more spherical. The central parts of an advection-dominated disk become spherical due to the high ion temperature [32, 33].

(4) The primary is spherical in shape and is located at a focus of the elliptical accretion disk. Since the compact object is small, we assume when analyzing the light curves of X-ray novae that its optical and infrared luminosities are negligible and do not contribute to the combined flux of the system.

(5) The elliptical (eccentricity e) accretion disk is represented as follows. The lateral (or outer) surface of the disk is an ellipsoid with semi-axes a, b, and c. The semi-axes a and b are in the orbital plane, so that $b^2 = a^2(1 - e^2)$; the semi-axis c is orthogonal to the orbital plane. The center of the primary is at a focus of the ellipsoid.

The disk's orientation is determined by the angle α_e between the radius vector from the center of the compact object to the disk periastron and the line connecting the components of the close binary. The value of α_e can vary from 0 to 2π and increases in the direction of the components' orbital motion. A detailed description of the procedure used to model a thick, elliptical accretion disk was presented in [34].

The temperature of an area element on the disk surface depends on the distance r between its center and the compact object. We assume that the temperature of disk areas near the black hole are equal to the

temperature T_b of the first inner orbit located near the equator at the distance R_1 from its center. Variations of the disk temperature are usually represented by the relation [28]

$$T(r) = T_b \left(\frac{R_1}{r}\right)^{\alpha_g}, \quad (1)$$

assuming that the gravitational energy released during the accretion is balanced by radiative cooling. As a first approximation for the parameter α_g, the value $\alpha_g = 0.75$ [28] is usually used, which corresponds to assuming that each point of the disk's surface emits as a black body. However, observations show that the radial temperature distribution is often flatter than for the canonical case, leading to higher temperatures. Heating of the disk's outer regions by radiation from the secondary increases its temperature only slightly, but the model also takes this into account. The outer boundaries of the disk can also be heated by high-temperature radiation from its inner regions. This effect is significant only when this radiation propagates isotropically; in this case, it also heats the secondary. If high-temperature radiation with luminosity L_b from the inner regions of a classical accretion disk propagates anisotropically, the flux L reaching the surface of the secondary varies according to the relation [30]

$$\frac{dL}{d\Omega} = \frac{L_b \cos\theta(1 + u_b \cos\theta)}{2\pi\left(1 + \frac{2}{3}u_b\right)}. \quad (2)$$

Here, the limb darkening in the accretion disk has been included in a linear approximation, θ is the angle between the normal to the disk's surface and the direction of the solid-angle element $d\Omega$, and u_b is the limb-darkening coefficient of the disk. For the case of isotropic flux propagation, this simplifies to

$$\frac{dL}{d\Omega} = \frac{L_b}{4\pi}. \quad (3)$$

(6) The hot line along the flow is described using part of an ellipsoid with semi-axes a_v, b_v, and c_v elongated toward the inner Lagrangian point, L_1. The lateral surface of this ellipsoid coincides with the tangent to the elliptical disk for all disk orientations, and its center is in the orbital plane in the disk, at some distance from its edge. Only that part of the ellipsoid outside the accretion disk is considered to be the hot line. The procedure used to construct the shape of the hot line and the technique used to synthesize the light curve of a close binary in the framework of the model used are described in [29].

The release of the shock energy occurs at the surface of the hot line, both at the shock front (i.e., on the side of the approaching flow, or the "windward side") and on the opposite ("leeward") side, depending on the physical parameters of the interacting flows (their velocities, densities, etc.). Areas on the surface of the hot line are assumed to radiate according to a Planck law, which means the hot line adjacent to the accretion disk is considerably opaque. We compute the temperature of an area element on the surface of the hot line independently for both its sides, in accordance with the relation

$$T_i(y) = T_d + T_0 \cos(0.5\pi\Delta y_i), \quad (4)$$
$$\Delta y_i = \frac{y_i - y_{\max}}{y_{\min} - y_{\max}},$$

where T_d is the temperature matter would have at the distance r from the compact object according to Eq. (1). At the point with the coordinate $y_{\max}$, the temperature of the matter in the hot line, $T_i(y)$, has the largest increment, $T_{\max}(y) = T_d + T_0$, and, at the point with $y_{\min}$, the temperature increment is equal to zero, and the temperature of the matter is $T_i(y) = T_d$. When $y_{\min}$ and $y_{\max}$ are close to each other, the energy release from the shock occurs in a small region resembling a hot spot, but located not on the disk but instead on one part of the hot-line surface, with its other parts remaining comparatively cool. It is assumed that the temperature on the windward side of the hot line reaches its highest value, $T_{\max}$, at the point of contact between the flow and the lateral surface of the disk. The highest temperature of the hot line on the leeward side is displaced to the point with

$$y^{(2)}_{\max} = y^{(1)}_{\max} - dy,$$

with the displacement dy being a free parameter of the problem, $dy > 0$. Here, the superscripts (1) and (2) refer to the windward and leeward sides of the hot line, respectively.

The model parameters we wish to estimate are $q = M_1/M_2$, i, T_2, and T_b; the disk eccentricity e and semi-major axis a; the parameter α_g determining the profile of the temperature variations across the disk surface; the azimuth of the disk's periastron α_e; the parameter A_p determining the thickness of the disk's outer edge; the semi-axes of the ellipsoid describing the ellipsoidal part of the hot line a_v, b_v, and c_v; the highest temperatures on the surface of the hot line near the outer edge of the disk at its windward side, $T^{(1)}$, and leeward side, $T^{(2)}$; and the parameters $y_{\min}$ and dy described above. Thus, there are a total of 16 parameters; however, we were able to fix some of these (cf. Section 4).

(7) We searched for the parameters best describing the system's mean light curve using the Nelder–Mead method [35]. When searching for the global minimum of the residual for each of the curves, we applied several dozen different first approximations, due to the large number of independent variables,

which typically leads to the existence of a number of local minima in the studied parameter range. We estimated the quality of the fit between the theoretical and observed light curves using the residual

$$\chi^2 = \sum_{j=1}^{n} \frac{(m_j^{theor} - m_j^{obs})^2}{\sigma_j^2}, \qquad (5)$$

where m_j^{theor} and m_j^{obs} are the object's theoretical and observed magnitudes at the jth orbital phase, σ_j^2 is the dispersion of the observations for the jth data point, and n is the number of normal points in the curve.

4. RESULTS OF LIGHT-CURVE MODELING FOR GU Mus

We determined the parameters of GU Mus using two models. The first assumed isotropic propagation of the X-ray and high-temperature ultraviolet radiation from inner parts of the disk. In the second, we allowed for angular anisotropy of the propagation of this radiation.

As noted in Section 3, the reason for the anisotropy of the X-ray radiation from the inner parts of a classical accretion disk is that, in the case of a black hole, the flat inner part of the disk radiates similarly to a thin stellar atmosphere. In this case, the radiation intensity is highest along the normal to the surface and decreases rapidly with deviation from the normal direction. In addition, due to the effect of projection, the radiating area of the flat disk surface also decreases with deviation from the normal direction. According to [28], this leads to a strong angular dependence for the X-ray intensities of accreting black holes [cf. Eq. (2)].

Light curves used. We used three groups of light curves of GU Mus to determine its parameters. The first consists of light curves acquired in white light (effective wavelength $\lambda \sim 5000$ Å) in 1992–1995 (designated BV, cf. Figs. 1, 2), and the second group are I curves ($\lambda_{eff} = 9000$ Å) acquired in 1992 and 1993. The BV and I observations are presented graphically in [23]. The 1992 light curves for BV and I are also described in detail by Remillard *et al.* [20]. The mean BV and I light curves are shown in Figs. 1–3. All these observations correspond to the system's low state, but comparison of the mean fluxes shows that GU Mus was $\sim 0^m.2$ brighter during 1993–1994 than in 1992 or 1995. The light-curve shape varies from season to season; the relative height of the brightness maxima at the quadratures in 1993–1995 was opposite to that observed in 1992. Both the absolute and relative depths of the brightness minima vary in both filters. We can see that the modulation amplitude and the difference between the maxima of the light curve at the quadratures increase with decreasing wavelength, especially for the 1992 season. The phase $\varphi = 0.0$ corresponds to the upper conjunction of the compact source. The I light curves are more symmetric due to the lower contribution of the accretion disk and possibly of the shock, since the optical star is, on average, cooler than the disk.

The third group of light curves we used are the J, K light curves of GU Mus presented by Gelino *et al.* [26], which were also acquired during the system's low state, on February 20 and 21, 2000.

The number of normal points n used to fit the shape of the mean BV, I, J, and K light curves of GU Mus are presented in the table, along with the corresponding critical $\chi^2_{0.01,n}$ values for the $\alpha = 0.01$ significance level; thus, the probability that the actual parameters of the system are outside the ranges derived from our light-curve analysis does not exceed 1%. Since the nature of the X-ray and ultraviolet heating of the optical star remains unclear, we analyzed the light curves independently for the cases of isotropic and anisotropic radiation from the inner regions of the accretion disk.

Optical light curves of 1992–1995. When constructing the theoretical light curves, we computed the radiation fluxes from the system's components, $F(X, \varphi)$, for a given set of parameters X and a sequence of orbital phases, φ. The resulting $F(X, \varphi)$ values are expressed in relative units. These can be converted into commonly used units (referring to a unit wavelength interval) using the expression $f = Fa_0^2 \times 10^{-12}$ [erg s^{-1} cm^{-3}], where a_0 is the distance between the centers of mass of the stars in centimeters. When interpreting individual light curves, during the construction of a trial theoretical curve, we usually used the flux at the first quadrature corresponding to the given trial curve to convert the computed radiation fluxes to magnitudes. For comparison with the observed light curve, we initially shift the computed trial light curve to achieve the best agreement between the observed and computed radiation fluxes (in magnitudes) at the first quadrature. The subsequent comparison of the observed and synthesized light curves uses the χ^2 criterion.

Since the number of model variables could be as high as 16, it is necessary to use additional information to choose the most probable solutions from the large number of sets of admissible parameters obtained from the light-curve fitting. This includes spectroscopic information about the mass ratio of the close-binary components, as well as data on the red dwarf's contribution to the combined radiation flux during the studied observing period. Information on the red dwarf's contribution to the combined flux is

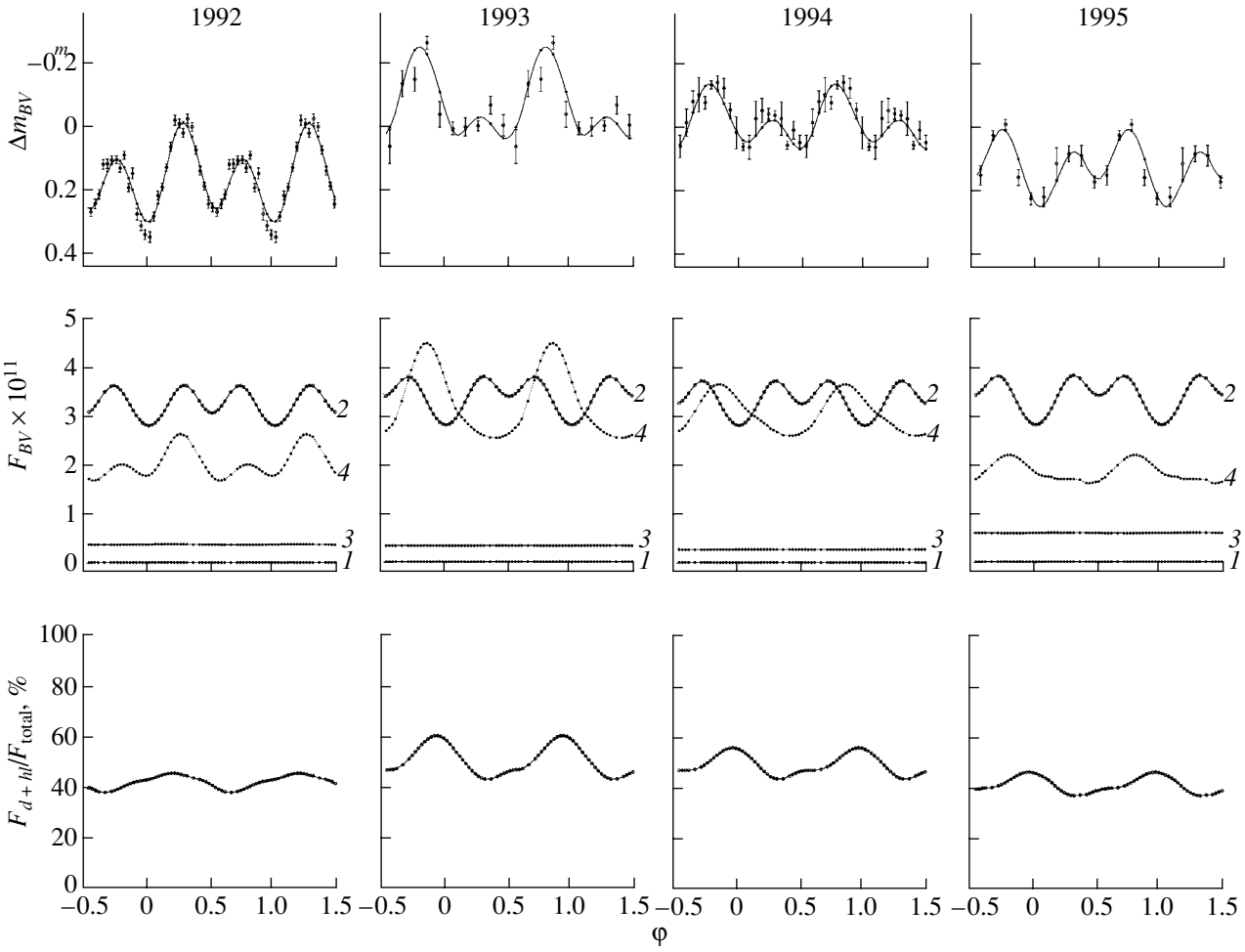

Fig. 1. Computational results for the model with isotropic radiation from the inner parts of the accretion disk. The upper panels show 1992–1995 observations of GU Mus in the optical ($\lambda = 5000$ Å; points with corresponding error bars) and theoretical curves (solid) computed using the parameters given in the table. The middle panels show the contributions of the (*1*) compact object (equal to zero in both models), (*2*) red dwarf, (*3*) elliptical accretion disk, and (*4*) extended hot line to the combined flux. The bottom panels show the relative contribution of the nonstellar radiation sources (disk and hot line) to the combined flux from the system.

very limited. According to the spectroscopic observations of Orosz *et al.* [23] obtained in 1993, the contribution of the secondary to the combined BV flux was 46–48%, with the corresponding contribution of the nonstellar sources of radiation being 52–54%. The luminosity of GU Mus was lower in 1992 due to the decreased flux from the nonstellar components; as a result, the relative contribution of the red dwarf's light to the total flux increased to 55–61%. This estimate of the contribution of the optical star to the combined flux was obtained using the standard approach: the equivalent widths of the stellar absorption lines for the binary were compared to the equivalent widths of the absorption lines in the spectrum of a standard star, which is a single star of a similar spectral type and luminosity class.

When searching for the parameters of the GU Mus components for different observing seasons, we expressed all four observed BV light curves ($\lambda_{eff} \sim 5000$ Å) in magnitude differences, Δm_{BV}, relative to the system's magnitude at phase $\varphi = 0.25$ ($m_{BV} = 20^m.3684$) for the 1993 light curve (this light curve's number is $N = 2$):

$$\Delta m = m_N^{obs}(\varphi) - m_2^{obs}(\varphi) = -2.5 \log \left(\frac{F_N^{obs}(\varphi)}{F_2^{obs}(0.25)} \right).$$

In other words, this flux, in magnitudes, was used as a unified energy unit for all other observed light curves. Thus, all the 1992–1995 observations were reduced to the same zero point, corresponding to the observed flux at the first quadrature of the 1993 light curve. This approach enabled us to estimate variations of the system's luminosity from one light curve to another for each phase and to use both the light-curve shape

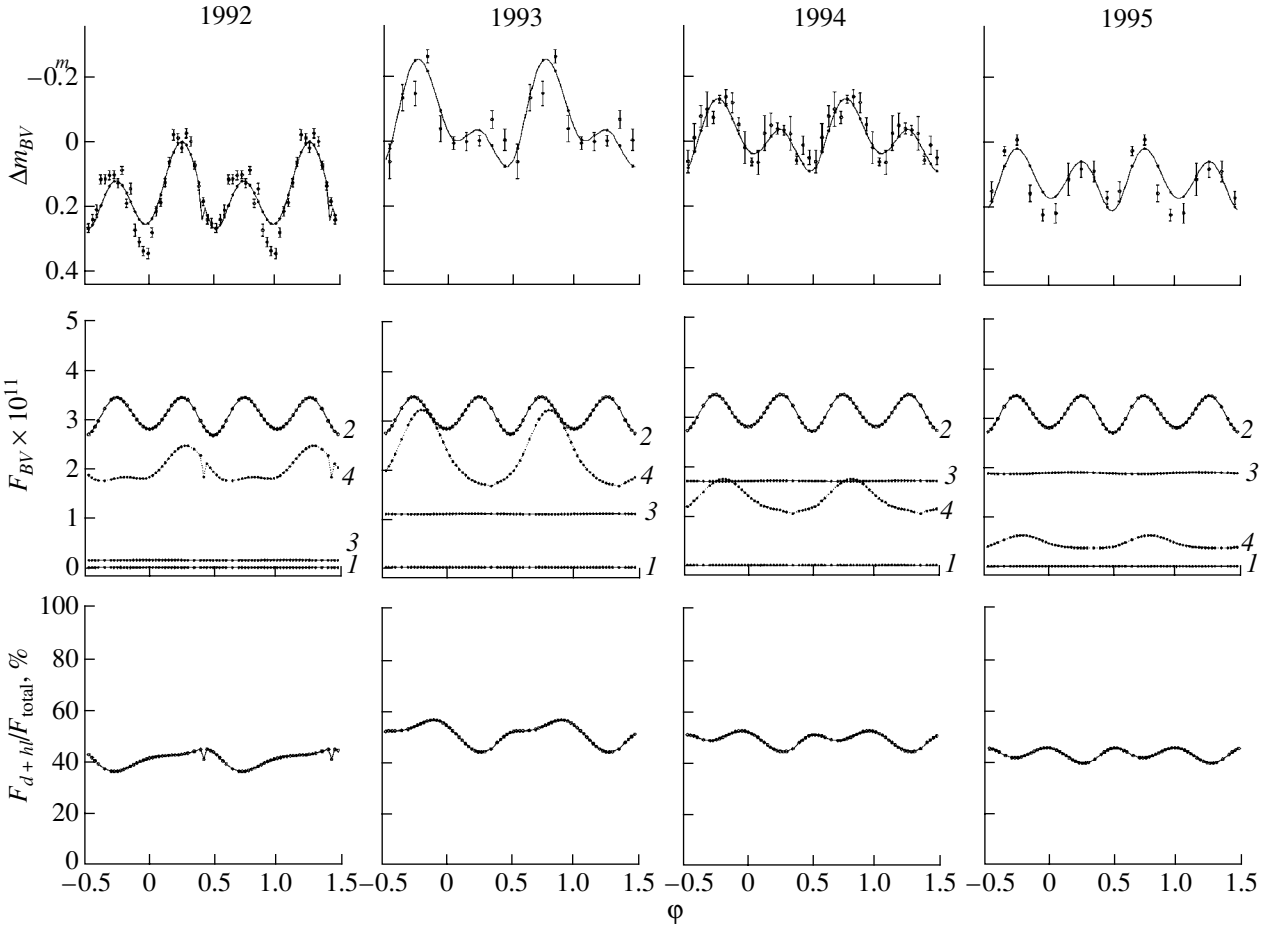

Fig. 2. Same as Fig. 1 for the model with anisotropic radiation from the inner parts of the accretion disk.

(as in the analysis of the individual light curves) and changes of the mean flux levels when comparing with the synthesized curves.

Thus, we constructed the Nth trial theoretical light curve in magnitudes by converting the theoretical fluxes, $F_N^{th}(X,\varphi)$, computed in the model into magnitudes, $\Delta m_N^{th}(X,\varphi)$, using the flux at the first quadrature for the same theoretical curve that best fitted the observed light curve with $N=2$, $F_2^{th}(0.25)$. In other words, the theoretical magnitude at phase φ for the Nth light curve will be

$$\Delta m_N^{th}(\varphi) = -2.5\log\left(\frac{F_N^{th}(\varphi)}{F_2^{th}(0.25)}\right).$$

The number of unknown parameters was largest in the first stage of solving for the parameters of GU Mus using each of the studied BV light curves. In the second stage of the analysis, we found the values of q, i, T_2 common to all the curves (close to the mean values). These parameters can be best determined from the J,K observations, because the star's optical light makes the highest contribution in these filters, but the normal points of the J,K light curves [26] have very high uncertainties, leading to a large range of admissible values for q and i. Therefore, when selecting the optimal q, i, T_2 values to fix, we used the parameters derived from the infrared light curves using the same weight as for the parameters derived from the BV light curves. We also fixed common values close to the mean parameter estimates for the disk's maximum radius (at apoastron), R_d/ξ (ξ is the distance between the center of mass of the compact object and the inner Lagrangian point, L_1), the thickness of the disk's outer edge β_d, the parameter α_g determining the radial temperature distribution in the disk, and the inner radius of the disk R_1 [this last parameter is needed to derive the radial temperature distribution of the disk; cf. (1)]. We then repeated the fit for the system's parameters for all four light curves fixing the parameter values $q = M_1/M_2 = 7.7$ (close to the spectroscopic estimate), $i = 54°$, $T_2 = 4500$ K, $R_1 = 0.0006a_0$, $R_d/\xi = 0.50$, $\beta_d = 1\overset{\circ}{.}8$, and $\alpha_g = 0.72$ for both the isotropic and anisotropic models.

Since we fixed the parameters of the secondary

Parameters of the components of GU Mus in 1992–2000, derived from the BV, I, J, K light curves in the hot-line model

Parameter	1992	1993	1994	1995	1992	1993	2000	2000
				"Isotropic" model				
n	30	10	20	10	25	10	29	22
$\chi^2_{0.01,n}$	50.9	23.2	37.6	23.2	44.3	23.2	49.6	40.3
Filter	BV				I		J	K
e	0.395	0.043	0.074	0.270	0.001	0.033	0.174	0.043
a/a_0	0.250	0.334	0.324	0.274	0.348	0.337	0.297	0.334
α_e, °	113.8	63.2	72.3	97.2	140.6	84.7	112.6	33.9
T_b, K	115255	133650	127340	134070	114800	132300	96935	97650
a_v/a_0	0.054	0.098	0.093	0.058	0.104	0.148	0.075	0.079
b_v/a_0	0.582	0.362	0.324	0.530	0.325	0.307	0.422	0.442
c_v/a_0	0.017	0.011	0.010	0.005	0.007	0.018	0.010	0.019
$T_{1*(\max)}$	10480	54850	15300	13210	6460	26505	15880	29670
$T_{2*(\max)}$	8500	30170	8985	11570	3195	14100	8150	12895
$\langle T_1 \rangle$	3620	2100	6480	2950	4565	5130	5245	19580
$\langle T_2 \rangle$	3070	2200	5630	2920	2065	4665	3515	9555
$y_{\min}/a_0$	0.321	0.236	0.273	0.248	0.367	0.276	0.291	0.411
$y_{\max}/a_0$	0.198	0.232	0.213	0.170	0.203	0.262	0.196	0.215
dy/a_0	0.261	0.0	0.097	0.251	0.217	0.015	0.151	0.014
χ^2	103	22.1	33.3	10.3	70.5	17.5	37.7	10.6
				"Anisotropic" model				
e	0.336	0.141	0.123	0.267	0.000	0.214	0.287	0.059
a/a_0	0.261	0.305	0.310	0.275	0.348	0.287	0.271	0.328
α_e, °	157.9	92.9	92.4	110.8	138.4	175.0	131.3	83.3
T_b, K	101425	158865	175055	170155	75340	147730	85010	90320
a_v/a_0	0.046	0.077	0.073	0.058	0.013	0.063	0.046	0.076
b_v/a_0	0.558	0.343	0.381	0.432	0.518	0.401	0.575	0.448
c_v/a_0	0.007	0.006	0.006	0.006	0.006	0.006	0.010	0.019
$T_{1*(\max)}$	15765	18785	14600	8515	19885	11600	11935	32725
$T_{2*(\max)}$	9475	11530	94845	8380	2030	8370	8630	11782
$\langle T_1 \rangle$	3010	3730	3395	2985	1410	2480	3035	18065
$\langle T_2 \rangle$	2345	5275	3935	3135	1055	2445	2630	7985
$y_{\min}/a_0$	0.24	0.25	0.25	0.26	0.13	0.21	0.29	0.38
$y_{\max}/a_0$	0.20	0.20	0.19	0.17	0.12	0.18	0.18	0.21
dy/a_0	0.226	0.129	0.178	0.297	0.358	0.238	0.188	0.032
χ^2	222	33.9	34.6	45.3	153	29.8	40.7	10.8

Note. Solutions were found for the cases of isotropic and anisotropic propagation of the radiation from the inner parts of the accretion disk with temperature T_b. The following parameters were fixed: $q = 7.70$, $i = 54°$, $T_2 = 4500$ K, $R_1 = 0.0006a_0$, $R_2 = 0.230a_0$, $R_d/\xi = 0.50$, $\beta_d = 1{}^{\circ}\!.8$, and $\alpha_g = 0.72$. $\chi^2_{0.01,n}$ is the critical χ^2 value for the $\alpha = 0.01$ significance level, and n is the number of normal points in the mean light curves of GU Mus.

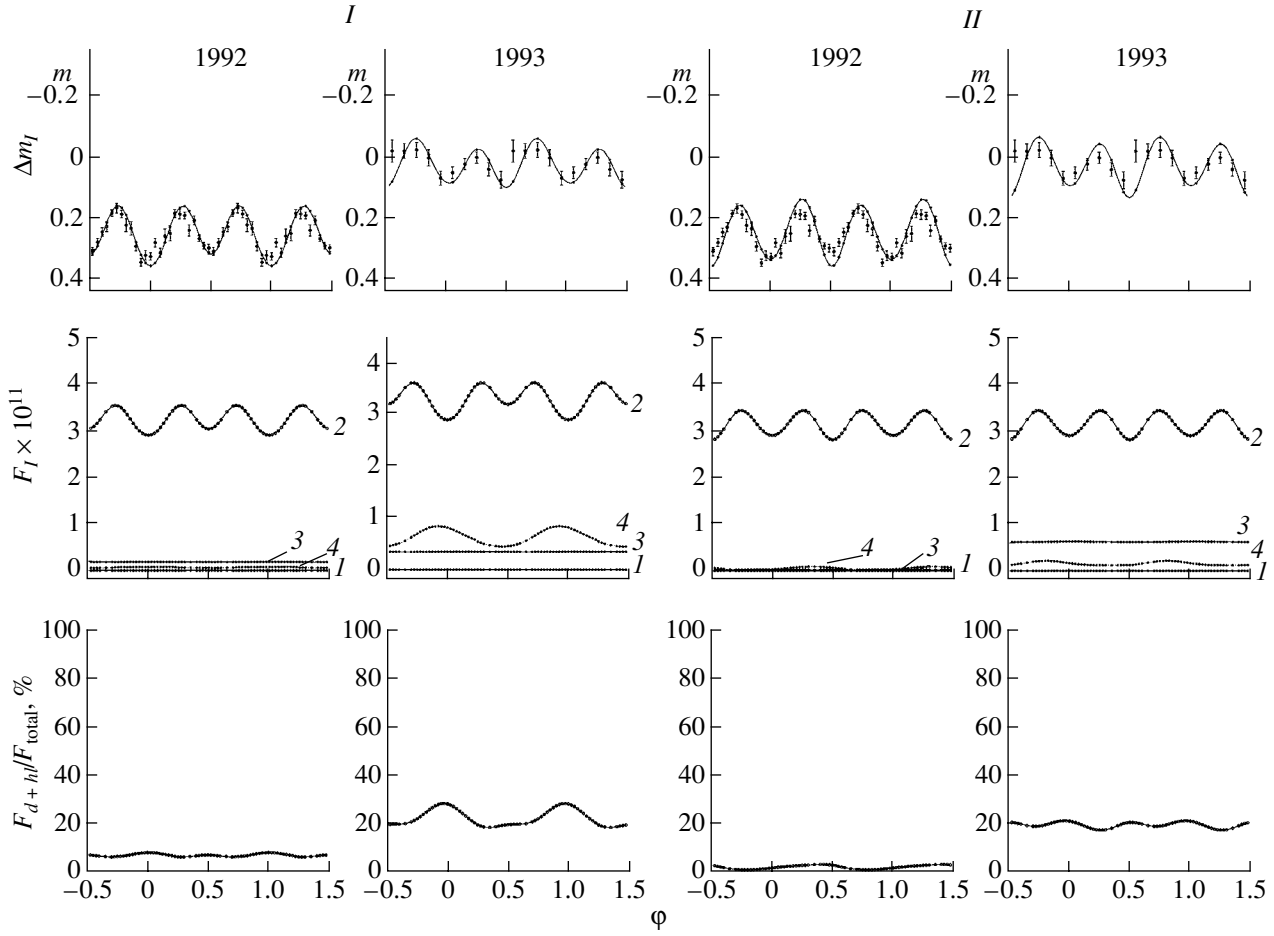

Fig. 3. Computational results for the models with isotropic (I) and anisotropic (II) radiation from the inner parts of the accretion disk derived from near-infrared (I) observations of GU Mus. The upper panels show the 1992–1993 observations (points with corresponding error bars) and theoretical curves (solid) computed using the parameters given in the table. The notation is the same as in Fig. 1.

in the computations, the contribution of its light to the combined flux depends only weakly on the trial set of remaining parameters (slight variations were found only at phase $\varphi = 0.5$, during the secondary minimum, due to re-radiation of the ultraviolet flux from inner parts of the disk by the body of the star in the case of isotropic propagation of the initial radiation). As a result, variations of the flux of the system are mainly determined by variations in the contributions of the nonstellar components of the close binary. We determined the best-fit parameters for the 1993 light curve based on the set of X_i values that gave the smallest residuals, for which the mean contribution of the light from the disk and hot line averaged over an orbit was 52–54%, in agreement with the spectrophotometric estimate [23] for that epoch. We accordingly used this value of the theoretical flux, $F_2^{th}(0.25)$, to calculate the theoretical 1992–1995 light curves in magnitudes when translating the theoretical fluxes, $F_N^{th}(X, \varphi)$, into magnitudes, $\Delta m_N^{th}(X, \varphi)$.

The table contains the parameters of the disk and hot line for 1992–1995, computed for the cases of isotropic and anisotropic propagation of the high-temperature ultraviolet radiation and X-rays from the inner parts of the disk. In the upper part of the table, we indicate the numbers of normal points for each of the light curves and their corresponding critical χ^2 values for the $\alpha = 0.01$ significance level. We can see that the agreement between the theoretical and observed light curves is somewhat better for the isotropic model. The solid curves in the upper panels of Fig. 1 are the theoretical curves for the 1992–1995 observations computed using the parameters from the table.

The hot-line model obtained assuming isotropic propagation of the radiation from the inner parts of the disk provides a very good fit to the observations of

the X-ray nova GU Mus, for both the standard 1993–1995 light curves with the normal luminosity ratio at the quadratures and the 1992 BV light curve with its anomalous distribution of the radiation fluxes at the quadratures. This can be achieved by increasing the contribution of the visible light from the hot line at phases ~ 0.25, due to the increase in the length of the shock along the line and the more favorable orientation of the disk and line for that epoch (see below).

There is a significant contribution to the secondary's brightness in the isotropic model due to the reflection effect, i.e., from reprocessing of the high-temperature radiation (X-rays and ultraviolet light) from inner parts of the disk in the atmosphere of the red dwarf. Such heating is strongest in the hemisphere facing the compact source (with the exception of equatorial regions of the star, due to screening by the disk itself). As a result, the minimum at phase $\varphi \sim 0.5$ is shallower than when the heating is not taken into account, and the minimum at phase $\varphi \sim 0.0$ is deeper [compare Figs. 1 and 2, where we show the contributions of the optical star to the combined flux (*2*) for the cases of a considerable reflection effect (Fig. 1) and virtually no reflection effect (Fig. 2)].

The middle panels of Fig. 1 show the contributions of the light from the system's components to the combined flux. In the isotropic model, the contribution of the disk varied little from epoch to epoch. The influence of the hot-line flux and its variations in the course of the system's orbital motion is much stronger. In particular, the anomalous shape of the light curve in 1992 is due to a significant increase of the flux from the windward side of the line (seen at phases $\varphi \sim 0.25$) compared to the flux from the leeward side ($\varphi \sim 0.75$). The hot-line flux depends on the size of the emitting region and the temperature at the shock front. We can estimate the size of the emitting region on the surface of the hot line from $y_{\max}$ and $y_{\min}$ (see the table), which are the y coordinates of the areas along the axis of the hot line on the windward side with the highest and lowest temperatures (recall that the highest temperature on the windward side of the line, $T_{\max}^{(1)}$, is reached where the hot line intersects the disk, whereas the leeward-side region with the highest temperature, $T_{\max}^{(2)}$, is displaced along the y axis by $dy = y_{\max}^{(1)} - y_{\max}^{(2)}$, where the superscripts 1 and 2 refer to the windward and leeward sides of the hot line). We can see from the table that the size of the hot region on the windward side of the line was quite large in 1992 ($\Delta y \sim 0.123 a_0$). The size of the emitting region on the leeward side (at phases $\varphi \sim 0.75$) is almost twice that on the windward side, and the ratio of the hot-line fluxes at phases $\varphi \sim 0.25$ and ~ 0.75 depends strongly on how much higher the mean temperature of the line material is on the windward side than on the leeward side.

Another important factor is the possible occultation of the brightest region of the shock by the edge of the disk. For the 1992 light curve, the mean temperature of the hot line on the windward side turned out to be almost 15% higher than on the leeward side. The combination of the large size of the hot-line emitting region and the temperature ratio was significant in making the radiation flux from the windward side higher than that from the leeward side. Figure 3 (column I) schematically displays the components of GU Mus in the optical. The shading shows emitting regions on the surface of the hot line for different years.

The length of the optically thick hot line in 1995 was approximately the same as in 1992, but the linear size of the emitting region was half as large ($\Delta y \sim 0.078 a_0$); the mean hot-line temperatures coincided within the errors. As a result, the luminosity from the leeward side of the hot line was higher than that from the windward side, and the variations of the radiation flux from this component were similar to those expected for hot-spot models. We see a similar picture for the 1993–1994 light curves. The hot line was quite short and resembled a modest bulge on the disk, and the linear size of the emitting region was even smaller ($\Delta y \sim 0.004 a_0$ and $\sim 0.060 a_0$ for 1993 and 1994, respectively). The main flux comes from the leeward side of the line. The increase in the hot-line luminosity in 1993 was due to a considerable increase in its highest temperature, to $\sim 30\,000$ K on the leeward side, though the mean brightness temperature for the entire surface of the hot line was not high due to the small size of the emitting region with the highest temperature. In 1994, the highest hot-line temperature decreased almost threefold. However, due to the increased linear size of the emitting region, the maximum flux from the line was reduced by only 20%.

The bottom panels of Fig. 1 present the relative contributions of the nonstellar radiation sources to the combined flux. The contribution of the secondary's light remained practically constant during 1992–1995. Thus, in this period, the main origin of variations of the system's flux were changes in the luminosities of the disk and hot line. The contribution of the nonstellar components to the combined luminosity of the system estimated using the 1992 light curve is $\sim 42\%$, in good agreement with the spectrophotometric estimate of [23], 39–45%.

With the anisotropic model for the propagation of radiation from the inner parts of the disk, the agreement between the observed and theoretical curves

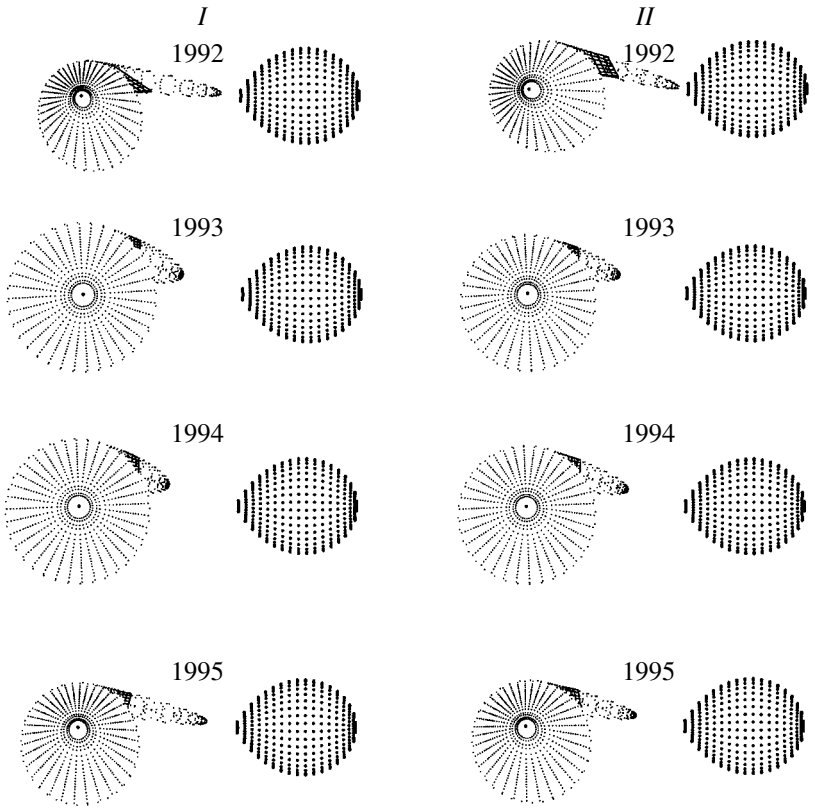

Fig. 4. Schematic of the components of GU Mus during the 1992–1995 observations for the models with isotropic (*I*) and anisotropic (*II*) radiation from the inner parts of the disk. The shading shows the emitting regions on the surface of the hot line in different years.

becomes worse for all four light curves (cf. the bottom part of the table). For example, in 1992, the anisotropic model predicted higher fluxes in the primary minimum and, correspondingly, a poorer agreement with the observations.

Comparison of the *BV* light curves of GU Mus obtained in 1993–1995 shows that it is very difficult to describe the rather shallow minimum of the observed light curves at phase $\varphi = 0.5$ in the anisotropic model. The theoretical flux is lower at phase $\varphi \sim 0.5$ than at phase $\varphi \sim 0.0$. Due to the angular distribution of the hot radiation from inner parts of the disk in the anisotropic model, the reflection effect is negligible, and variations of secondary's flux are determined solely by effect of its ellipticity, which are known to give rise to two minima with equal amplitudes, at photometric phases 0.25 and 0.75, and a deeper minimum at phase $\varphi \sim 0.5$ due to the star's gravitational darkening near the inner Lagrangian point L_1, which is most visible at such phases.

The solid curves in the upper panels of Fig. 2 are the theoretical curves for the 1992–1995 observations for the anisotropic model with the parameters from the table. The luminosity of the hot line in the anisotropic model for 1992–1995 (cf. the model parameters in the table) experienced variations similar to those for the isotropic model. In this case, the luminosity of the disk needed to reproduce the observed flux from the system is much higher than in the isotropic model. Schematic images of the components of GU Mus in the optical obtained for the anisotropic model for 1992–1995 are shown on the right-hand side of Fig. 4 (column *II*).

Thus, the isotropic-radiation model is better able to fit the shape of the *BV* light curves for the low-mass X-ray binary GU Mus. Our analysis of the optical *BV* light curves indicates that, in the GU Mus system during quiescence, there exists a source of ultraviolet light in the central parts of the accretion disk whose luminosity is higher than the X-ray luminosity, L_X, giving rise to a significant reflection effect from the optical star. The origin of this ultraviolet light remains unclear, as does the origin of the X-rays in the low state of the system.

I light curves of 1992–1993. The shapes of both the 1992–1993 *I* light curves of GU Mus are close to the standard one, with the system's brightness lower at the first than at the second quadrature (Fig. 3). The curves are symmetric, but the deeper minimum is at

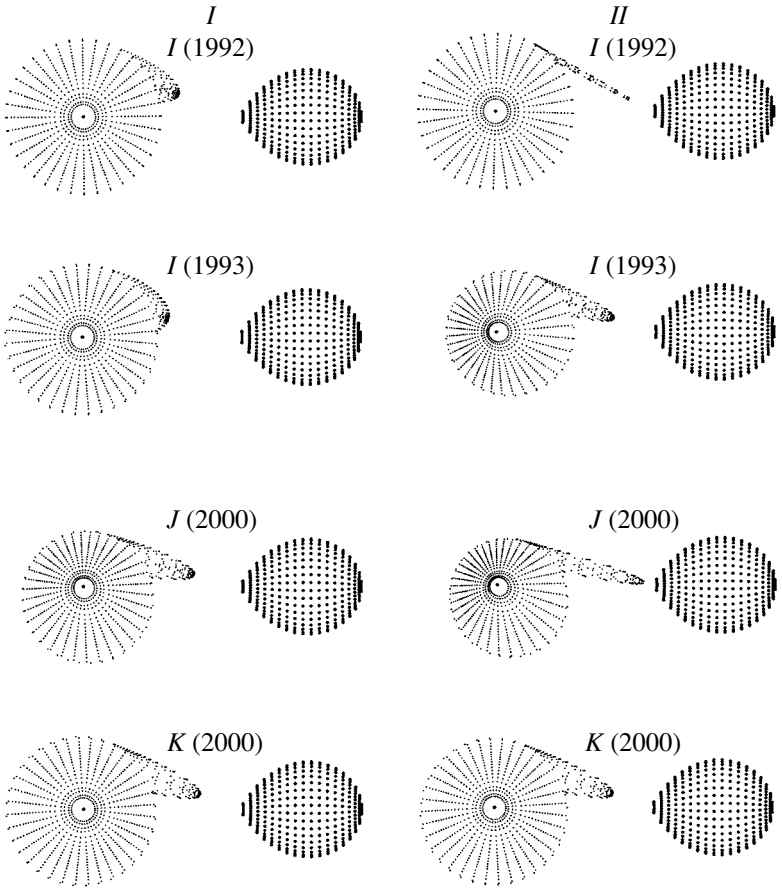

Fig. 5. Schematic of the components of GU Mus for the observations of 1992–1993 (I band) and 2000 (J and K bands) for the models with isotropic (I) and anisotropic (II) radiation from the inner parts of the disk.

phase $\varphi \sim 0.0$ rather than phase 0.5, so that non-ellipsoidal variations also contribute to the I light curve. The higher brightness at phase 0.5 testifies to the presence of an additional source of light, usually believed to be due to heating of the red dwarf by radiation from its companion. The higher brightness of the system at phase 0.75 is sometimes attributed to the emission of a hot spot at the outer edge of the disk.

The I light curves of GU Mus were analyzed using a model with purely ellipsoidal variability in [21, 23]. Both the BV and I observations were reduced to standard magnitudes by Orosz *et al.* [23], taking into account interstellar reddening using the value $E(B-V) = 0^m.29$ derived by Cheng *et al.*. Both studies [21, 23] assumed that the contribution of nonstellar sources of additional light to the system's light curve was small and did not vary with the system's orbital motion. We used our hot-line model to interpret the I light curves of Orosz *et al.* [23]. The resulting parameters for the GU Mus system in 1992 and 1993 are in good agreement with the values found for the system's optical radiation during the same time intervals (see the table).

Only Casares *et al.* [24] have estimated the contribution of light from nonstellar sources in the infrared. Their observations indicate that the contribution of the secondary to the R flux from the system is 85–88%. No similar estimates are available for spectral bands further in the infrared. The bottom panels of Fig. 3 show the relative contributions of the light from the disk and hot line to the combined flux derived by fitting the 1992 and 1993 I light curves using the isotropic (I) and anisotropic (II) models. This contribution was 5–7% in 1992 but increased to 20–25% in 1993. Due to the low contribution of the light of the disk and hot line to the combined flux in 1992 and its insignificant variability in the course of the orbital motion, the 1992 I light curve corresponded best to the model with purely ellipsoidal variability. The assumption of isotropic heating of the stellar surface by radiation from inner parts of the disk whose material is heated to the effective temperature T_b leads to consistent effective temperatures for BV and I light curves ($T_b = 115\,000 \pm 200$ K).

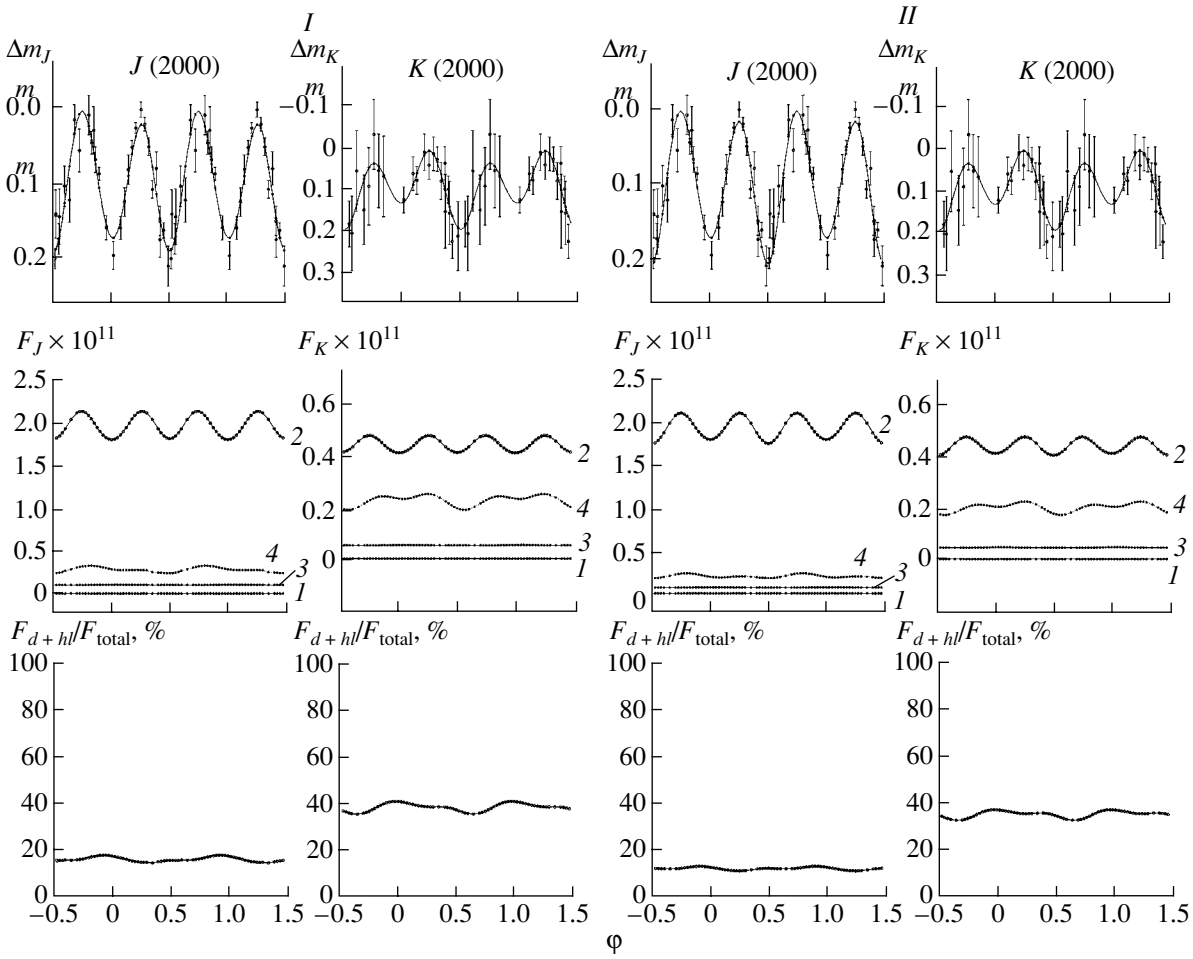

Fig. 6. Computational results for the models with isotropic (I) and anisotropic (II) radiation from the inner parts of the accretion disk obtained for the observations in the far infrared (J and K). The upper panels show the observations of GU Mus for 2000 (points with corresponding error bars) and the theoretical curves (solid) synthesized using the parameters given in the table. The notation is the same as in Fig. 1.

The table contains the parameters of the system derived from the 1992 and 1993 I light curves of GU Mus in both models, and the upper panels of Fig. 4 display the theoretical light curves computed using these parameters. The lowest residual for the 1992 light curve ($\chi^2 = 70.5$) is above the critical χ^2 value for the 1% significance level ($\chi^2_{0.01,25} = 44.3$), even in the isotropic model, despite the good reproduction of the light-curve shape. The reason is that the normal points of the 1992 I light curve demonstrate appreciable scatter, whereas the observing errors, σ_i, are comparatively low, probably testifying to physical variability of the system. The 1993 curve is well described by the isotropic model ($\chi^2 = 17.5$, while the critical χ^2 residual for the 1% significance level is $\chi^2_{0.01,10} = 23.2$).

The middle panels of Fig. 4 show the contributions of the system's components to the combined flux. Compared to 1992, the 1993 infrared fluxes for both the disk and hot line increased, by factors of about two and of more than ten, respectively, giving rise to an increase of the system's overall brightness, a stronger reflection effect, and the appearance of signatures of an orbital hump in the light curve (the observed flux from the system is higher at phase $\varphi \sim 0.75$ than at phase 0.25). At that time, the hot line was transformed into a small bulge on the outer surface of the disk (Fig. 5).

The discrepancy between the T_b values derived from the optical and infrared light curves using the anisotropic model exceeds the errors: $T_b \sim 100\,000$ and $T_b \sim 75\,000$ K, respectively. The agreement between the I observations and the theoretical light curves is a factor of two better for the isotropic than for the anisotropic model, which is not able to reproduce the depth of the secondary minimum of the I light curve without taking into account the reflection effect. Thus, even the 1993 light curve, which is fit

well by the isotropic model, is fit much worse by the anisotropic model ($\chi^2 = 29.8$, whereas the critical χ^2 value for the 1% significance level is $\chi^2_{0.01,10} = 23.2$).

J and K light curves for 2000. We interpreted the J, K light curves of GU Mus acquired by Gelino *et al.* [26] using the same technique we applied to the homogeneous BV and I light curves of [23]: the observed J, K light curves were reduced to the corresponding fluxes at the first quadrature ($m_J = 18.04$, $m_K = 16.97$).

The upper panels of Fig. 6 display the theoretical J, K light curves for the parameters providing the lowest residual, estimated fixing the parameters of both the stars and applying the above restrictions on the fluxes from the nonstellar components (see the table). When the temperature of the inner parts of the disk is ~90 000 K, the reflection effect is negligible at these wavelengths, and the isotropic (I) and anisotropic (II) models give similar results. The residuals for both models are below the critical significance level, and neither model can be rejected on the basis of this criterion. The middle panels of Fig. 6 show the contributions of the light from the system's components in the J and K filters for both models, while the lower panels illustrate the relative contributions of the light from the nonstellar components to the combined flux. In the J filter, this contribution is ~13–17% for the isotropic and ~11–14% for the anisotropic model, close to the estimates presented by Casares *et al.* [24] derived from spectrophotometric R observations, ~12–15%. For the chosen parameters, the contribution of the light from the disk and shock in the K filter increases to ~35%, on average: the flux from the hot line is comparable in both filters, while the K flux from the red dwarf is a factor of four to five lower than in the J filter. Since the fraction of light from the hot line increases in the K filter due to the contribution of free–free radiation in the infrared, to obtain the hot-line flux required to fit the shape of the K light curve, its brightness temperature must be a factor of ~1.5–2 higher than its value in the J band. This conclusion is in agreement with the estimates of the contribution to the infrared flux from free–free transitions in the disk and hot-line material obtained for other cataclysmic variables [15].

Our self-consistent analysis of photometric $BVIJK$ light curves of the X-ray nova GU Mus using the hot-line model has yielded parameters for the system occupying a narrower range than those obtained in other studies based on standard models for close binary systems (for example, cf. [26]). Using the component-mass ratio $q = M_1/M_2 \sim 8$ and the known mass function, $f_2 = 3.01 \pm 0.15\ M_\odot$, our estimate of the orbital inclination, $i = 54° \pm 1.^\circ 3$, gives the component masses $M_X = (6.7–7.6) M_\odot$ (or $7.2^{+0.4}_{-0.5}\ M_\odot$), $M_2 = 0.93(3)\ M_\odot$. These uncertainties correspond to the 90% confidence interval. Our estimate of the uncertainty in i was obtained by running through values for this parameter keeping the remaining parameters fixed at their best-fit values.

The mass we have derived for the primary, black-hole, component is in good agreement with the values found earlier in [24, 26], whereas the mass of the secondary, a K3–4V star, is higher than the values (0.70–0.74) $M_\odot$ corresponding to main-sequence stars of this spectral type [36]. The radii of single K3–4V stars do not exceed $(0.76–0.81) R_\odot$. The radius of the secondary of the binary GU Mus coincides with the size of the star's Roche lobe, which is equal to $R_2 = 0.23 a_0$ in our case, where $a_0 = (4.80 \pm 0.14) R_\odot$ is the distance between the centers of mass of the components, i.e., $R_2 = (1.10 \pm 0.03) R_\odot$, and the secondary has obviously already left the main sequence. The secondary, whose effective temperature is 4500 K, has a bolometric luminosity of $L_{\rm bol} = (1.7 \pm 0.1) \times 10^{33}$ erg/s, or $(0.43 \pm 0.01) L_\odot$. Using the observed X-ray flux at 2–30 keV during the low state, $L_X \leq 1.5 \times 10^{32}$ erg/s [1, 23], we can estimate the component-luminosity ratio to be $L_X/L_{\rm bol} < 0.1$. This ratio is too low to give rise to an appreciable reflection effect on the secondary. The observed reflection effect is apparently due to heating by ultra-soft X-ray and ultraviolet radiation from inner parts of the disk, which are heated to 100 000–180 000 K. The nature of this radiation remains unclear, but its presence necessarily follows from our analysis of the light curves.

A considerably stronger radiation flux originates from matter in the inner parts of the disk heated to temperatures of 115 000–130 000 K (see the table). Assuming this is black-body radiation, the maximum of the spectral energy distribution for such temperatures is at soft X-ray energies (~0.05 keV). Our model assumes that this radiation originates near the radius R_1, with the value adopted in our computations being $R_1 = 0.0006 a_0$, or, using the above estimates of a_0, $R_1 \sim (2–3) \times 10^8$ cm ($R_1 \sim (90–150) R_g$ in units of the gravitational radius, R_g, for masses of $M_X \sim (6.7–7.6)\ M_\odot$). The corresponding bolometric flux is $L_b \sim (0.7–2.7) \times 10^{33}$ erg/s, and the ratio of the soft X-ray to the optical flux from the secondary will be high enough to lead to an appreciable reflection effect on the red dwarf, $L_b/L_{\rm opt} \sim 0.4–1.5$.

5. CONCLUSIONS

Due to the low optical luminosity of the stars, the contribution of the optical luminosity of the accretion disk becomes significant for X-ray novae in quiescence. It is important that, due to the existence of a

region of interaction between the disk and flow (the hot line), the contribution of this gaseous structure depends on the phase of the orbital period. This gives rise to optical and infrared variability that, combined with variations due to ellipticity effects, makes interpretation of the orbital light curve less straightforward than in the case of purely ellipsoidal variability.

We have developed a technique for computing the contribution of nonstellar components to the orbital optical and infrared variability of an X-ray nova in quiescence, based on a hot-line model. Applying this technique to the X-ray nova GU Mus = GRS 1124–68, we have demonstrated that the hot-line model can provide a good description of various features of the system's orbital optical and infrared variability, including the anomalous increase of the system's luminosity at phase $\varphi \sim 0.25$. At the same time, in some cases, the hot-spot model cannot explain the anomalous shape and amplitude of the orbital light curves of "quiescent" X-ray novae.

Our detailed analysis of the orbital optical and infrared light curves of the X-ray nova GU Mus = GRS 1124–68 using a model with an ellipsoidal optical star and an accretion disk with a hot line has enabled us to determine the parameters of the disk and hot line that give rise to the light-curve anomalies, and to obtain a trustworthy estimate of the orbital inclination, making it possible to derive a more reliable estimate of the mass of the black hole in the system. On the other hand, the variations of the characteristics of the accretion disk and hot line we have discovered lead to the need for studies of unstable phenomena occurring during mass transfer in "quiescent" X-ray novae, probably due to activity of their optical components, which have convective envelopes. It is also of interest to clarify the nature of the ultraviolet radiation emerging from central regions of the disk, whose luminosity exceeds the X-ray luminosity, L_X, and leads to a considerable reflection effect on the optical star in the GU Mus system in quiescence.

Note also that we have used a Planck approximation to describe the radiation from the disk and hot line, leading to large optical depths for both the accretion disk and the region of interaction of the flow with the circumstellar envelope of the binary, the hot line. If the optical depth of the disk and hot line for the quiescent state of GU Mus is not high, the optical variability of the nonstellar components (disk + hot line) should be less strong than we have found. In this case, the accretion disk and hot line will only provide a constant addition to the system's optical luminosity. This ambiguity can be removed using spectrophotometric estimates of the component-luminosity ratio at various phases of the orbital period. Thus, further detailed and high-accuracy spectroscopic observations of X-ray novae in their low state are very promising.

ACKNOWLEDGMENTS

This study was supported by the Russian Foundation for Basic Research (projects 02-02-16088, 02-02-16462, 02-02-17642, 03-02-16622), the State Science and Technology Program "Astronomy," the State Program "Universities of Russia—Basic Research" (grant UR.02.03.012/1), grants of the President of the Russian Federation (NS-388.2003.2, NS-162.2003.2), the Programs of the Presidium of Russian Academy of Sciences "Mathematical Modeling" and "Unstable Processes in Astronomy," and the INTAS foundation (grant 00-491).

REFERENCES

1. A. M. Cherepashchuk, N. A. Katysheva, T. S. Khruzina, and S. Yu. Shugarov, *Highly Evolved Close Binary Stars. Catalogue* (Gordon and Breach, Brussels, 1996).
2. A. M. Cherepashchuk, Space Sci. Rev. **93**, 473 (2000).
3. Y. Tanaka and N. Shibazaki, Annu. Rev. Astron. Astrophys. **34**, 607 (1996).
4. Y. Tanaka, in *Black Holes in Binaries and Galactic Nuclei*, Ed. by L. Kaper, E. P. J. van den Heuvel, and P. A. Woudt (Springer, 2001), p. 141.
5. W. Chen, C. R. Shrader, and M. Livio, Astrophys. J. **491**, 312 (1997).
6. Y. Tanaka, in *Disk Instabilities in Close Binary Systems. 25 Years of the Disk-Instability Model*, Ed. by S. Mineshige and J. C. Wheeler (Univ. Acad. Press, Kyoto, Japan, 1999), p. 21.
7. *Basic Physics of Accretion Disk,* Ed. by S. Kato, S. Inagaki, S. Mineshige, and J. Fukue (Gordon and Breach, Kyoto, Japan, 1996).
8. A. M. Cherepashchuk, Usp. Fiz. Nauk **166**, 809 (1996) [Phys. Usp. **39**, 769 (1996)].
9. P. Charles, in *Black Holes in Binaries and Galactic Nuclei,* Ed. by L. Kaper, E. P. J. van den Heuvel, and P. A. Woudt (Springer, 2001), p. 27.
10. D. V. Bisikalo, A. A. Boyarchuk, O. A. Kuznetsov, and V. M. Chechetkin, Astron. Zh. **74**, 880 (1997) [Astron. Rep. **41**, 786 (1997)].
11. D. V. Bisikalo, A. A. Boyarchuk, O. A. Kuznetsov, and V. M. Chechetkin, Astron. Zh. **74**, 889 (1997) [Astron. Rep. **41**, 794 (1997)].
12. D. V. Bisikalo, A. A. Boyarchuk, V. M. Chechetkin, *et al.*, Mon. Not. R. Astron. Soc. **300**, 39 (1998).
13. D. V. Bisikalo, A. A. Boyarchuk, O. A. Kuznetsov, *et al.*, Astron. Zh. **75**, 706 (1998) [Astron. Rep. **42**, 621 (1998)].
14. D. V. Bisikalo, A. A. Boyarchuk, O. A. Kuznetsov, *et al.*, Astron. Zh. **75**, 40 (1998) [Astron. Rep. **42**, 33 (1998)].

15. T. S. Khruzina, A. M. Cherepashchuk, D. V. Bisikalo, *et al.*, Astron. Zh. **78**, 625 (2001) [Astron. Rep. **45**, 538 (2001)].
16. T. S. Khruzina, A. M. Cherepashchuk, D. V. Bisikalo, *et al.*, Astron. Zh. **80** (2003, in press).
17. N. Lund, S. Brandt, F. Makino, *et al.,* IAU Circ. **5161**, 1 (1991).
18. F. Makino *et al.*, IAU Circ. **5161**, 1 (1991).
19. M. Della Valle, B. J. Jarvis, and R. M. West, Astron. Astrophys. **247**, L33 (1991).
20. R. A. Remillard, J. E. McClintock, and C. D. Bailyn, Astrophys. J. Lett. **399**, L145 (1992).
21. E. A. Antokhina and A. M. Cherepashchuk, Pis'ma Astron. Zh. **19**, 500 (1993) [Astron. Lett. **19** (3), 194 (1993)].
22. N. I. Balog, A. V. Goncharskiĭ, Z. Yu. Metlitskaya, and A. M. Cherepashchuk, Perem. Zvezdy **21** (155), 695 (1982).
23. J. A. Orosz, C. D. Bailyn, J. E. McClintock, and R. A. Remillard, Astrophys. J. **468**, 380 (1996).
24. J. Casares, E. L. Martin, P. A. Charles, *et al.*, New Astron. **1** (4), 299 (1997).
25. T. Shahbaz, T. Naylor, and P. A. Charles, Mon. Not. R. Astron. Soc. **285**, 607 (1997).
26. D. M. Gelino, T. E. Harrison, and B. J. McNamara, Astron. J. **122**, 971 (2001).
27. R. E. Wilson and E. J. Devinney, Astrophys. J. **166**, 605 (1971).
28. N. I. Shakura and R. A. Sunyaev, Astron. Astrophys. **24**, 337 (1973).
29. T. S. Khruzina, Astron. Zh. **78**, 298 (2001) [Astron. Rep. **45**, 255 (2001)].
30. N. G. Bochkarev, R. A. Sunyaev, T. S. Khruzina, *et al.*, Astron. Zh. **65**, 778 (1988) [Sov. Astron. **32**, 405 (1988)].
31. N. I. Shakura and R. A. Sunyaev, Mon. Not. R. Astron. Soc. **175**, 613 (1975).
32. A. A. Esin, J. E. McClintock, and R. Narayan, Astrophys. J. **489**, 865 (1997).
33. A. A. Esin, E. Kuulkers, J. E. McClintock, and R. Narayan, Astrophys. J. **532**, 1069 (2000).
34. T. S. Khruzina, Astron. Zh. **77**, 510 (2000) [Astron. Rep. **44**, 446 (2000)].
35. D. Himmelblau, *Applied Nonlinear Programming* (McGraw-Hill, New York, 1971; Mir, Moscow, 1975).
36. C. Allen, *Astrophysical Quantities* (Athlone, London, 1973; Mir, Moscow, 1977).

Translated by N. Samus'

Astronomy Reports, Vol. 47, No. 8, 2003, pp. 637–647. Translated from Astronomicheskiĭ Zhurnal, Vol. 80, No. 8, 2003, pp. 692–703.

Gamma-Ray Bursts—Tracers of the History of Star Formation in the Universe

A. V. Tutukov

Institute of Astronomy, Russian Academy of Sciences, Pyatnitskaya ul. 48, Moscow, 109017 Russia

Received March 5, 2003; in final form, March 14, 2003

Abstract—The rate of gamma-ray bursts (GRBs) in the Galaxy is estimated assuming that these events result from the formation of rapidly rotating Kerr black holes during the core collapse of massive, helium, Wolf–Rayet secondary components in very close binary systems. This process brings about rapid rotation of the cores of such Wolf–Rayet stars, inevitably resulting in the formation of Kerr black holes during type Ib,c supernovae. The current rate of formation of Kerr black holes (GRBs) in the Galaxy is about 3×10^{-5}/year. Collimation of the gamma-ray radiation into a small solid angle (about 0.1–0.01 sr) brings this rate into consistency with the observed rate of GRBs, estimated to be 10^{-6}–10^{-7}/year. Possible immediate progenitors of GRBs are massive X-ray binaries with X-ray luminosities of 10^{38}–10^{40} erg/s. Due to the short lifetimes of the progenitors and the very high brightnesses of GRBs, the GRB rate can provide information about the history of star formation in the Universe on the Hubble time scale. A model in which the star-formation rate is determined by the conditions for ionization of the interstellar gas, whose density and volume are determined by supernovae, yields a Galactic star-formation history that can be viewed as representing the history of star formation in the Universe. The theoretical history of star formation is in satisfactory agreement with the history reconstructed from observations. The theoretical model for the history of star formation in the Galaxy can also be used to assess the influence of dust on optical observations of supernovae and GRBs in galaxies of various ages. © *2003 MAIK "Nauka/Interperiodica"*.

1. INTRODUCTION

Since the very first publications on gamma-ray bursts (GRBs), the mechanism producing these short (0.01–1000 s) bursts of gamma-ray radiation has been one of the most popular and complex problems in astrophysics. Although papers dedicated to GRBs are now being published at a rate that exceeds that of the detection of the events themselves ($\sim$300/yr), it has only recently became clear that most or all GRBs are associated with events in distant galaxies with high star-formation rates and accompany supernova explosions of massive stars [1–5]. However, the estimated detection rate of GRBs (10^{-6}–10^{-7}/yr [6, 7]) is much lower than the rates of known types of supernovae (10^{-3}–10^{-2}/yr [8]) for a galaxy with a mass equal to that of the Milky Way. This appreciable discrepancy must be explained in an adequate GRB model. Thus far, no such unambiguous model has been developed.

The record brightnesses of GRBs and the understanding that GRBs are associated with the evolution of short-lived massive stars and, consequently, with the local star-formation rate makes these events an invaluable tool for analyzing the history of star formation during the earliest stages of galaxy evolution, which are not accessible using other methods. As is well known, at redshifts $z > 6.3$ (ages $t < 5 \times 10^8$ yr), neutral hydrogen and the associated optical absorption make the earliest stages of star formation in the Universe inaccessible to optical methods. The extreme energy ($\sim 10^{51}$ erg), collimation (0.1 sr [7]) and penetrating power of gamma rays enable GRBs to be detected to distances $z \sim 100$ ($t \sim 10^7$ yr) [8]. Generally speaking, this enables the reconstruction of the history of star formation in the Universe, even without knowledge of the specific mechanism producing the GRBs, based only the hypothesis that the GRB rate is related to the intensity of star formation and the evolution of the most massive stars (figure). This approach, in particular, has made it possible to establish that active star formation begins at $z \sim 15$ ($t \sim 2 \times 10^8$ yr) and peaks at $z \sim 8$ and that the star-formation rate has decreased by almost a factor of 100 by the present [10]. About half of all GRBs have $z < 5$ ($t > 10^9$ yr; figure); i.e., they are located at redshifts where possible optical manifestations of the GRB could be detectable. The lack of optical "companions" for about half of even the most powerful GRBs [10] is likely due not only to the "reionization" barrier, but also to optical absorption by dust, which is usually abundant in regions of active star formation. We return to this issue below.

1063-7729/03/4708-0637$24.00

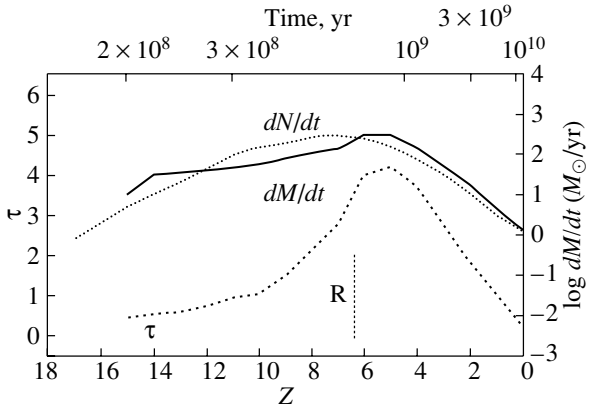

Star-formation rate dM/dt (solid line) [67], gamma-ray burst rate dN/dt (dotted line) [10], and optical depth τ (dashed line) as functions of the age of the Galaxy. $\tau = 10^{-8} X_Z M_g / M_\odot (10^4 \text{ pc}/R)^2$, where X_Z is the heavy-element abundance, M_g the mass of the gaseous component, and R the radius of the galaxy in pc. $T = 1.3 \times 10^{10}/(1+z)^{3/2}$ yr. Also shown is the reionization boundary R. Half of all the stars in the model are born before the galaxy reaches an age of $\sim 10^9$ yr.

The unique properties noted above have made studies of GRBs one of the most popular areas of research in modern astrophysics. The rate of publications in this field in the astronomical literature exceeds the detection rate of GRBs (1–3 per day) [3, 11]. The wide range of GRB durations (10^{-2}–10^3 s) and the variety of their light curves may indicate that several mechanisms are involved in their formation and/or that the observed manifestations strongly depend on the conditions under which the process responsible for the GRB occurs. The first evidence pointing to a cosmological origin for longer GRBs included their uniform sky distribution and the classical brightness distribution of bright GRBs, which appeared to be uniformly distributed in Euclidean space [12]. It is interesting that the number–flux relation flattens and forms a plateau at low gamma-ray fluxes [13], indicating that these events have reached their spatial cosmological "horizon." Because these relations flatten at fluxes $\sim 10^{-4}$ erg/cm^{-2} [13] and the distance to the "horizon" is $\sim 5 \times 10^9$ pc, the characteristic energy emitted in an isotropic burst should be equal to $\sim 10^{53}$ erg. However, the radiation of a GRB is collimated in a narrow beam filling a solid angle of only 0.1–0.01 sr [9, 14, 15], so that the characteristic energy of a GRB is actually on the order of $10^{50} - 10^{51}$ erg [16, 17], comparable to the energy of a supernova. It is important that this energy is carried away by gamma rays with characteristic energies of about 10^{-5}–10^{-6} erg, although multifaceted studies of GRBs have shown that bright bursts are accompanied by appreciable infrared, optical, and X-ray radiation [1].

Host galaxies have been identified for many GRBs (a total of thirty events so far). The distances to these host galaxies vary from $z = 0.01$ (GRB 980425) to $z = 4.5$ (GRB 000131), with the mean redshift being $z \sim 1$ [1]. In the most nearby galaxies, we find that the positions of GRBs are definitely associated with regions of active star formation and, in particular, with the spiral arms in spiral galaxies [18]. These results suggest that most, if not all, GRBs are associated with the evolution of the most massive stars [7]. Estimates of the characteristic star-formation rates in these host galaxies are about several solar masses per year [1], close to the estimated current star-formation rate in our Galaxy. However, we should bear in mind that this result may be largely due to two obvious selection effects. First, the mass function of galaxies has a break near 10^{11} $M_\odot$ [19], which implies, among other things, that most of the stellar mass in galaxies is contained in galaxies with masses close to that of the Milky Way, where the current star-formation rate is several solar masses per year [20, 21]. Second, during the early stages of the evolution of isolated massive galaxies, when the star-formation rate is high [20–22], the optical depth due to dust is also high (see the figure). This complicates the detection of optical afterglows of GRBs in young, distant, dust-rich galaxies. Therefore, such distant, young, bright ($L \sim 10^{12}$ $L_\odot$) GRB host galaxies with star-formation rates of the order of 100 $M_\odot$/yr were detected only very recently, in 2002 [4, 23, 24]. As a result, it becomes clear that, owing to their exceptional brightness, GRBs are an effective tool for studying the history of star formation in the Universe, including distant "dusty" stages and stages that are "screened" by the ionization barrier, which have remained inaccessible to other methods of observation. It is important that neither a specific model nor the conditions for the formation of a GRB have been confidently established. The only guiding circumstance is the observed association between GRBs and some type Ib,c supernovae, which, according to our current understanding, mark the end of the evolution of short-lived, massive stars that are probably in close binaries.

The aim of the current paper is to analyze a plausible model for a GRB, which suggests that a GRB occurs during the formation of a rapidly rotating Kerr black hole during the core collapse of a rapidly rotating Wolf–Rayet star [25]. The fast rotation of these stars is made possible by the presence of a close, massive black hole, which forms a close binary together with the Wolf–Rayet star. Unfortunately, the mechanism producing the GRB and the collimation of the resulting gamma-ray radiation remain unknown. The collimation may be due to the strong

magnetic field of the collapsing core [26]. Studies of related objects—accreting black holes, microquasars (e.g., GRS 1915+105), and quasars—have shown that these objects possess narrowly collimated jets of matter and, possibly, radiation. The rapid rotation of these black holes is powered by the prolonged accretion of matter from a Keplerian disk, which has a large angular momentum. This provides hope that GRBs can be explained in terms of a model based on the formation of a Kerr black hole during the collapse of the rapidly rotating 6core of a massive helium star.

2. CONDITIONS FOR AND RATE OF FORMATION OF KERR BLACK HOLES

The search for adequate GRB models has pushed forward our understanding of explosive processes with appropriate energies occurring during the evolution of single stars and close binaries. The wide range of GRB time scales (0.01–1000 s) and the fact that GRBs may be subdivided into short (with durations of less than one second) and long bursts [27] leave open the possibility that several scenarios explaining the origin of the bursts operate simultaneously. One GRB model associates these events with the disruption of low-mass ($< 0.1\ M_\odot$), unstable neutron stars during the coalescence of the components of a close binary made up of a pair of neutron stars or a neutron star and a black hole under the action of gravitational-wave radiation [28, 29]. Estimates of the rates of such events in the Galaxy vary from $\sim 10^{-4}$ [8, 30] to 3×10^{-6}/yr [31]; the former estimate neglects the "kick" a young neutron star may receive at the time of its formation. However, the high fraction of binary radio pulsars [32], the bimodal distribution of their spatial velocities, and scenario-based analyses [33] allow the absence of a substantial kick. The latter estimate of the neutron-star coalescence rate is based on the "observed" fraction of binary radio pulsars, for which the uncertainty, due to selection effects, remains rather high [32].

Naturally, to explain the low [6, 7] observed rate of GRBs, the model must include collimation of their radiation. Available estimates suggest that the radiation of GRB 980329 and GRB 000911 may be highly collimated ($(10^2$–$10^3)$ [34, 14]). However, generally speaking, the observed manifestations of the coalescence of relativistic stars in a tenuous interstellar medium are incompletely understood.

Evidence has been accumulating suggesting that at least long GRBs may be associated with type Ib,c supernovae in starburst galaxies [5, 35–38]. It is noteworthy that at least two GRBs—GRB 01121 [39] and GRB 0211189 [40]—have shown signs that they are surrounded by an intense (10^{-6}–$10^{-4}\ M_\odot$/yr) and fast ($v_w \sim 1000$ km/s) stellar wind with a characteristic radial distribution, presumably associated with the burst precursors. The high wind velocity has enabled the identification of these precursors with Wolf–Rayet stars, whose explosions at the end of their nuclear evolution have been suggested as possible models of type Ib,c supernovae. These explosions are accompanied by the formation of massive black holes with masses 5–40 $M_\odot$ [37, 41, 42]. One possible explanation of GRBs involves the formation of a rapidly rotating Kerr black hole as a result of a SN Ib,c explosion [43, 44]. The energy released in the form of neutrinos and gravitational waves during the formation of a massive black hole exceeds the gamma-ray emission of a GRB by three to four orders of magnitude.

The condition for the formation of a Kerr black hole has the obvious form [37]

$$\omega^2 R_{BH}^3 = GM_{BH}, \tag{1}$$

where ω, R_{BH}, and M_{BH} are the angular rotational velocity, radius, and mass of the black hole, respectively. It is important that the rotation of the cores of single stars or of the components of wide binaries slows during their evolution so efficiently that the young final products of stellar evolution—black holes, neutron stars, and degenerate dwarfs—rotate with velocities that are far from their limiting values [45, 46]. One obvious way to achieve the maximum rotational velocity for young neutron stars and black holes is for a compact helium presupernova to have a very close, massive, compact companion, with the axial rotation of the presupernova being synchronous with the orbital rotation of the close binary. The feasibility of this picture follows from the scenario for the evolution of close massive binaries described in [47]. The angular velocity of the orbital motion is determined by the equation

$$\omega^2 a^3 = G(M_{SN} + M_2), \tag{2}$$

where a is the semimajor axis of the binary and M_{SN} and M_2 are the masses of the helium supernova and its companion, respectively. Assuming that the collapsing core of the supernova conserves angular momentum, the condition for the formation of a Kerr black hole acquires the form

$$\left(\frac{R_n}{a}\right)^3 \frac{R_n}{R_{BH}} > \frac{M_{BH}}{M_{SN} + M_2}, \tag{3}$$

where R_n is the radius of the helium presupernova core that collapses into a black hole. Supposing as an example that $M_2 = M_{BH} = 10\ M_\odot$ and $M_{SN} = 2M_{BH}$ [37], we find that this last condition is equivalent to

$$a < 0.0145 {R_n}^{4/3}. \tag{4}$$

To estimate R_n, we assume that the black hole forms from the products of carbon burning, with a nuclear energy of $\sim 3 \times 10^{17}$ erg/g. Comparing this energy with the binding energy of the collapsing core, we find the final constraint on the semimajor axis of the binary before the explosion $a < 1.5\ R_\odot (M_{BH}/10\ M_\odot)^{4/3}$, and the orbital period is equal to $p_{orb} < (M_{BH}/10\ M_\odot)^{3/2}$ h. It is clear that such close systems can consist only of compact helium stars with radii $\sim 0.2 (M_{He}/M_\odot)^{0.6}\ R_\odot$ [47] and black holes. This estimate of the allowed interval of semimajor axes should be considered only preliminary, and special numerical computations of the late stages of the evolution of massive ($M > 10\ M_\odot$) helium stars and supernovae accompanying the formation of black holes are required to refine this interval and clarify its dependence on the mass of the helium presupernova. Note also that the mass of the black hole and the nature of the explosion may depend appreciably on the rotational velocity of the supernova core [48].

We can now use the empirical star-formation function for close binaries in our Galaxy [8, 49],

$$d^3\nu = 0.2 d\log(a/R_\odot)(M/M_\odot)^{-2.5} d(M/M_\odot) dq, \quad (5)$$

to estimate the formation rate of Kerr black holes in the framework of the mechanism proposed here. This last formula describes the distribution of close binaries forming each year in the Galaxy over their semimajor axes a, the mass M of their primaries, and their initial mass ratio q. In this connection, we should bear in mind that, to form a close binary consisting of a Wolf–Rayet star and a black hole, after depleting all its hydrogen, the secondary must expand and form the common envelope of the binary. This means that the mass of the secondary should not exceed $\sim 50\ M_\odot$ [50]. At the same time, to become a black hole, a main-sequence star should have a mass greater than $\sim 25\ M_\odot$ [37]. If we now adopt $d\log a = 0.3$ and $dq = 0.5$, the final estimate of the formation rate of Kerr black holes becomes $\sim 10^{-4}$/yr. This formation rate must be corrected for the high collimation factor of the GRB radiation (100–1000) [14,15]. Combined with this collimation factor, the inferred formation rate of Kerr black holes yields the estimate of the observed rate of GRBs in our Galaxy 10^{-6}–10^{-7}/yr [6, 7, 51]. However, we acknowledge that both estimates—observed and theoretical—remain uncertain and will be refined in the course of subsequent work.

Thus, GRBs may result from the core collapse of a Wolf–Rayet component in a close binary system accompanied by a type Ib,c supernova. The enormous (a factor of ~ 6000 [51]) difference between the rates of these events (type Ib,c supernovae and GRBs) is probably due to the necessary "fine" tuning of the initial parameters of the close binaries and the narrow (only several degrees [9, 14, 15]) opening angles of the the GRB beams. We do not address here the physics of the development of a GRB during the collapse of the rapidly rotating core of a Wolf–Rayet star. One possible mechanism for the formation of a narrowly collimated jet in the presence of a strong magnetic field in a collapsing core has been suggested by Bisnovatyi-Kogan [26].

3. ANALYSIS OF THE OBSERVED PROPERTIES OF X-RAY BINARIES. PROGENITORS OF GAMMA-RAY BURSTS

We show below that luminous, massive X-ray binaries (XRBs) are likely immediate progenitors of GRBs. Let us now look at their main observational properties in some detail. Grimm *et al.* [52] have established the principal properties of the empirical luminosity function of X-ray sources in several of the nearest galaxies. The maximum luminosity of XRBs is limited to 10^{40} erg/s. In the interval $4 \times 10^{35} < L_X(\text{erg/s}) < 10^{40}$, the luminosity function is given by the equation

$$dN/dL_X \sim L_X^{-1.6}. \quad (6)$$

The total X-ray luminosity of a starburst galaxy with a star-formation rate exceeding $\sim 5\ M_\odot$/yr is proportional to the star-formation rate μ, as we would expect, given the nature of massive XRBs. At lower star-formation rates, we have

$$L_X \sim \mu^{1.7}. \quad (7)$$

Gilfanov [54] showed that the extension of the proportionality between L_X and μ toward low star-formation rates found by Ranalli [53] is due to the inclusion of long-lived, low-mass binaries, which reflect the mass of the corresponding galaxies rather than their star-formation rates. Note also the poor statistics of the dependence of L_X on μ in this interval of L_X [53]—it is based only on two galaxies.

Special attention should be paid to the fact that the observed XRB luminosity function exhibits no discernible features near sources with luminosities corresponding to the Eddington limit for neutron stars ($L_X \sim 10^{38}$ erg/s), implying that accreting neutron stars do not contribute appreciably to the luminosity function. The hypothesis that the accretors in most bright XRBs are stellar-mass black holes is further supported by the fact that the luminosities of the brightest XRBs are bounded from above by 10^{40} erg/s. The hypothesis that this XRB luminosity limit is associated with the Eddington limit yields

a direct constraint on the maximum mass of stellar black holes: $\sim 40(1+X)\ M_\odot$, where X is the hydrogen abundance of the accreting matter. In the case of the accretion of wind material from a Wolf–Rayet star by a companion (X = 0), the upper limit on the mass of stellar black holes should be $\sim 40\ M_\odot$.

It also follows from the constraint on the XRB luminosity that the accretion rates in these systems are limited to $\sim 10^{-6}\ M_\odot$/yr. Such accretion rates rule out conservative exchange on the thermal or nuclear time scales for donors with masses exceeding $\sim 2\ M_\odot$ or $\sim 10\ M_\odot$, respectively, provided that the corresponding donors are main-sequence stars filling their Roche lobes. It follows that the donors in most of the brightest XRBs are Wolf–Rayet or OB stars feeding the black hole via their stellar wind. Note that the overall increase in the masses of the most massive black holes during the X-ray stage is fairly small, even for the brightest X-ray sources: 3×10^6 yr $\times$ $10^{-6}\ M_\odot$/yr $\sim 3\ M_\odot$ and $\sim 0.3\ M_\odot$ for hydrogen and helium donors, respectively.

Known Galactic XRBs have black holes with masses that do not exceed $\sim 20\ M_\odot$ [37], obviously due to their small number (~ 20) and their mass function, which has the form $dN/dM_{BH} \sim M_{BH}^{-2}$. The condition for survival of an XRB with a low-mass donor during a supernova in a system with a circular orbit [47] requires that the mass of the resulting black hole exceed half the mass of the Wolf–Rayet supernova, or $M_{BH}/M_\odot > 0.05(M_{MS}/M_\odot)^{1.4}$, where M_{MS} is the initial main-sequence mass of the star. It follows that, to produce a black hole with a mass of $\sim 40\ M_\odot$, the initial mass of the OB star must be 70–100 $M_\odot$. This mass is typical of the most massive OB stars in the Milky Way and other galaxies [55].

Why are most X-ray sources associated with accreting black holes, whereas, according to the initial stellar mass function (5), neutron stars should outnumber black holes by a factor of three? This estimate is based on the assumption that, in order for a star to evolve into a neutron star or black hole, its initial mass must be no less than 10 $M_\odot$ or 25 $M_\odot$, respectively [25]. The predominance of black holes among XRBs is due to the stellar-wind accretion mechanism. The rate of accretion of the stellar wind is [56]

$$\mu_{acc} = 0.25 G^2 M_a^2 v_w^{-4} a^{-2} \mu_w, \qquad (8)$$

where $v_w = (GM_d/R_d)^{0.5}$, G is the gravitational constant, M_a is the mass of the accretor, v_w is the velocity of the stellar wind, a is the semimajor axis of the XRB orbit, and μ_w is the intensity of the wind. R_d and M_d are the radius and mass of the donor. It follows from (8) that the accretion rate of a black hole of mass 10 $M_\odot$ is almost a factor of 50 higher than that of a neutron star of mass 1.4 $M_\odot$. At the same time, the number of neutron stars is only a factor of three higher than the number of black holes. This explains the predominance of black holes among the accretors of bright XRBs, despite the somewhat longer duration of the X-ray stage for accreting neutron stars, owing to the two–threefold difference in the characteristic masses of the donors in these systems.

Let us now turn to the relationship between the integrated X-ray fluxes of galaxies and their star-formation rates. For massive galaxies with masses exceeding that of the Milky Way, the X-ray luminosity is proportional to the star-formation rate, which is quite natural in the case of a standard luminosity function. However, at lower galaxy masses and star-formation rates, the observed X-ray luminosity decreases much faster than the corresponding star-formation rates [see (7)]. This provides direct evidence that a new factor associated with the galaxy mass plays a role in these galaxies. If XRBs are assumed to have the same standard luminosity function, this additional factor may depend on the abundance of metals X_Z in the galactic material. For galaxies more massive than the Milky Way, $X_Z = X_{Z_\odot}$, whereas $M \sim X_Z^\alpha$ for less massive galaxies, where $\alpha = 0.7$–1.3 [57, 58]. The stellar-wind intensities of OB stars can be written $\mu \sim X_Z^\beta$, where $\beta = 0.5$–1.7 [55, 59]. We now assume that $\mu \sim M$ to obtain $L_X \sim \mu^{1+\beta/\alpha}$. The luminosity function (7) shows that, to explain its observed slope, we must suppose that $\beta/\alpha = 0.7$. This appears quite possible given the appreciable uncertainty in the parameters used. It is important that, to explain the observed dependence (7) in terms of the proposed model, the dependence of the stellar-wind intensity on the heavy-element abundance must be independent of nature of the donor, i.e., of whether it is an OB or Wolf–Rayet star. These two types of stars should display different mechanisms for sustaining their stellar wind [37]. Note also that the hypothesis that the XRB luminosity function has a universal form is not consistent with the dependence of the specific X-ray luminosity on the star-formation rate in the galaxy [52].

Let us now consider the XRB luminosity distribution (6). We first estimate the maximum luminosity attained by an XRB fed by the stellar wind of the donor. We assume that the accretor is a black hole and that the donor is close to filling its Roche lobe, i.e., a = $2.5R$. We find from (7)

$$\mu_{acc} = 0.04(M_{BH}/M_d)^2 \mu_w. \qquad (9)$$

In general, the donor can be either a main-sequence star with

$$\mu_w = 10^{-16.4}(L_{\rm OB}/L_\odot)^2 \qquad (10)$$
$$= 10^{-12.4}(M_{\rm OB}/M_\odot)^4\ M_\odot/\text{yr},$$

according to [55], or a Wolf–Rayet star with

$$\mu_{\rm WR} = 10^{-8.6}(L_{\rm WR}/L_\odot)^{0.7} \qquad (11)$$
$$= 10^{-6.1}(M_{\rm WR}/M_\odot)^{1.3}\ M_\odot/{\rm yr},$$

according to [37]. Estimates made using the formalism adopted earlier in [60] show that we can neglect the X-ray driven stellar wind in this case. We can now find from the latter three relations that, to provide the maximum observed luminosity, XRB $\sim 10^{40}$ erg/s ($\mu_{acc} \sim 10^{-6}\ M_\odot$/yr) for $M_{BH} = 40\ M_\odot$, the mass of the Wolf–Rayet star must be $M_{\rm WR} < 100\ M_\odot$. These are usual masses for Wolf–Rayet stars [37]. To provide the maximum luminosity of an XRB with an OB donor, the mass of the donor must exceed $\sim 200\ M_\odot$, ruling out these stars as possible donors for the brightest XRBs.

Finally, we can use the XRB luminosity function (6) to make another comparison of the "feasibility" of these two types of donors. For a Salpeter mass distribution for the primaries and a flat mass distribution for the secondaries in close binaries (5), the mass distribution of the binaries has the form $d\nu/dM_2 \sim M_2^{-1.5}$. Because $M_{\rm WR} \sim M^{1.4}$ [47], we have $d\nu/dM_{\rm WR} \sim M_{\rm WR}^{-1.36}$. The lifetimes of Wolf–Rayet stars are [47] $T_{\rm WR} \sim M_{\rm WR}^{-0.5}$, so that we finally obtain for $L_X \sim \mu_{\rm WR} \sim M_{\rm WR}^{1.3}$ (11) the theoretical luminosity function $dN/dL_X \sim L_X^{-1.66}$, which virtually coincides with the observed luminosity function (6) within the uncertainties. Applying the same procedure to OB donors yields a luminosity function of the form $dN/dL_X \sim L_X^{-1.1}$, which differs appreciably from (6).

As a result, we conclude that at least the brightest X-ray sources associated with XRBs are extremely close binaries consisting of massive black hole accretors and Wolf–Rayet donors. At the same time, these very systems are potentially promising candidates for explaining GRBs. Two conclusions follow from this coincidence. First, close binaries suitable for producing Kerr black holes should be among the brightest XRBs of their host galaxies. Second, since the brightest systems should be the closest ones, it is worthwhile to search for variability in the brightest XRBs, due to eclipses of the X-ray source by the wind from the donor or by the donor itself, with periods ranging from several hours to several days. A supernova accompanied by a GRB produces a close binary consisting of massive black holes. Due to the emission of gravitational waves, the components of such systems coalesce at a rate of $\sim 10^{-6}$/yr per Milky Way [30] and are the brightest stellar sources of gravitational waves.

An important question now arises: why have no obvious systems with Wolf–Rayet donors been found among the sixteen XRBs with black-hole accretors cataloged thus far? The most likely explanation is observational selection effects. According to the luminosity function (6), the brightest X-ray sources are few in number, and those in our Galaxy are located far from the Sun and are thus hidden from an "optical" observer located in the plane of symmetry by interstellar dust. Furthermore, the large widths of the spectral lines of Wolf–Rayet stars make periodic variations of their radial velocities—and, consequently, binarity of such stars with X-ray companions—difficult to detect. The search for eclipses in XRBs may be a more promising way of their detection.

4. GAMMA-RAY BURSTS—TRACERS OF STAR FORMATION IN GIANT GALAXIES

Because GRBs are visible at cosmological distances [10], it is absolutely essential to take into account the history of star formation when analyzing the evolution of their rate. Available estimates show that the GRB rate per galaxy increases by almost a factor of ten in going from the present ($z = 0$) to galaxies with ages $\sim 1.6 \times 10^9$ yr ($z = 3$) [12, 61]. If we assume a "standard" nature for long GRBs, we can reconstruct the "observed" dependence of the GRB rate on galaxy age (see the figure) [10, 62] in the age interval 10^8–10^{10} yr. It seems natural to assume that star formation starts at an age of $\sim 10^8$ yr, since this is close to the time scale for the collapse of protostars with an initial density of the order of the mean density of our Galaxy. Recall that, according to the observed luminosity function, our Galaxy, with a mass of $\sim 2 \times 10^{11}\ M_\odot$ and a radius of ~ 20 kpc, is representative of the stellar component in the Universe [63]. This provides hope that modeling the history of star formation in our Galaxy will enable us to approximately reconstruct the history of star formation in the Universe. It is important that the penetrating power of GRBs makes them a realistic and potentially very effective tool, enabling us to see for the first time beyond the hydrogen reionization "barrier," which makes the first billion years of star formation in the Universe inaccessible to optical observations.

The physically self-consistent model for the numerical analysis of star formation in disk galaxies of [20, 21] assumes that the star-formation rate in a disk galaxy is determined by the full ionization of hydrogen in a presumably uniform interstellar medium. Qualitatively, this condition is equivalent to the empirical Schmidt law, which says that the local star-formation rate is proportional to the square of the interstellar-gas density. The volume of an axisymmetric gaseous component of a given constant radius and variable thickness is determined by the balance between the

kinetic energy pumped into the interstellar gas by supernovae and the dissipation of this energy during collisions of gaseous clouds. The model shown in the figure enables us to describe the history of star formation in the Galaxy from the formation of the first stars ($t \sim 10^8$ yr) to the present ($t \sim 1.3 \times 10^{10}$ yr). The advantages of this model include the following: (1) it implies that the current integrated star-formation rate in the Galaxy should be proportional to the mass of its gaseous component, as is confirmed by observations over a very wide range of galactic gas masses (10^2–10^{11} $M_\odot$), (2) it can describe the observed distribution of stellar heavy-element abundances, and (3) it can explain the observed dependence of the metal abundance on distance from the Galactic plane [20].

We adopted a galaxy model with a mass and radius of the order of those of the Milky Way, since the Milky Way is representative of the stellar population [64] and most ($\sim$30) of the GRBs identified thus far are associated with galaxies with luminosities similar to that of the Milky Way [65]. In this model, the star-formation rate gradually increases with the age of the galaxy. The maximum star-formation rate, $\sim 300\ M_\odot$/yr, is attained at $z = 5$ ($t = 8 \times 10^8$ yr) and is nearly two orders of magnitude higher than the present-day star-formation rate in the Galaxy. About half of all stars form by the age of $\sim 10^9$ yr. It is interesting that only about one-quarter of all stars in this model are born beyond the reionization barrier. The age of the galaxy when it attains its maximum star-formation rate in the adopted model is completely determined by its radius and, given the observed dispersion of galactic radii with similar masses [66], varies within a factor of three. For example, a twofold decrease or increase of the galactic radius [21, 67] would shift the time of star-formation maximum to ages of $\sim 2.5 \times 10^8$ and $\sim 3 \times 10^9$ yr, respectively. Comparison with mostly optical observations of galaxies show that the model of galactic evolution portrayed in the figure describes the observed history of star formation in massive galaxies at $z < 3$ [20, 67].

We can see that the model star-formation history and the "observed" evolution of the GRB rate [10, 68, 69] in the figure are qualitatively in good agreement. We should not give too much weight to the question of quantitative agreement at this point, given the remaining uncertainties in both the parametrization of the model and, most importantly, in the procedure for reconstructing the history of GRB rates from the known statistical properties of the ensemble of GRBs. It follows from the model that a large fraction of stars formed after the epoch of hydrogen reionization. Combined with possible mechanisms for the decrease of the dust optical depth in galaxies, this can explain the high fraction of GRBs (about half [1]) that are accompanied by detectable optical afterglows.

The figure shows that the optical halfdepth of the galactic model varies with time. It increases during early stages of the evolution, reflecting the increase in the metal abundance as a result of supernovae. The optical halfdepth reaches its maximum, $\sim 5^m$, at $z = 5$, and afterward begins to decrease as a result of the decrease in the gas content in the galaxy due to the conversion of gas into stars. Observational estimates of the role of intergalactic dust in the absorption of radiation are currently limited to a search for an X-ray halo produced by dust grains around the blazar GB 1508+5714 ($z = 4.3$) by Telis [70]. The absence of a detectable halo suggested that the optical extinction of radiation from cosmological objects by intergalactic dust is insignificant. At the same time, infrared observations of galaxies with ongoing star formation and the model described here show that optical extinction by dust in young galaxies requires a special discussion.

Young gas-rich galaxies are known to be powerful sources of infrared radiation resulting from the conversion of stellar radiation by interstellar dust grains [71, 72]. As noted above, a high gas content is always accompanied by a high star-formation rate and, consequently, by a high luminosity of the galaxy. The model shows that optical halfdepth of the young galaxy during the stage of active star formation and a high GRB rate (see the figure) could have been as high as several magnitudes, even in the polar direction. Naturally, inclination of the axis of a disk galaxy to the line of sight can only increase the extinction. As a result, the extinction toward several observed supernovae is as high as $\sim 8^m$ [74]. The measured extinction in young ($z = 2$–4) galaxies can reach $\sim 3^m$ [73], close to the model estimate. Evidence for strong optical extinction by dust in the host galaxies of GRBs is also provided by their high bolometric-to-ultraviolet luminosity ratios ($\sim$100) [75]. Our old Galaxy also exhibits appreciable extinction in the polar direction ($\sim 0\overset{m}{.}5$). The mean observed extinction averaged over 80 000 galaxies is $\sim 1^m$ [76]. Against this background, the low extinctions observed for 39 extragalactic type Ia supernovae ($\sim 0\overset{m}{.}2$ [77]) and 22 optically identified GRBs ($\sim 0\overset{m}{.}3$ [4, 78]) appear paradoxical. Moreover, it is well known that up to half of all GRBs have optical afterglows [79, 80]. How can the high mean optical extinction of the host galaxies by dust be reconciled with the low extinctions of optically detected SN Ia's and GRBs?

A number of factors may be responsible for the relatively low mean observed optical extinction of SN Ia's and GRBs. The most important ones probably include various selection effects. Let us consider one of these. Suppose that the optical depths τ

of galaxies are distributed according to the law $dN/d\tau = Ae^{-A\tau}$. The median optical depth for this distribution is $0.7/A$. If we assume that galaxies are distributed uniformly in space, the volume where objects of a given luminosity are observable for a fixed minimum flux depends on the optical depth as $e^{-1.5\tau}$. As a result, the median optical depth of detectable objects is $0.5(A + 1.5)^{-1}$. For $A = 1$, the median extinction is $0\overset{m}{.}2$ (as for SN Ia's) for a median optical-depth extinction of $0\overset{m}{.}7$ for the initial galaxy distribution. This example clearly illustrates the role of the predominance of objects with low extinctions in optically selected samples. Note that the decrease in the mean extinction for SN Ia's is also due to a considerable degree to the fact that a sizeable fraction of these supernovae occur in elliptical galaxies with negligible optical extinction by dust.

There is another obvious selection effect that decreases the dust optical depth in disk galaxies with ongoing star formation, primarily for GRBs. This is due to the presence of gaseous supershells with sizes of the order of the thickness of the gaseous disk of the galaxy, which are usually transparent in the polar directions [81]. Such holes in the gaseous-dust disk "expose" regions of violent star formation and young stellar objects, including GRBs, to an external observer. Another important effect decreasing the extinction toward young objects in young, dust-rich galaxies compared to that implied by the model in the figure is that an appreciable fraction of young stars are in galaxies that are less massive than the Milky Way [63, 82]. Numerical simulations show that such galaxies do not reach solar metal abundances [57, 58] and, consequently, large optical depths, probably due primarily to the loss of the products of supernovae carried away by the galactic wind [21, 67].

Another effect that may also be important in increasing the chances of detecting optical radiation from GRBs and the associated type Ib,c supernovae is the vaporization of dust by the powerful and narrowly collimated GRB radiation. Simple estimates show that the blackbody temperature of the dust is higher than the vaporization temperature at distances smaller than 30 kpc from the GRB. This demonstrates the potentially high efficiency of the gamma-ray radiation in vaporizing dust in the host galaxy, at least within the GRB radiation cone. To summarize, the above effects are capable of explaining the low mean extinction toward SN Ia's and the high fraction (up to half) of GRBs with optical afterglows [1].

5. CONCLUSIONS

The origin of GRBs remains a subject of heated debate. Despite the variety of models proposed, no real criteria making it possible to discriminate between them were known until recently, when several long GRBs were identified with type Ib,c cosmological supernovae. The detection of the manifestations of intense stellar winds in the optical spectra of these supernovae leads us to conclude that, at least in these cases, the presupernovae were massive Wolf–Rayet stars [83], which appear to be common progenitors for type Ib,c supernovae. In this paper, we have assumed that a GRB marks the formation of a Kerr black hole during the core collapse of a Wolf–Rayet component in an extremely close binary. Preliminary estimates yield the plausible estimate for the rate of such events in a galaxy like ours $\sim 10^{-6}$–10^{-7}/yr, and make it possible to describe the "observed" cosmological history of such events. However, given the wide variety of manifestations of observed GRBs, we must acknowledge that this mechanism cannot represent the entire range of these events, so that studies of other interpretations, such as the coalescence of the components of extremely close binaries [30], magnetorotational supernovae associated with the formation of neutron stars with strong magnetic fields and rotation energies of the order of $\sim 10^{51}$ erg ($p_{rot} \sim 0.01$ s) [84, 85], etc., should remain on the research agenda.

Theoretical studies of the history of star formation in massive galaxies suggest a severalfold increase in the star-formation rate in the past, in the age interval 2×10^9–13×10^9 yr [22, 86–89], as is confirmed by observations. The use of GRBs as tracers of star-formation history enables us to expand the age interval accessible for objective analyses to earlier epochs up to ages of $\sim 10^8$ yr (see the figure). A comparison of the theoretical star-formation history with the "observed" history based on GRBs would enable the establishment of their qualitative and currently satisfactory quantitative agreement. Further improvement of the theoretical model and refinement of the "observed" star-formation history reconstructed from GRBs would enable a more constructive approach to such comparisons. One problem of our model that should be pointed out is the origin of the delay of the complete ionization of the gaseous components in galaxies at $z = 6$–20. Formally, in the adopted model, star formation brings about complete ionization of the uniformly distributed galactic gas within a dynamical time scale $\sim 10^8$ yr, which is much less than the age of the Universe during the reionization stage. Several factors can be suggested to explain this delay, such as a nonuniform distribution of the gas or a delay in the onset of star formation due to a low initial gas density. This problem requires a special analysis.

We have searched for the immediate progenitors of GRBs in the framework of a model that associates these events with the collapse of the rapidly rotating cores of massive Wolf–Rayet star in the closest binary

systems. To this end, we have analyzed the principal properties of the brightest stellar extragalactic X-ray sources [52]. Most of these sources reside in the spiral arms of their host galaxies [91], supporting their identification as massive stars. The donors in these systems are massive sources of powerful stellar winds—most likely massive (20–70 $M_\odot$) Wolf–Rayet stars that fill their Roche lobes nearly completely—while the accretors are black holes with masses of 10–40 $M_\odot$. The presence of a massive black hole is dictated by the high (up to $\sim 10^{40}$ erg/s) luminosities of the brightest XRBs, while Wolf–Rayet stars are required to provide high (up to $10^{-6}\ M_\odot$/yr) accretion rates by the black hole. The reconstruction of the observed XRB luminosity function requires scenario modeling to determine the contributions of various binaries to the observed XRB luminosity function in the framework of current concepts about the nature and intensity of the stellar winds of massive stars. Allowance for the dependence of the stellar-wind intensity on the heavy-element abundance may make it possible to explain the strong observed dependence of the integrated specific luminosity of XRBs on the star-formation rate for low-mass galaxies with low ($\mu < 5\ M_\odot$/yr) star-formation rates [52].

The extreme closeness of the XRB components that is required to produce Kerr black holes during the core collapse of Wolf–Rayet stars suggests that eclipses can be used to search for binarity of the brightest X-ray sources. It is important that this method can also be applied to eclipsing XRBs in other galaxies that are beyond the reach of detailed spectroscopic analyses. The brightest XRBs—GRB progenitors—are expected to have orbital periods ranging from several hours to several days, and it is possible that an appropriate rereduction of already available X-ray monitoring data would make it possible to find close binaries among these objects.

The qualitative agreement between the model star-formation history and the evolution of the GRB rate as a function of galaxy age enables us to normalize the GRB rate to the star-formation rate. The current star-formation rate in our Galaxy is $dM/dt \sim 2\ M_\odot$/yr [21]. The local observed GRB rate is $\nu \sim 10^{-6}$–10^{-7}/yr in a galaxy with a mass of the order of the mass of the Milky Way. As a result, we can write

$$\nu \sim 10^{-7} dM/dt, \qquad (12)$$

where dM/dt is in units of $M_\odot$/yr. The total number of galaxies with masses of the order of the mass of the Milky Way located within the cosmological "horizon" is $\sim 10^9$ [64], explaining why the observed rate of GRBs is about one burst per day. Given the high degree of collimation of the GRB radiation, the real formation rate of Kerr black holes should exceed the GRB rate by two to three orders of magnitude [9, 14, 15] and be equal to 10^{-4}–10^{-5}/yr. This means that GRBs accompany the formation of 10% of black holes in the Galaxy. In these estimates, we have assumed that stellar black holes are the final products of the evolution of stars with initial masses exceeding $\sim 25\ M_\odot$ [37].

The GRB mechanism discussed here, in which a GRB is the result of the collapse of a rapidly rotating core of a massive star, is, in many respects, similar to the magnetorotational supernova hypothesis [84], which has been suggested to explain the ejection of a supernova shell by the energy associated with the rapid rotation of a young pulsar with a strong magnetic field. However, after the slowing of their rotation at the red supergiant stage, the cores of single stars and of the components of wide binaries are unlikely to be capable of producing either GRBs, rotating neutron stars, or radio pulsars. Only compact, helium, presupernova components in close binaries with compact companions, which are "forced" to rotate rapidly by their orbital motion, can offer the necessary conditions for the formation of rapidly rotating young neutron stars and Kerr black holes.

If our suggestion that GRBs accompany the formation of Kerr black holes is confirmed, this raises the question of the formation of supermassive (10^6–$10^{10}\ M_\odot$) black holes in galactic nuclei, which are manifest as quasars in the presence of sufficiently active accretion. Quasars have been detected to high redshifts, $z \sim 6$, corresponding to ages of only $\sim 7 \times 10^8$ yr [64, 91]. This suggests that quasars may have formed via the collapse of short-lived ($\sim 2.5 \times 10^6$ yr) supermassive stars, ruling out the accretion-driven increase of their masses from the maximum stellar values $\sim 100\ M_\odot$, at least for these objects [64]. The fast rotation of these supermassive stars is powered by disk accretion of gas from the galactic nucleus. The formation of a Kerr black hole appears likely in this case. It is more difficult to estimate the formation rate of supermassive black holes in galactic nuclei and the observational manifestations of these events. If the formation rate of supermassive black holes is estimated from the observed number of quasars within the horizon ($\sim 10^5$ [64]), it should be $\sim 10^{-5}$/yr, which would virtually rule out the possibility of observing such events. However, quasars quite probably represent only a fraction of the total number of supermassive black holes "switched on" by powerful accretion. If we suppose that the number of supermassive black holes that form as a result of the collapse of supermassive stars is of the order of the number of galaxies located within the

horizon—($\sim 10^{10}$–10^{11})—the formation rate of supermassive black holes becomes quite "observable." This problem requires a special analysis.

Finally, given the observed variety of GRBs, we note that Kerr black holes can also form during the coalescence of relativistic components in close binaries—neutron stars and black holes—as a result of gravitational radiation. Theoretical estimates of the rate of such events in the absence of "kicks" accompanying the formation of the neutron stars vary from 10^{-4}/yr for binary neutron stars to 10^{-6}/yr for binary black holes [30]. The collimation of the resulting radiation that probably accompanies such events provides hope for reconciling the rate of detectable events with the observed rate.

It is worth noting the inevitable association between the formation of stellar-mass Kerr black holes and a powerful burst of gravitational waves with a duration of $\sim 10^{-4} M/M_\odot$ s, which emits ~ 0.1 of the binding energy of the black hole. These events may become the first detected sources of gravitational waves produced by stellar objects.

6. ACKNOWLEDGMENTS

This work was supported by the Council for the Support of Leading Scientific Schools of Russia (project code no. 00-15-96533), the Russian Foundation for Basic Research (project code 03-02-254), and the State Science and Technology Program "Astronomy." I am grateful to G. Bisnovatyĭ-Kogan, R. Manchester, B. Paczynski, and R. Sunyaev for discussions of magnetorotational supernovae, the empirical formation rates of single and binary radio pulsars, gamma-ray burst models, and the X-ray binary luminosity function.

REFERENCES

1. S. Djorgovski, S. R. Kulkarni, D. A. Frail, *et al.*, astro-ph/0301342.
2. S. Dado, A. Dar, and A. DeRujula, Astron. Astrophys. **393**, L25 (2002).
3. K. Hurley, R. Sari, and S. Djorgovski, astro-ph/0211620.
4. J. Bloom, S. Kulkarni, and S. Djorgovski, Astron. J. **123**, 1111 (2002).
5. J. Reeves, D. Watson, J. P. Osborne, *et al.*, astro-ph/0206480.
6. S. Mao and B. Paczynski, Astrophys. J. Lett. **388**, L45 (1990).
7. B. Paczynski, Astrophys. J. Lett. **494**, L45 (1998).
8. A. Tutukov and L. Yungel'son, Astron. Zh. **79**, 738 (2002) [Astron. Rep. **46**, 667 (2002)].
9. D. Frail, S. R. Kulkarni, R. Sari, *et al.*, Astrophys. J. Lett. **562**, L55 (2001).
10. D. Lamb, astro-ph/0210433; astro-ph/0210434.
11. E. Gögüs, P. M. Woods, C. Kouveliotou, *et al.*, Astrophys. J. Lett. **526**, L93 (1999).
12. B. Stern, J. Atteia, and K. Hurley, Astrophys. J. **578**, 304 (2002).
13. M. Kudryavtsev, S. I. Svertilov, O. V. Morozov, *et al.*, Pis'ma Astron. Zh. **28**, 331 (2002) [Astron. Lett. **28**, 287 (2002)].
14. P. Price, E. Berger, S. R. Kulkarni, *et al.*, Astrophys. J. **573**, 85 (2002).
15. S. Yost, D. Frail, and F. Harrison, Astrophys. J. **577**, 155 (2002).
16. M. Schmidt, Astrophys. J. **559**, L79 (2001).
17. E. Berger and S. Kulkarni, astro-ph/0301268.
18. H. Pedersen, J.-L. Atteia, M. Boer, *et al.*, Messenger No. 100, 32 (2000).
19. S. Anderson, J.-C. Cuileandre, and R. Pello, astro-ph/0009431.
20. C. Firmani and A. Tutukov, Astron. Astrophys. **264**, 37 (1992).
21. D. Wiebe, A. Tutukov, and B. Shustov, Astron. Zh. **75**, 3 (1998) [Astron. Rep. **42**, 1 (1998)].
22. J. Gallagher, D. Hunter, and A. Tutukov, Astrophys. J. **284**, 544 (1984).
23. E. Berger, L. L. Cowie, S. R. Kulkarni, *et al.*, astro-ph/0210645.
24. D. Frail, F. Bertoldi, G. H. Moriarty-Schieven, *et al.*, Astrophys. J. **565**, 829 (2002).
25. A. Tutukov and A. M. Cherepashchuk, Astron. Zh. **80**, 419 (2003).
26. G. Bisnovatyi-Kogan, Astrophys. Space Sci. **276**, 259 (2001).
27. M. Botcher and C. Dermer, Astrophys. J. **529**, 635 (2000).
28. S. Blinnikov, I. D. Novikov, T. V. Perevodchikova, and A. G. Polnarev, Sov. Astron. Lett. **10**, 177 (1984).
29. B. Paczynski, Astrophys. J. Lett. **308**, L43 (1986).
30. A. Tutukov and L. Yungelson, Mon. Not. R. Astron. Soc. **260**, 675 (1993).
31. V. Kalogera, C. Kim, and D. R. Lorimer, astro-ph/0212048.
32. A. Faulkner, M. Kramer, G. Hobbs, *et al.*, astro-ph/0301349.
33. A. Tutukov and A. Fedorova, Astron. Zh. (2003, in press).
34. S. Yost, D. A. Frail, F. A. Harrison, *et al.*, Astrophys. J. **577**, 155 (2002).
35. K. Postnov and A. Cherepashchuk, Astron. Zh. **78**, 602 (2001) [Astron. Rep. **45**, 517 (2001)].
36. S. McGreen *et al.*, astro-ph/0206298.
37. A. Tutukov and A. Cherepashchuk, Astron. Zh. (2003, in press).
38. T. Le Floch, P.-A. Duc, I. F. Mirabel, astro-ph/0211252.
39. J. Bloom, S. R. Kulkarni, P. A. Price, *et al.*, Astrophys. J. Lett. **572**, L45 (2002).
40. B. Schaefer, C. L. Gerardy, P. Hoflich, *et al.*, astro-ph/0211189.
41. A. Tutukov and A. Cherepashchuk, Astron. Zh. **62**, 1124 (1985) [Sov. Astron. **29**, 654 (1985)].

42. A. Tutukov and N. Chugaĭ, Pis'ma Astron. Zh. **18**, 606 (1992) [Sov. Astron. Lett. **18**, 242 (1992)].
43. W. Zhang, S. E. Woosley, A. I. MacFadyen, astro-ph/0207436.
44. A. Heger and S. E. Woosley, astro-ph/0206005.
45. A. Tutukov, Nauchn. Inf. **11**, 27 (1969).
46. S. Kawaler, astro-ph/0301539.
47. A. Tutukov and L. Yungelson, Nauchn. Inf. **27**, 57 (1973).
48. C. Fryer, A. Heger, N. Langer, and S. Wellstein, astro-ph/0112539.
49. E. Popova, A. V. Tutukov, and L. R. Yungelson, Astrophys. Space Sci. **55**, 55 (1982).
50. R. Humphreys, Astrophys. J., Suppl. Ser. **29**, 389 (1975).
51. J. Scalo and J. Wheeler, Astrophys. J. **566**, 723 (2002).
52. H. Grimm, M. Gilfanov, R. Sunyaev, astro-ph/0205371.
53. P. Ranalli, A. Comastri, G. Setti, astro-ph/0211304.
54. M. Gilfanov, H.-J. Grimm, R. Sunyaev, astro-ph/0301331.
55. R. Stothers, Astrophys. J. **568**, 312 (2002).
56. A. Tutukov and L. Yungelson, Astrofizika **12**, 576 (1976).
57. J. Brodie and J. Huchra, Astrophys. J. **379**, 157 (1991).
58. K. Nagamine, M. Fukugita, R. Cen, and J. P. Ostriker, Astrophys. J. **558**, 497 (2001).
59. R. Kudritzki and J. Puls, Annu. Rev. Astron. Astrophys. **38**, 613 (2000).
60. I. Iben, Jr., A. V. Tutukov, and A. V. Fedorova, Astrophys. J. **486**, 955 (1997).
61. B. Stern, J.-L. Atteia, and K. Hurley, astro-ph/0202181.
62. T. Donaghy, D. Q. Lamb, D. E. Reichart, and C. Graziani, astro-ph/0210436.
63. N. Trentham and R. Tully, Mon. Not. R. Astron. Soc. **335**, 712 (2002).
64. A. Tutukov, Astron. Astrophys. Trans. **21**, 137 (2002).
65. S. Djorgovski, S. R. Kulkarni, D. A. Frail, *et al.*, astro-ph/0302004.
66. A. Kostyunin, Astron. Zh. **72**, 811 (1995) [Astron. Rep. **39**, 722 (1995)].
67. B. Schustov, D. Wiebe, and A. Tutukov, Astron. Astrophys. **317**, 397 (1997).
68. J. Norris, Astrophys. J. **579**, 386 (2002).
69. B. Stern, J.-L. Atteia, and K. Hurley, Astrophys. J. **578**, 304 (2002).
70. G. A. Telis *et al.*, Astrophys. J. **585**, 312 (2003).
71. I. Smail, F. N. Owen, G. E. Morrison, *et al.*, Astrophys. J. **581**, 844 (2002).
72. J. Afonso, B. Mobasher, B. Chan, and L. Cram, Astrophys. J. **559**, L101 (2001).
73. V. Vijh, A. N. Witt, and K. D. Gordon, astro-ph/0301121.
74. A. DiPaola, V. Larionov, A. Arkharov, *et al.*, Astron. Astrophys. **393**, L21 (2002).
75. E. Berger, L. L. Cowie, S. R. Kulkarni, *et al.*, astro-ph/0210645.
76. G. Kaufmann, T. M. Heckman, S. D. M. White, *et al.*, astro-ph/0204055.
77. M. Sullivan, R. S. Ellis, G. Aldering, *et al.*, astro-ph/0211444.
78. E. Le Floch, P.-A. Duc, I. F. Mirabel, *et al.*, astro-ph/0301149.
79. J. Gorasabel, L. Christensen, J. Hjorth, *et al.*, astro-ph/0212334.
80. D. Lamb, astro-ph/0210433.
81. I. V. Igumenshchev, A. V. Tutukov, B. M. Shustov, Astron. Astrophys. **234**, 396 (1990).
82. S. Sabatine, J. Davies, R. Scaramella, *et al.*, astro-ph/0301585.
83. A. Panaitesau and P. Kumar, astro-ph/0301032.
84. G. Bisnovatyĭ-Kogan, Astron. Zh. **47**, 813 (1970) [Sov. Astron. **14**, 652 (1970)].
85. A. Koenigl, astro-ph/0302110.
86. M. Sawicki, H. Lin, and H. K. C. Yee, Astron. J. **113**, 1 (1997).
87. P. Madau, H. C. Ferguson, M. E. Dickinson, *et al.*, Mon. Not. R. Astron. Soc. **283**, 1388 (1997).
88. M. Schmidt, Astrophys. J. Lett. **559**, L79 (2001).
89. G. Wilson, I. Smail, R. S. Ellis, and W. J. Couch, Mon. Not. R. Astron. Soc. **284**, 915 (1997).
90. S. Holt, E. M. Schlegel, U. Hwang, and R. Petre, astro-ph/0301319.
91. A. Kaspi, W. N. Brandt, and D. P. Schneider, astro-ph/0001299.

Translated by A. Dambis

Astronomy Reports, Vol. 47, No. 8, 2003, pp. 648–659. Translated from Astronomicheskiĭ Zhurnal, Vol. 80, No. 8, 2003, pp. 704–716.

Studies of Classical Barium Stars

L. I. Antipova[1], A. A. Boyarchuk[1], Yu. V. Pakhomov[1], and V. E. Panchuk[2]

[1] *Institute of Astronomy, Russian Academy of Sciences, ul. Pyatnitskaya 48, Moscow, 109017 Russia*

[2] *Special Astrophysical Observatory, Russian Academy of Sciences, Nizhniĭ Arkhyz, Karachaĭ-Cherkessian Republic, 357147 Russia*

Received December 6, 2002; in final form, January 10, 2003

Abstract—Using atmosphere models based on high-resolution spectra, we have derived the abundances of chemical elements in the atmospheres of seven classical barium stars and compared them with the elemental abundances of moderate barium stars and normal red giants. The behavior of elements up to the iron peak is the same in all three groups of giants, providing evidence that they have a common origin. The dependence of the anomalous abundances of *s*-process elements on stellar mass and metallicity is qualitatively similar for all three groups, probably indicating that a substantial role is played by the evolutionary phase of the stars. We conclude that the barium-star phenomenon and the overabundances of *s*-process elements in barium stars cannot be explained as a consequence of binarity alone. The extent to which the *s*-process elements are overabundant is affected by the mass, metallicity, and evolutionary phase of the given star, and any of these parameters may prove to be important in a specific object.

1. INTRODUCTION

The spectra of late-type giants often display chemical peculiarities. Such stars include carbon stars, S stars, and so-called barium stars, a peculiar group of G–K giants. Quantitative analyses of the spectra of these stars are essential for our understanding of stellar evolution, since these spectra can reflect the synthesis of elements in the interiors of stars at different evolutionary phases.

Barium stars, or BaII stars, were distinguished as a separate group by Bidelman and Keenan in 1951 [1] on the basis of their unusually strong BaII lines; in addition, they display enhanced SrII lines and CH, C_2, and CN bands. Warner [2] introduced quantitative indices (1 to 5) to classify the strength of the BaII lines, which Bidelman and Keenan [1] suggested was associated with an overabundance of barium. Garstang [3] noted that many elements heavier than barium are also overabundant in these stars. The first quantitative study of the barium star HD 46407, which is classified as K0IIIBa3, was carried out in [4] via a growth-curve analysis based on spectrograms with dispersions of 10 and 15 Å/mm at photographic and visual wavelengths, respectively. It was concluded that elements heavier than Sr display anomalously high abundances (on average, by an order of magnitude), with these elements initially being produced by the *s* process (slow neutron capture in the stellar interior) and subsequently being carried to the stellar atmosphere. Further studies of elemental abundances in the atmospheres of barium stars [5–13] made it possible to determine the abundance anomalies with higher accuracy and analyze their origin. The carbon abundances in the atmospheres of classical barium stars exceed that in the solar atmosphere by 0.3 dex, while normal red giants display a carbon deficit of approximately 0.5 dex, as is typical for the phase of hydrogen burning in the CNO cycle. Barium stars exhibit "normal" nitrogen and oxygen abundances, unlike red giants, which display nitrogen excesses, also typical for the CNO cycle. It was confirmed that the overabundances of *s*-process elements reach 1.5 dex in individual stars. The metallicity—i.e., the average abundance of iron-group elements—ranges from 0.0 to −0.5 dex in studied barium stars, which may indicate that they belong to the old disk population of the Galaxy.

Two basic hypotheses have been offered to explain the barium-star phenomenon. According to one, barium stars are single (see, for example, [14]). At certain stages of their evolution, conditions favoring the *s* process and the synthesis of rare-earth elements are created in their interiors. This may occur either (1) during explosive ignition of helium in the degenerate core (the helium flash) or (2) in the course of thermal pulsations in the helium shell source during the asymptotic giant branch (AGB) stage. In both cases, convection can carry *s*-process elements to upper layers of the atmosphere. However, these scenarios face serious difficulties. Modern hydrodynamical calculations of the core helium flash [15] indicate that,

1063-7729/03/4708-0648$24.00

Table 1. List of selected barium stars

HD	Coordinates (2000.0)		m_v	Sp	P_{orb}, day
	α	Δ			
46407	$06^h32^m46^s.9$	$-11°09'59''$	6.30	K0III Ba3	457.4
65854	08 03 32.3	+54 09 35	8.41	G8III Ba1	–
77247	09 03 32.3	+53 06 30	6.87	G8III Ba2	80.5
199394	20 55 09.0	+46 21 00	7.00	G8II Ba1	4382.6
199939	20 58 43.5	+44 24 53	7.44	K0III Ba4	584.9
204075	21 26 39.9	−22 24 41	3.77	G4II Ba3	2378.2
205011	21 31 50.2	+23 50 43	6.43	G9III Ba2	2836.8

although there is mixing of the products of helium burning and the hydrogen envelope, few neutrons are produced, due to the insufficient temperature in the corresponding zone at this evolutionary phase. On the other hand, the fact that the luminosities of barium stars are substantially lower than is needed for the ignition of burning in the helium shell source presents serious difficulties for the thermal-pulsation model.

The other hypothesis suggests that barium stars are binary (see, for example, [16]). In this picture, the more massive component, which evolves more rapidly than its companion, reaches the AGB, where helium thermal flashes in a shell source occur. In its subsequent evolution, the star loses matter enriched in heavy elements and becomes a white dwarf. Some of this matter falls onto the surface of the secondary, which becomes a barium star. Monitoring of radial velocities carried out for over a decade has yielded the orbits of 75 barium stars thus far [16–21]. As a rule, these stars have orbital periods from several hundreds to several thousands of days. The mass functions of several stars have been derived from their radial velocities. Assuming the mass of a barium star is about 1.5 $M_\odot$, which is very likely [16], these estimates imply that the secondaries in these systems are white dwarfs. This has been observationally confirmed for several barium stars [22, 25]. The binarity hypothesis is also supported by the inverse dependence between the overabundance of s-process elements and the orbital period of the binary [13]. However, this hypothesis likewise cannot be adopted unconditionally, and a number of observational results present real challenges (see, for example, [20]). Therefore, supplementary data based on observations with high spectral resolution are desirable.

In a number of studies, nucleosynthesis calculations have been used to estimate the relative abundances of heavy elements, with the aim of explaining the observed abundances of these elements in barium stars. Currently, the most attractive hypothesis is that a BaII star originates due to mass transfer from an AGB star onto its companion in a binary. Therefore, the most extensive nucleosynthesis calculations have been made for AGB stars in the phase of thermal flashes in the helium shell source.

One of the first studies of this kind [24] considered the unbranched s process, and observations of barium stars were analyzed on the basis of these calculations in [25]. Later, Malaney [26] performed nucleosynthesis calculations for s-process elements formed during thermal pulsations on the AGB, using a new network of nuclear reactions that took into account a large number of branching processes. These calculations were carried out for several stellar models with different core masses. The abundances of elements from Fe to Tl were determined for each model after

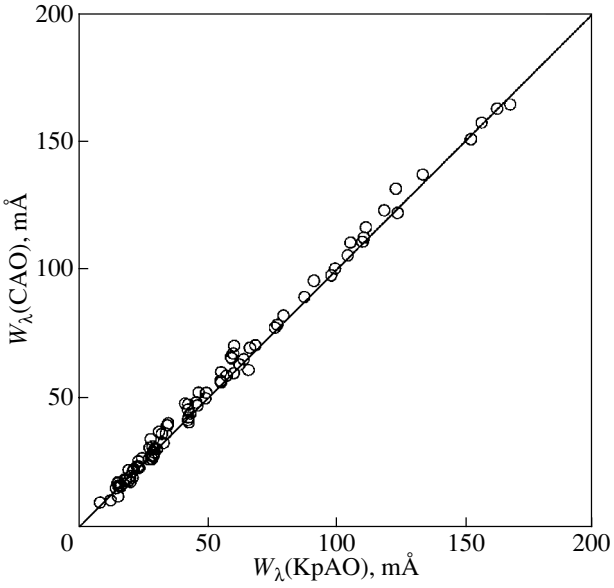

Fig. 1. Comparison between the equivalent widths of spectral lines of the red giant β Gem observed with the 2.6-m Shain telescope and the 6-m SAO telescope.

Table 2. Parameters of the atmospheres of the studied stars

HD	Sp	T_{eff}, K	$\log g$	V_t, km/s	[M]	[s-el/Fe]	$M/M_\odot$
46407	K0III Ba3	4916	2.48	1.43	−0.11	$+1.38 \pm 0.12$	2.1
65854	G8III Ba1	4958	2.74	1.30	−0.22	$+0.80 \pm 0.10$	1.6
77247	G8III Ba2	4978	2.20	1.51	+0.07	$+0.56 \pm 0.10$	3.9
199394	G8II Ba1	5080	2.81	1.53	−0.03	$+0.90 \pm 0.06$	2.3
199939	K0III Ba4	4600	1.91	1.74	−0.35	$+1.53 \pm 0.13$	2.5
204075	G4II Ba3	5300	1.75	2.16	−0.09	$+1.05 \pm 0.08$	4.8
205011	G9III Ba2	4880	2.63	1.51	−0.03	$+0.86 \pm 0.13$	2.4

30 pulsations, i.e., after 30 neutron exposures, after which these abundances reach their asymptotic values. Similar calculations were performed for a single neutron exposure (as may occur, for example, in a single helium flash in a degenerate core). It turned out that the abundances of some elements, such as Rb, Eu, and Tb, are sensitive to the neutron density at the time of the exposure, so that observations of their lines in stellar spectra may provide information about this quantity (the importance of Rb observations was also noted in [27–29]). Furthermore, a single exposure predicts low abundances of Cu, Zn, and Ge. In addition, different core masses and other parameters yield different relative abundances of s-process elements. Comparisons between the calculations and observations can provide information about the nature and localization of processes leading to the barium-star phenomenon. However, as was noted in [26], the results of observations of the same star by different authors often differ appreciably, leading to uncertainties when comparing observations and calculations. Thus, one of the most important tasks that must be undertaken if we wish to obtain a fuller understanding of the barium-star phenomenon is to obtain high-accuracy observations and use them to determine the abundances of the largest number of s-process elements possible with the maximum possible certainty.

Classical barium stars, as a peculiar group of red giants, were included in our program, which is aimed primarily at comparative analyses of various subclasses of red giants based on homogeneous, high-resolution, high signal-to-noise observational data carried out using a single method.

2. OBSERVATIONS AND DATA REDUCTION

Our previous studies of red giants, which did not consider spectral peculiarities and did not include moderate barium stars, were based on observations carried out with the 2.6-m Shain Telescope at the Crimean Astrophysical Observatory [30–34]. A CCD camera mounted in the first camera of a diffraction spectrograph mounted at the Coudé focus (with a resolution of $R = 50\,000$) was used as the detector. Due to the relative faintness of classical barium stars, they were observed with the 6-m telescope of the Special Astrophysical Observatory. The NES echelle spectrograph mounted at the Nasmyth focus [35] provided a spectral resolution of $R = 60\,000$, and a 2048×2048 CCD camera was used as the detector [36]. Table 1 presents the list of classical barium stars studied along with their orbital periods, taken from [16–21].

The accuracy of the derived chemical composition of a stellar atmosphere depends on the accuracy of the measured line equivalent widths. Since the studied spectra were obtained with an echelle spectrograph, we paid special attention to a careful determination of the continuum level, which was complicated by the presence of substantial variations of the intensity along the spectral strips of different orders (with widths of about 70 Å), as is characteristic of echelle spectra. We were guided by previously analyzed photographic spectra of red giants obtained with the 2.6-m Shain telescope, whose widths were about 1000 Å, making it possible to trace the continuum level with certainty. We excluded the edges of spectral orders, where the intensity of the echelle spectra varied too steeply and the measured line equivalent widths were more uncertain.

We checked the reliability of our analysis by comparing line equivalent widths for the red giant β Gem (frequently used as a comparison star) derived from observations made at the Crimean Astrophysical Observatory and Special Astrophysical Observatory (Fig. 1). Figure 1 shows that there is no systematic shift between these two data sets, and the scatter of individual points does not exceed the uncertainties of the equivalent-width measurements (several milliangstroms). Thus, a comparative chemical-composition analysis based on equivalent widths

Table 3. Elemental abundances in the atmospheres of the barium stars

	HD 46407		HD 65854		HD 77247		HD 199394		HD 199939		HD 204075		HD 205011	
	N	[X]	N	[X]	N	[X]	N	[X]	N	[X]	N	[X]	N	[X]
CI	1	0.02	2	−0.19 ± 0.11	−	−	1	−0.05	1	+0.39	3	0.13 ± 0.04	2	−0.07 ± 0.16
NaI	2	0.09 ± 0.07	2	−0.12 ± 0.02	−	−	3	+0.09 ± 0.05	3	−0.03 ± 0.05	2	0.33 ± 0.06	2	0.17 ± 0.02
MgI	2	0.27 ± 0.08	1	−0.04	2	0.39 ± 0.04	1	+0.20	2	+0.21 ± 0.10	1	0.74	3	0.42 ± 0.03
SiI	5	−0.14 ± 0.03	4	−0.24 ± 0.04	3	0.09 ± 0.07	11	−0.01 ± 0.07	5	−0.17 ± 0.04	4	−0.09 ± 0.03	4	−0.07 ± 0.02
CaI	4	−0.11 ± 0.03	5	−0.09 ± 0.05	2	0.13 ± 0.01	2	−0.02 ± 0.08	2	−0.41 ± 0.03	5	0.14 ± 0.12	4	−0.08 ± 0.04
ScI	1	0.03	2	−0.23 ± 0.02	−	−	7	−0.11 ± 0.05	4	−0.33 ± 0.05	1	−0.22	2	−0.12 ± 0.03
ScII	5	0.00 ± 0.03	4	−0.25 ± 0.05	3	0.35 ± 0.18	7	−0.06 ± 0.08	4	−0.24 ± 0.09	3	−0.21 ± 0.03	3	−0.04 ± 0.02
TiI	35	−0.10 ± 0.07	47	−0.19 ± 0.06	13	0.06 ± 0.07	59	+0.09 ± 0.18	39	−0.34 ± 0.12	23	−0.03 ± 0.09	35	−0.08 ± 0.07
TiII	4	0.03 ± 0.11	11	−0.20 ± 0.08	6	0.26 ± 0.12	13	+0.02 ± 0.08	6	−0.35 ± 0.06	5	0.12 ± 0.12	8	0.05 ± 0.08
VI	9	−0.16 ± 0.04	13	−0.20 ± 0.07	4	0.10 ± 0.08	15	−0.08 ± 0.14	9	−0.35 ± 0.06	5	−0.28 ± 0.11	10	−0.07 ± 0.06
VII	1	0.89	−	−	−	−	−	−	−	−	4	−0.26 ± 0.16	1	0.48
CrI	12	−0.11 ± 0.08	33	−0.21 ± 0.09	7	0.08 ± 0.05	41	+0.01 ± 0.13	13	−0.39 ± 0.12	10	0.03 ± 0.14	13	0.01 ± 0.09
CrII	4	0.04 ± 0.02	6	−0.20 ± 0.04	6	0.12 ± 0.08	10	−0.03 ± 0.05	3	−0.26 ± 0.08	6	−0.12 ± 0.04	8	0.09 ± 0.07
MnI	9	−0.18 ± 0.21	4	−0.31 ± 0.08	3	−0.01 ± 0.11	3	−0.18 ± 0.06	3	−0.35 ± 0.09	5	−0.02 ± 0.09	5	−0.27 ± 0.09
FeI	63	−0.14 ± 0.08	105	−0.20 ± 0.08	40	0.09 ± 0.05	119	−0.02 ± 0.12	82	−0.34 ± 0.11	57	−0.04 ± 0.11	60	−0.03 ± 0.05
FeII	7	−0.14 ± 0.04	11	−0.35 ± 0.07	8	0.08 ± 0.07	8	−0.11 ± 0.03	4	−0.42 ± 0.05	5	−0.08 ± 0.07	7	−0.07 ± 0.05
CoI	13	−0.08 ± 0.07	12	−0.16 ± 0.06	7	0.08 ± 0.08	15	−0.09 ± 0.09	5	−0.33 ± 0.04	5	−0.15 ± 0.07	11	0.05 ± 0.07
NiI	24	−0.20 ± 0.07	57	−0.27 ± 0.10	17	−0.03 ± 0.07	53	−0.08 ± 0.10	38	−0.37 ± 0.17	35	−0.08 ± 0.13	30	−0.11 ± 0.07
ZnI	1	−0.15	1	−0.35	2	0.23 ± 0.08	1	−0.10	1	−0.39	1	−0.03	2	0.03 ± 0.07
SrI	−	−	−	−	−	−	−	−	1	+1.03	−	−	1	1.04
YI	2	0.95 ± 0.06	1	0.43	−	−	1	+0.05	−	−	1	1.02	1	0.66
YII	4	1.07 ± 0.02	6	0.40 ± 0.07	4	0.59 ± 0.06	5	+0.85 ± 0.06	5	+1.01 ± 0.13	3	0.98 ± 0.32	7	0.85 ± 0.07
ZrI	10	0.78 ± 0.09	9	0.36 ± 0.12	3	0.61 ± 0.30	8	+0.69 ± 0.13	11	+0.47 ± 0.16	7	0.82 ± 0.13	8	0.53 ± 0.08
ZrII	4	1.40 ± 0.10	3	0.61 ± 0.07	1	0.77	2	+0.87 ± 0.05	2	+1.24 ± 0.03	1	1.47	3	0.98 ± 0.07
MoI	3	0.85 ± 0.09	4	0.33 ± 0.04	1	0.25	3	+0.79 ± 0.02	3	+0.77 ± 0.05	1	0.69	3	0.43 ± 0.05
RuI	3	1.35 ± 0.14	1	0.28	−	−	2	+0.49 ± 0.17	4	+1.25 ± 0.21	3	+1.71 ± 0.18	−	−
CdI	1	0.84	−	−	−	−	−	−	−	−	−	−	−	−
BaII	−	−	1	0.84	1	1.23	1	+1.04	1	+1.38			1	1.01
LaII	5	1.39 ± 0.04	5	0.69 ± 0.12	3	0.74 ± 0.05	4	+0.90 ± 0.15	8	+1.44 ± 0.15	3	0.76 ± 0.10	4	0.77 ± 0.10
CeII	13	1.23 ± 0.09	8	0.56 ± 0.08	4	0.57 ± 0.12	5	+0.84 ± 0.06	14	+1.25 ± 0.11	7	0.90 ± 0.10	6	0.68 ± 0.07
PrII	7	1.20 ± 0.09	3	0.55 ± 0.02	2	0.54 ± 0.09	1	+0.99 ± 0.19	16	+1.14 ± 0.21	5	0.82 ± 0.15	3	0.69 ± 0.01
NdII	24	1.19 ± 0.12	17	0.67 ± 0.12	9	0.55 ± 0.10	26	+0.97 ± 0.18	35	+1.20 ± 0.17	8	0.91 ± 0.05	19	0.76 ± 0.10
SmII	4	0.53 ± 0.08	3	0.02 ± 0.05	2	0.33 ± 0.05	1	+0.45 ± 0.15	4	+0.70 ± 0.15	3	0.26 ± 0.08	1	0.71
EuII	−	−	−	−	−	−	−	−	1	+0.85	1	0.19	−	−
DyII	−	−	1	0.85	−	−	−	−	1	+0.80	−	−	1	1.08
HfI	1	1.16	1	0.72	−	−	−	−	1	+0.80	−	−	1	0.85
[M]		−0.11 ± 0.07		−0.22 ± 0.06		+0.07 ± 0.04		−0.03 ± 0.06		−0.35 ± 0.05		−0.09 ± 0.09		−0.03 ± 0.07

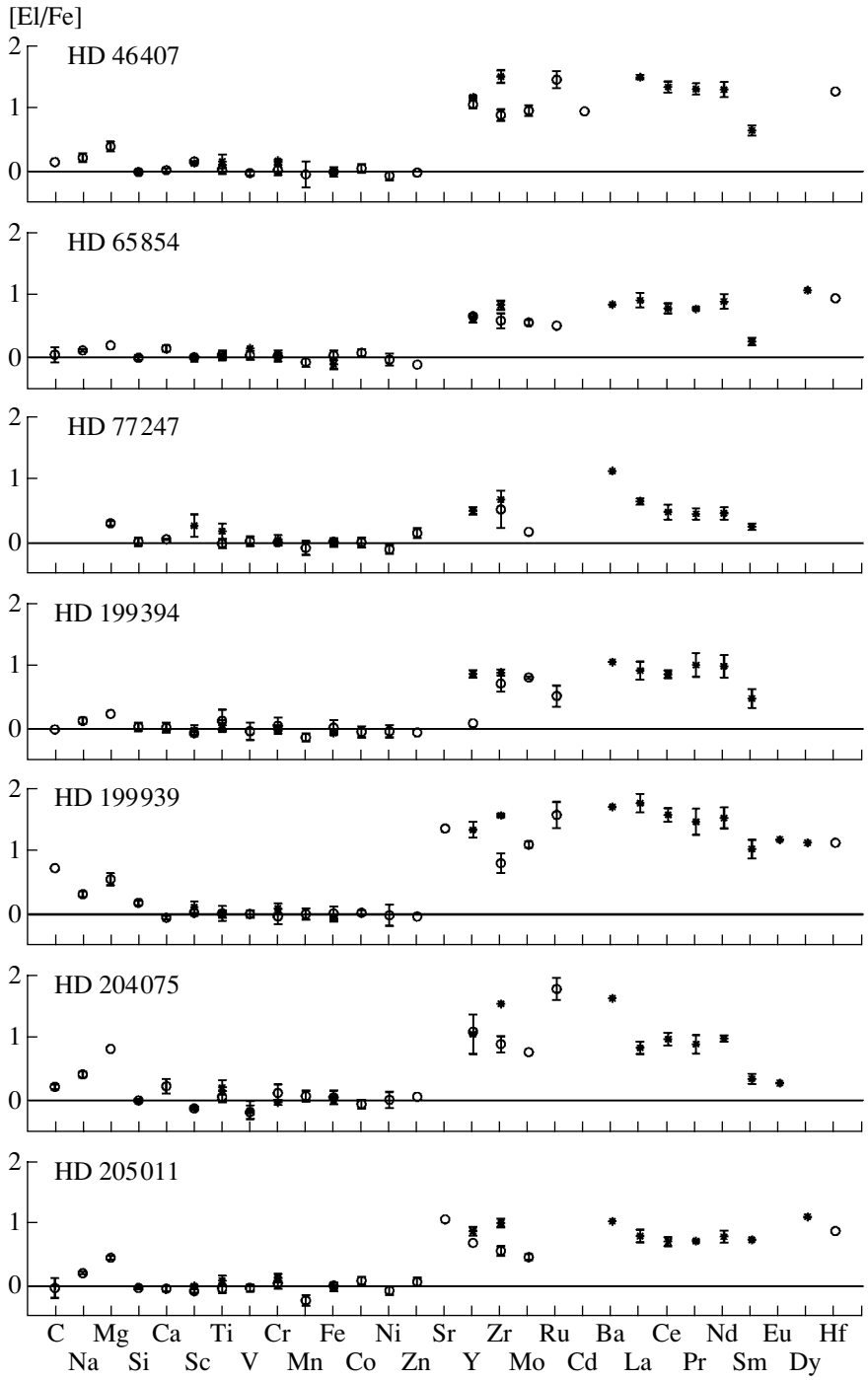

Fig. 2. Elemental abundances of the studied classical barium stars relative to those in the solar atmosphere. The circles mark abundances derived from lines of neutral atoms, while the asterisks mark those derived from ion lines. The errors in all the abundances are given and were calculated as the dispersions of the values for the individual lines. The absence of an error bar indicates that the abundance was determined from a single line.

obtained from observations made with these two telescopes should not contain systematic differences.

The selection of spectral lines for the abundance determinations was also done very carefully. We chose pure (unblended) lines for which the oscillator strengths were known with reasonable certainty. When checking the lines for blending, we relied primarily on the VALD [37] database. In general, the processing of the spectra and measurement of the equivalent widths were carried out using the procedure described in detail in [30]. For one exposure, the NES spectrograph recorded the spectral

interval from 4600 to 6030 Å. The Sun served as a comparison star. The equivalent widths of the solar lines were estimated from Shain-Telescope observations of scattered solar light [33]. We hope that the differential analysis will minimize errors in the oscillator strengths. The list of equivalent widths for the selected lines and corresponding oscillator strengths can be found at http://bnfm1.sai.msu.ru/~pakhomov/article/2/cqw.dat.

The turbulent velocity V_t was derived from the FeI lines using the condition that the iron abundances be independent of the equivalent widths of the lines that were used to derive them.

As in the previous studies [30–34], we assumed that the relative abundances of iron-group elements from Ti to Ni do not differ from their values in the solar atmosphere. This seems justified, since only the abundances of lighter elements (He–Si) and s-process elements are expected to change in the course of evolution of ordinary stars; variations in the relative abundances of iron-group elements occur only in supernova outbursts.

It was shown in [30, 33] that, under this assumption, calculations of the abundances of iron-group elements for different atmospheric parameters (T_{eff}, $\log g$) close to those expected can be used to determine the parameter values that minimize the scatter of the relative abundances of these elements. According to [30, 33], the effective temperature can be estimated with an accuracy of ±20 K and the surface gravity $\log g$ with an accuracy of ±0.1dex. The technique is described in detail in [30]. Table 2 presents the atmospheric parameters obtained for the studied stars. The parameters of the classical barium stars do not differ systematically from those of moderate barium stars and are also close to those of normal red giants. Further, we calculated the corresponding model atmospheres in accordance with Kurucz's ATLAS9 code, which were, in turn, used to calculate the elemental abundances using the WIDTH9 [38] code.

To avoid a loss of accuracy in the abundances due to uncertainty in the damping constants, which affect the line wings, we primarily restricted our analysis to lines with equivalent widths not exceeding 100 mÅ. In addition, we did not consider lines whose lower level had excitation potentials of 0.0 eV or close to this value, since, as a rule, these transitions are sensitive to non-LTE effects.

Table 3 presents the estimated elemental abundances in the atmospheres of the studied stars relative to those in the Sun, specified by the relation

$$[\mathrm{X}] = \log[\epsilon(\mathrm{el})/\epsilon(\mathrm{H})]_* - \log[\epsilon(\mathrm{el})/\epsilon(\mathrm{H})]_\odot. \quad (1)$$

The number of lines used for the abundance determinations are given for each star in the corresponding column (N); the metallicities [M], specified as the averaged abundances (relative to the Sun) of the iron-group elements (Ti to Ni) are also presented. Figure 2 displays the elemental abundances for each of the studied stars.

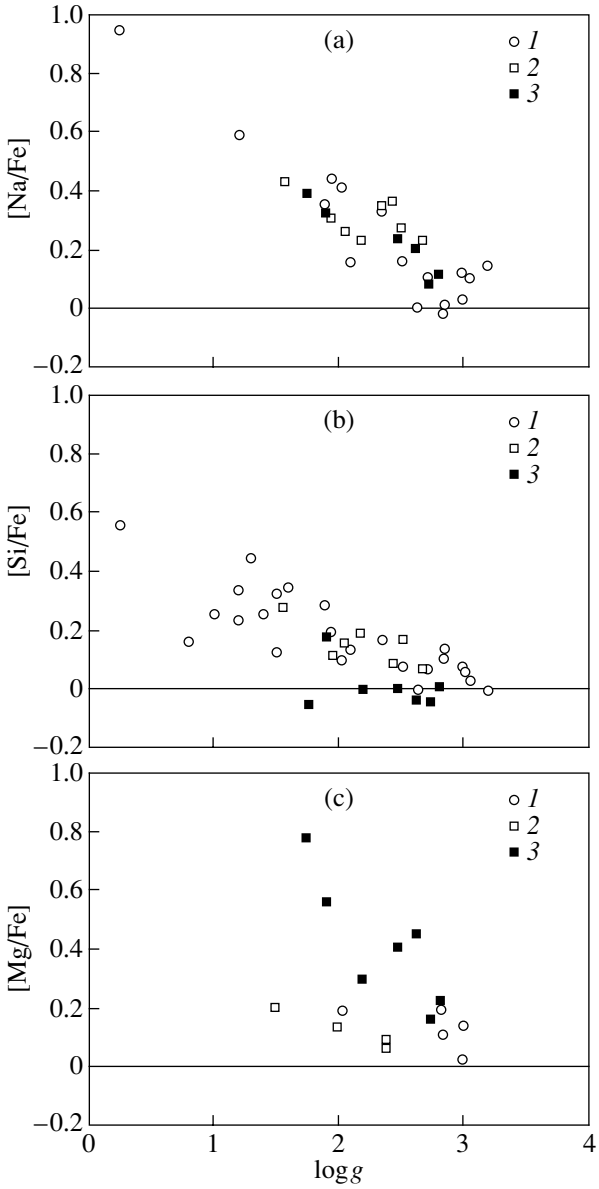

Fig. 3. Excesses of (a) [Na/Fe], (b) [Si/Fe], and (c) [Mg/Fe] in the atmospheres of red giants compared to the Sun. Shown are data for (1) normal giants and supergiants [34], (2) moderate barium stars [34], and (3) classical barium stars (this study).

It follows from Table 3 that the various studied stars have somewhat different metallicities [M]. Although these values are determined fairly reliability (with a relatively small scatter), we will further consider the ratio of the elemental abundances to the abundance of iron, which is determined with the

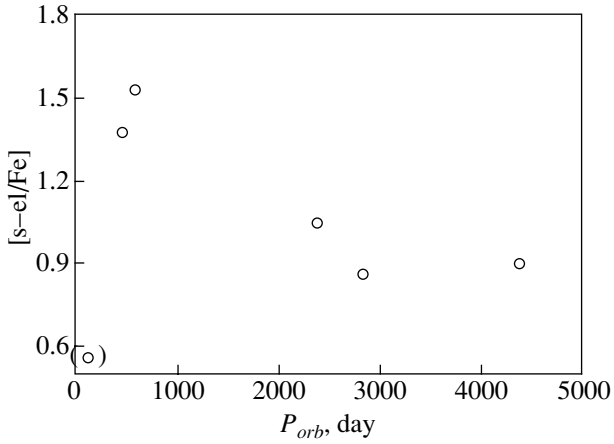

Fig. 4. Abundances of *s*-process elements in the atmospheres of the studied classical barium stars as a function of their orbital periods. HD 77247 is marked by the (○).

highest accuracy due to the large number of observed Fe spectral lines. Note that the studied stars display positive values of [Na/Fe], [Si/Fe], and [Mg/Fe]; i.e., these elements are overabundant. We plotted these excess abundances as a function of $\log g$ (i.e., versus luminosity), as had previously been done for normal red giants and supergiants, and also for moderate barium stars (see Figs. 3a–3c). The anomalous overabundances of classical barium stars are in good consistency with these relationships. We conclude that the anomalous abundance excesses observed for all these groups of stars—supergiants, normal red giants, moderate barium stars, and classical barium stars—have a common origin.

As we can see from Table 3, some of the stars display a modest (compared with the Sun) carbon excess. Qualitatively, this suggests we are observing matter from a region of helium burning. However, quantitative estimates should be treated with caution. The excitation potentials of the observed carbon lines are high; for this reason, and given the low temperatures in the atmospheres of red giants, the resulting carbon abundances may be fairly uncertain. The carbon abundances of red giants derived from analyses of molecular bands are most trustworthy, but this requires specialized methods and observations. We were not aiming to address this problem, and, therefore, having noted the qualitative consistency, we will further use data from the literature to analyze the carbon abundances.

As expected, the abundances of *s*-process elements are high and show relatively little scatter. It is striking that the zirconium abundances determined from the ZrI and ZrII lines are in poor agreement. The lines of neutral zirconium are numerous, and the corresponding abundances show only a modest scatter about the average value. Only two lines of ionized zirconium were observed. It would seem preferable to determine the Zr abundance from the ZrI lines. However, the results for different stars indicate that the difference in the abundances determined from the two types of lines depends on $\log g$ (Table 3). The ZrI lines are apparently affected by deviations from LTE (although the excitation potentials of the lines used are 1–1.5 eV), which should decrease with increasing $\log g$; i.e., with increasing density (as is indeed observed). The abundances determined from the ZrII lines are consistent with those of other elements originating primarily via the *s* process (along with Zr, these include Sr, Y, Ba, La, Ce, Pr, and Nd), and they should probably be given preference. The same is true for Y. Since the atoms of various *s*-process elements have similar compositions, it is very likely that abundances for these elements based on lines for their neutral states should be treated with caution, even if the lines are not related to the ground state. In contrast to these elements, the atoms of Mo, Sm, Eu, Dy, and Hf do not originate entirely due to the *s* process; they form partly as a result of the *r* process. This may be the reason for their somewhat lower abundances.

The abundance excesses for various elements originating mainly due to slow neutron capture (the *s* process) are fairly similar. For each star, the abundances of these elements can be characterized by the average of the abundances of individual elements, determined by the relation

$$[\text{s–el/Fe}] = [\text{SrI}] + [\text{ZrII}] + [\text{YII}] + [\text{CeII}] + [\text{LaII}] + [\text{NdII}] + [\text{PrII}]/7 - [\text{Fe}]. \quad (2)$$

Table 2 presents these average abundances for each star. Here, we have not used the BaII lines due to their high intensities and the expected influence of non-LTE effects. Table 2 indicates that the typical scatter of the abundances of these elements about the mean value is modest, comparable to the scatter of the abundances for individual lines. The excess abundances of *s*-process elements are from +0.5 to +1.5 dex.

3. THE LUMINOSITIES OF THE STARS

Further analysis of the properties of our program stars requires knowledge of their luminosities, which can be estimated using the data in Table 4. The apparent magnitudes, $B-V$ color indices, and parallaxes (columns 2, 4, and 8) are taken from the HIPPARCOS catalog [39]. Note that, when the HIPPARCOS data were being collected, many binary barium stars had not yet been identified as binaries, and the astrometric parameters (parallaxes and proper motions) published in [39] were obtained assuming that these stars were single. As was noted in [40, 41],

Table 4. Luminosities of the studied stars

HD	m_v (HIP)	m_v (Ph)	$B-V$ (HIP)	$B-V$ (Ph)	N	$(B-V)_0$	π milliarcsec (HIP)	r, pc (HIP)	A_v^a	M_V	T_{B-V}, K (HIP)	BC	M_{bol}	$\log\left(\frac{L_*}{L_\odot}\right)$
1	2	3	4	5	6	7	8	9	10	11	12	13	14	15
46407	6.30	6.26	1.096	1.11	7	1.07	8.25	121	0.083	+0.78	4660	−0.56	+0.22	1.81
65854	8.41	8.41	0.976			0.96	6.34	157	0.051	+2.35	4930	−0.42	+1.93	1.13
77247	6.87	6.86	0.999			0.96	2.86	349	0.125	−0.92	4870	−0.35	−1.27	2.41
199394	7.00	7.01	1.002	1.01	3	0.96	6.33	157	0.134	+0.78	4850	−0.39	+0.39	1.74
199939	7.44	7.45	1.238	1.24	2	1.07	3.16	316	0.538	−0.52	4350	−0.67	−1.19	2.38
204075	3.77	3.74	1.002	1.00	11	0.81	8.19	122	0.000	−1.83	4880	−0.39	−2.22	2.79
205011	6.43	6.43	1.064			1.01	6.31	158	0.173	+0.33	4730	−0.49	−0.16	1.96

[a] $A_v = 3.2 * E_{B-V}$,
$E_{B-V} = (B-V) - (B-V)_0$.

the neglected orbital motions may have introduced so-called "space errors"; i.e., a real orbital displacement can be interpreted as a false parallax shift or can be falsely added to the shift resulting from the proper motion. This problem was analyzed in detail in [42], where it was concluded that the HIPPARCOS parallaxes are equal to their true values for all unidentified binaries excepting those whose orbital periods are close to a year. Thus, the parallaxes of our stars, and hence the absolute magnitudes calculated on their basis, can be considered trustworthy, with the possible exception of the parallax of HD 46407.

The interstellar absorption was estimated from the reddening of $B-V$ ($A_v = 3.2 \times [(B-V)_* - (B-V)_0]$). We first compared the HIPPARCOS $B-V$ estimates [39] (see column 4 in Table 4) with those obtained from ground-based photometry (the SIMBAD database). Column 6 of Table 4 indicates the number of such measurements, while column 5 contains the average $B-V$. A comparison of columns 4 and 5 clearly show that the two data sets are consistent. We determined the $(B-V)_0$ values from the spectral type of the star. In our calculations of the interstellar absorption, we used the data from the column 4; the results of the calculations are given in column 10. The calculated distances to the stars r, absolute magnitudes M_v, bolometric corrections BC, bolometric magnitudes M_{bol}, and luminosities $\log(L_*/L_\odot)$ are given in columns 9, 11, 13, 14, and 15 of Table 4.

The $B-V$ color index was also used to estimate the effective temperatures of the objects. Note that the effective temperature determined as one parameter of the model atmosphere from a given model grid providing the best fit of the observed spectrum does not always coincide with the effective temperature derived from the continuum spectral energy distribution, as was noted in [30, 33]. It was proposed that this inconsistency was due to imperfection of the model atmospheres. Therefore, we used the data from column 4 of Table 4 to estimate the temperatures of the objects using the calibration we constructed based on the temperatures derived from the stellar diameters and IR observations. The resulting temperatures are given in column 12 of Table 4. Further, we used these

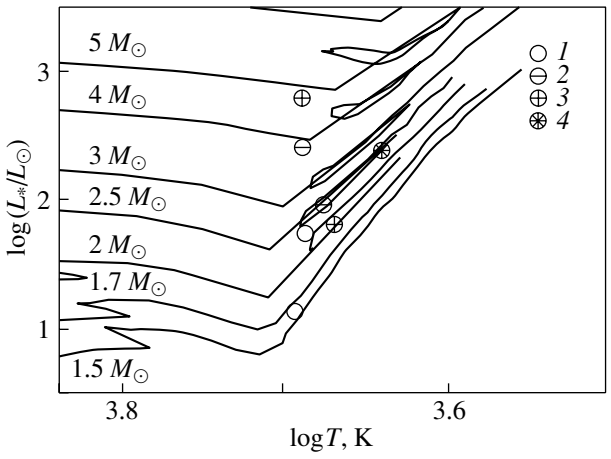

Fig. 5. The studied classical barium stars in the HR diagram. The stars are denoted in accordance with the strength of their barium lines [2] (Table 1): (*1*) Ba1, (*2*) Ba2, (*3*) Ba3, and (*4*) Ba4.

values to analyze the positions of the stars in the $\log T - \log(L_*/L_\odot)$ diagram.

4. ANALYSIS AND DISCUSSION

Currently, the most popular hypothesis is that barium stars originate within binaries. This predicts an inverse dependence between the excess of s-process elements and the orbital period: the shorter the period, i.e., the closer the components, the larger the amount of material enriched in s-process elements that is lost by the evolved component and falls onto its companion, transforming it into a barium star. The observations confirm this dependence (see, for example [13]). This hypothesis is also supported by the high proportion of binaries among classical barium giants compared to normal giants. Figure 4 presents the excess of s-process elements as a function of the orbital period for our stars. It is obvious that HD 77247 does not follow this dependence. As the barium star with the shortest orbital period, it should display the largest excess of s-process elements. For brevity, we will call the degree of enrichment of s-process elements in a stellar atmosphere the "barium degree." This excess, or barium degree, for HD 77247 is an order of magnitude lower than expected based on this dependence. This discrepancy cannot be explained by the observational errors and the uncertainties in the atmospheric parameters. There may be some other factor that affects the barium degree of this star, in addition to binarity.

Note that some non-barium binaries have the same types of components (a white dwarf and cool giant), periods, and eccentricities as barium stars. These stars were studied in [43], where it was concluded that binarity on its own is not a sufficient condition for the formation of a barium star, and that the mass-transfer rate probably plays an important role.

Figure 5 illustrates the position of the studied stars in the $\log T - \log(L_*/L_\odot)$ diagram. The evolutionary tracks were constructed based on the data of [44]. The temperatures and luminosities of the stars are taken from Table 4 (see also Section 3). The position of each star is denoted by a symbol corresponding to its barium-line-strength index according to [2] (see captions to Fig. 5 and Table 1). The higher this index, the stronger the lines of barium and other s-process elements, i.e., the larger their overabundances in the stellar atmospheres [2]. Table 2 presents mass estimates for each star determined from their positions relative to the evolutionary tracks in Fig. 5. We can see from this figure that stars with relatively large barium degrees tend to be in areas of lower temperatures or higher mass; i.e., for the classical barium stars considered, the barium degree increases with the evolution of the star. We noted a similar pattern for moderate barium stars, and suggested that this is due to different degrees of convection (mixing) in stars of different masses with, accordingly, different amounts of nucleosynthesis products being carried to the stellar surfaces from the interiors [32].

Figure 5 also shows that several stars possess similar temperatures but different masses. Figure 6 presents the dependence of the abundances of s-process elements [s-el/Fe] on the stellar mass for these stars, according to the data from Table 2. It is clear that, in general, the abundances of these elements tend to increase with increasing mass; however, HD 77247 again falls away from this dependence. The abundance of s-process elements in its atmosphere is roughly 0.5 dex lower than it should be according to this dependence. As was noted above, this discrepancy cannot be explained by the errors in the observations or the atmospheric parameters. The study [13] also presents low estimates for this star's abundances of s-process elements. We thus conclude that the abundances of s-process elements obtained for HD 77247 are inconsistent with the established dependence between the excess of s-process elements and the stellar mass.

Note that HD 77247 also differs from the other program stars in its metallicity, which exceeds the solar value ($+0.07 \pm 0.04$ dex), Table 2). The stellar population of the Galactic disk is a mixture of objects with a range of ages, rather than a homogeneous group. Taking the metallicity as an age index, we conclude that HD 77247 is the youngest of the stars considered.

Thus, compared with the other classical barium stars, HD 77247 displays a high mass, high metallicity (Table 2), and young age. In the framework of the hypothesis that classical barium stars are single (or evolve unaffected by their companions), this may indicate that other factors (such as mass) being equal, the mixing in HD 77247 is less developed than in other barium stars that have the same mass and temperature but lower metallicities, i.e., that are older. Qualitatively, the same effect—a decreased abundance of s-process elements with increased metallicity—was noted previously in the study of red giants [31]. In addition, we note that the very young Hyades-cluster red giants do not display any overabundances of s-process elements [34].

Analysis of the properties of HD 77247 in the framework of the hypothesis that barium stars are binaries does not yield satisfactory results. As is noted above (see also Fig. 4), the abundances of s-process elements in its atmosphere are substantially lower than expected if it is accreting from a companion and the accreted matter is mixed with the material of the red giant's atmosphere. Given the short period of

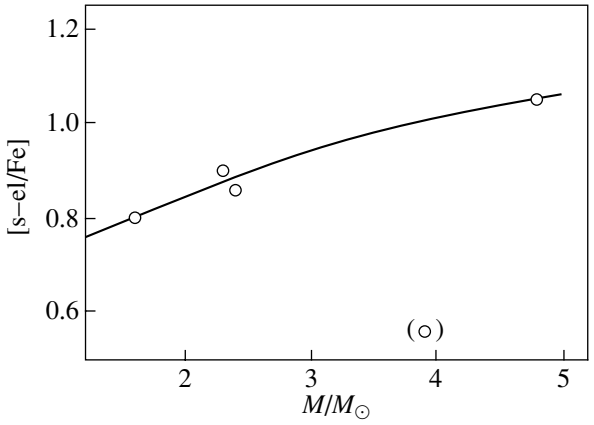

Fig. 6. Abundances of s-process elements in the atmospheres of the studied classical barium stars as a function of their mass. The position of HD 77247 is marked by the (○).

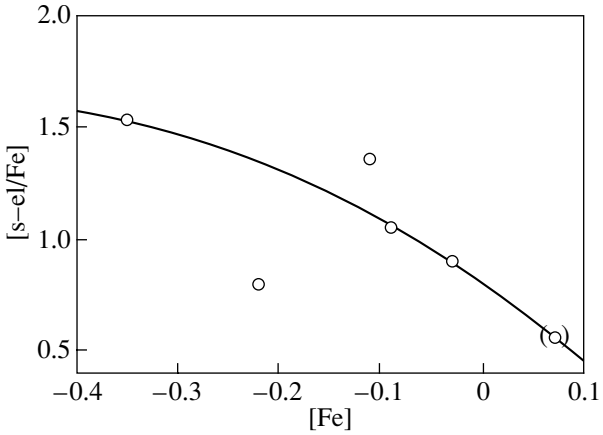

Fig. 7. Abundances of s-process elements in the atmospheres of the studied classical barium stars as a function of metallicity. The position of HD 77247 is marked by the (○).

the system (and the corresponding proximity of the components), the amount of accreted matter should exceed that for barium stars with longer periods. In addition, since the mass of HD 77247 is fairly large (about 4 $M_\odot$; Table 2), the mass of its companion would have to have been substantially higher, so that it would be able to reach its proposed present evolutionary stage of a white dwarf. In this case, we would expect to observe on the surface of the barium star matter reprocessed in nuclear reactions in the interior of a massive star at very late stages of its evolution. In other words, we would expect to detect larger overabundances of s-process elements than in the case of less massive donors. However, the excess abundances of these elements in the atmosphere of HD 77247 are the lowest of all the seven studied stars.

Thus, there must be another factor that affects the barium degree of HD 77247. It may be its high metallicity that makes this star different from the others studied. The study [45] of nucleosynthesis and mixing in stars located on the asymptotic giant branch and displaying a wide range of metallicities indicated that the overabundances of s-process elements should depend on metallicity. The calculations of [45] showed that this dependence is complex over a broad range of metallicities; however, in the metallicity interval of interest to us, [M] = 0.1–(–0.8) dex, we should observe a monotonic increase of the excess abundances of s-process elements with decreasing metallicity. Figure 7 presents this dependence for our program stars. We can see that the positions of HD 77247 and several of the other stars are consistent with this relation. Thus, in this star, the metallicity indeed exerts an appreciable influence on the barium degree. However, two stars do not follow this dependence, suggesting there may be some other factors playing the dominant role in specifying their overabundances of s-process elements.

It was shown in [31] that the overabundances of s-process elements in the spectra of red giants tend to increase with increasing stellar mass. It was also noted that, for the same temperature, gravitational acceleration, and mass, a star with a higher metallicity will display a lower abundance of s-process elements than a star with a lower metallicity. Our results show a qualitatively similar dependence between the abundances of s-process elements in the atmospheres of classical barium stars and the stellar masses (Fig. 6) and metallicities (Fig. 7), although the magnitudes of the abundance excesses in classical barium stars are substantially higher.

Modest overabundances of s-process elements were found earlier in the atmospheres of normal red giants [30]; higher abundances of these elements are displayed by the atmospheres of moderate barium stars [32]. The results we present here indicate very high (up to 1.5dex for individual stars) anomalous abundances in classical barium stars (here, we do not consider numerous sources in the literature, preferring to compare results obtained from homogeneous observational data using a single method). Despite the different barium degrees in these three cases,

Table 5. Comparison of the average data for moderate and classical barium stars

Barium stars	[Fe]	[C/Fe]	$^{12}C/^{13}C$	Z, pc	Number of stars
Moderate	–0.14	–0.30	20	98	17
Classical	–0.41	+0.09	15	276	13

the abundances of *s*-process elements within each group of objects behave qualitatively similarly: they increase with evolutionary phase, increasing stellar mass, and decreasing metallicity. We conclude that, in the case of classical barium stars, whose high barium degrees are, as a rule, determined by their binarity, the evolutionary phase, mass, metallicity, and possibly some other factors can play appreciable roles, and even, as in the case of HD 77247, very important ones.

Mennessier *et al.* [46] attempted to consider barium stars from the point of view of stellar evolution, analyzing the positions in the HR diagram of approximately three hundred stars with various barium-star signatures. The absolute magnitude M_v and height above the Galactic plane Z were calculated for each star based on the HIPPARCOS data. It was concluded that barium stars do not form a homogeneous group, and can be divided into five types according to their luminosity and kinematic properties. The average age and mass were determined for each of these five groups, and their evolutionary status was discussed. We collected published metallicities [Fe], carbon abundances [C/Fe], and isotope ratios $^{12}C/^{13}C$ for the stars from [46] (apart from the supposed halo stars and dwarfs, whose existence is subject to doubt and which we do not consider here). We divided all the stars for which these data were available into only two groups—moderate and classical barium stars. We calculated the average values of the above parameters for each of these groups, presented in Table 5. We can see that, based on the metallicity and Z values, the classical barium stars can be interpreted as being older than the moderate barium stars. In addition, the classical barium stars have positive carbon excesses, providing evidence for the presence of products of helium burning. The moderate barium stars show a carbon deficiency, as is characteristic for the phase of hydrogen burning via the CNO cycle.

In each of Figs. 4, 6, and 7 illustrating the dependences between the *s*-process element overabundances and the stellar masses, metallicities, and orbital periods, one or two different stars fall away from the dependences. We verified that these discrepancies could not be due to errors in the abundances. Thus, it is likely that the classical-barium-star phenomenon and a star's barium degree (the overabundance of *s*-process elements) cannot be fully explained using a single parameter—binarity, metallicity, mass, or evolutionary phase. In various particular cases, any of these parameters could become dominant in giving rise to the barium star and determining the degree of the anomalous *s*-process element abundances.

It is possible that two groups of barium stars exist. The stars of the first group evolve in the usual way, being unaffected by their companions, if they have any. The larger the luminosity of the star (which increases with the evolutionary phase), the higher the degree of mixing, which penetrates into deeper layers of the star and carries out more nucleosynthesis products from its interior. This scheme is illustrated by Figs. 6 and 7, which indicate the dependence between the overabundances of *s*-process elements and the stellar mass and metallicity. This is consistent with the results of [46], in which it was suggested that two of the five groups of barium stars (see above)—giants belonging to the "clump" group and supergiants—are post-core-helium-flash objects in which convection can carry *s*-process elements produced inside the stars to their outer layers.

The second group of barium stars contains stars in which mass transfer from one component of a binary to the other plays the dominant role in creating the barium star (classical barium stars). It is very likely in this case as well that the mass, metallicity, and evolutionary phase of the component currently observed as a barium star can affect the observed anomalous abundances of heavy elements.

These conclusions must be considered tentative, however, due to the small number of studied stars.

5. CONCLUSIONS

(1) Comparison of the elemental abundances in the atmospheres of the classical barium stars, moderate barium stars, and normal red giants [30, 32] indicates that the behavior of elements up to the iron peak is the same in all three groups of giants, providing evidence that they have a common origin.

(2) The dependences of the anomalous abundances of *s*-process elements on the stellar masses and metallicities are qualitatively similar for normal red giants and moderate and classical barium stars. This probably indicates that a substantial role is played by the evolutionary phase of the stars.

(3) The creation of a barium star and the magnitudes of the overabundances of *s*-process elements cannot be explained as the effect of a single parameter—binarity, mass, metallicity, or evolutionary phase. Any one of these parameters could be dominant in certain individual objects; however, this does not rule out the possibility that the other factors also simultaneously exert a significant influence.

6. ACKNOWLEDGMENTS

The study was partially supported by the Russian Foundation for Basic Research (project code 00-02-17660) and the State Program for Support of Leading Science Schools (project code 00-15-96722).

REFERENCES

1. W. P. Bidelman and P. C. Keenan, Astrophys. J. **114**, 473 (1951).
2. B. Warner, Mon. Not. R. Astron. Soc. **129**, 263 (1965).
3. R. H. Garstang, Publ. Astron. Soc. Pac. **64**, 227 (1952).
4. E. M. Burbidge and G. R. Burbidge, Astrophys. J. **126**, 357 (1957).
5. C. A. Pilachowski, Astron. Astrophys. **54**, 465 (1977).
6. S. Sneden, D. L. Lambert, and C. A. Pilachowski, Astrophys. J. **247**, 1052 (1981).
7. V. V. Smith, Astron. Astrophys. **132**, 326 (1984).
8. N. Kovacs, Astron. Astrophys. **124**, 63 (1983).
9. N. Kovacs, Astron. Astrophys. **150**, 232 (1985).
10. L. A. Zach, Soobshch. Spets. Astrofiz. Obs. **60**, 70 (1989).
11. L. A. Zach, Soobshch. Spets. Astrofiz. Obs. **63**, 160 (1989).
12. L. A. Zach, Soobshch. Spets. Astrofiz. Obs. **65**, 45 (1990).
13. L. Zacs, Astron. Astrophys. **283**, 937 (1994).
14. P. R. Wood, in *Cool Stars with Excesses of Heavy Elements,* Ed. by M. Jaschek and P. C. Keenan (Reidel, Dordrecht, 1985), p. 357.
15. R. G. Deupree, Astrophys. J. **303**, 649 (1986).
16. R. D. McClure, in *Cool Stars with Excesses of Heavy Elements,* Ed. by M. Jaschek and P. C. Keenan (Reidel, Dordrecht, 1985), p. 315.
17. R. D. McClure, J. M. Fletcher, and J. M. Nemec, Astrophys. J. Lett. **238**, L35 (1980).
18. R. D. McClure, Astrophys. J. **268**, 264 (1983).
19. R. D. McClure, Publ. Astron. Soc. Pac. **96**, 11 (1984).
20. S. Udry, A. Jorissen, M. Mayor, and S. Van Eck, Astron. Astrophys., Suppl. Ser. **131**, 25 (1998).
21. S. Udry, M. Mayor, S. Van Eck, *et al.*, Astron. Astrophys., Suppl. Ser. **131**, 43 (1998).
22. E. Bohm-Vitense, Astrophys. J. Lett. **239**, L79 (1980).
23. J. F. Dominy and D. L. Lambert, Astrophys. J. **270**, 180 (1983).
24. C. R. Cowley and P. L. Downs, Astrophys. J. **236**, 648 (1980).
25. V. V. Smith, Astron. Astrophys. **132**, 326 (1984).
26. R. A. Malaney, Astrophys. J. **321**, 832 (1987).
27. J. Tomkin J. and D. L. Lambert, Astrophys. J. **273**, 722 (1983).
28. V. V. Smith and D. L. Lamber, Publ. Astron. Soc. Pac. **96**, 226 (1984).
29. F. Käppeller, in *Nucleosynthesis and Its Implications on Nuclear and Particle Physics,* Ed. by J. Audouze and N. Mathieu (Reidel, Dordrecht, 1986), p. 253.
30. A. A. Boyarchuk, L. I. Antipova, M. E. Boyarchuk, and I. S. Savanov, Astron. Zh. **78**, 349 (2001) [Astron. Rep. **45**, 301 (2001)].
31. L. I. Antipova and A. A. Boyarchuk, Astron. Zh. **78**, 807 (2001) [Astron. Rep. **45**, 700 (2001)].
32. A. A. Boyarchuk, Yu. V. Pakhomov, L. I. Antipova, and M. E. Boyarchuk, Astron. Zh. **79**, 909 (2002) [Astron. Rep. **46**, 819 (2002)].
33. A. A. Boyarchuk, L. I. Antipova, M. E. Boyarchuk, and I. S. Savanov, Astron. Zh. **75**, 586 (1998) [Astron. Rep. **42**, 517 (1998)].
34. A. A. Boyarchuk, L. I. Antipova, M. E. Boyarchuk, and I. S. Savanov, Astron. Zh. **77**, 96 (2000) [Astron. Rep. **44**, 76 (2000)].
35. V. E. Panchuk, V. G. Klochkova, and I. D. Naĭdenov, Preprint No. 135 (Spec. Astrophys. Obs., Nizhniĭ Arkhyz, 1999).
36. V. E. Panchuk, N. E. Piskunov, V. G. Klochkova, *et al.*, Preprint No. 169 (Spec. Astrophys. Obs., Nizhniĭ Arkhyz, 2002).
37. N. E. Piskunov, F. Kupka, T. A. Ryabchikova, *et al.*, Astron. Astrophys., Suppl. Ser. **112**, 525 (1995).
38. R. L. Kurucz, Rev. Mex. Astron. Astrophys. **23**, 181 (1992).
39. *The Hipparcos and Tycho Catalogues* (Eur. South. Obs., Noordwijk, 1997), ESA SP-1200.
40. R. Wielen, Astron. Astrophys. **325**, 367 (1997).
41. R. Wielen, C. Dettbarn, H. Jahreis, *et al.*, Astron. Astrophys. **346**, 675 (1999).
42. D. Pourbaix and A. Jorissen, Astron. Astrophys., Suppl. Ser. **145**, 161 (2000).
43. L. Začs, F. A. Musaev, I. F. Bikmaev, and O. Asksnis, Astron. Astrophys., Suppl. Ser. **122**, 31 (1997).
44. G. Schaller, D. Schaerer, G. Meynet, and A. Maeder, Astron. Astrophys., Suppl. Ser. **96**, 269 (1992).
45. M. Busso, R. Gallino, D. L. Lambert, *et al.*, Astrophys. J. **557**, 802 (2001).
46. M. O. Mennessier, X. Luri, F. Figueras, *et al.*, Astron. Astrophys. **326**, 722 (1997).

Translated by K. Maslennikov

Astronomy Reports, Vol. 47, No. 8, 2003, pp. 660–669. Translated from Astronomicheskiĭ Zhurnal, Vol. 80, No. 8, 2003, pp. 717–727.

Simultaneous Dual-Frequency Observations of Giant Radio Pulses from the Millisecond Pulsar B1937+21

M. V. Popov[1] and B. Stappers[2]

[1] *Astro Space Center, Lebedev Institute of Physics, Russian Academy of Sciences, Profsoyuznaya ul. 84/32, Moscow, 117997 Russia*

[2] *ASTRON, P.O. Box 2, 7990 AA Dwingeloo, The Netherlands*

Received February 9, 2003; in final form, March 14, 2003

Abstract—Simultaneous dual-frequency observations of giant radio pulses from the millisecond pulsar B1937+21 were performed for the first time in January–February 2002 on the Westerbork Synthesis Radio Telescope (2210–2250 MHz) and the 64-m Kalyazin radio telescope (1414–1446 MHz). The total observing time was about three hours. Ten giant pulses with peak flux densities from 600 to 1800 Jy were detected at 2210–2250 MHz, and fifteen giant pulses with peak flux densities from 3000 to 10 000 Jy were observed at 1414–1446 MHz. No events were found to occur simultaneously at both frequencies. Thus, the observed radio spectra of individual giant pulses of this pulsar are limited in frequency to scales of about $\frac{\Delta\nu}{\nu} < 0.5$. The duration of the giant pulses is less than 100 ns and is consistent with the expected scattering timescale in these frequency ranges. Instantaneous radio spectra of the detected giant pulses were compared with the diffractive spectra obtained from ordinary pulses of the pulsar. In some cases, considerable deviations of the radio spectra of the giant pulses from the diffractive spectrum were revealed, which can be interpreted as indicating temporal structure of the giant pulses on timescales of 10–100 ns.

1. INTRODUCTION

Giant radio pulses are one of the most surprising phenomenon associated with the radio emission of pulsars. The peak flux densities of giant pulses frequently exceed those of ordinary pulses by factors of tens of thousands. Such powerful giant pulses have been observed in only two pulsars: the Crab pulsar, B0531+21 (see, e.g., Sallmen *et al.* [1]), and the millisecond pulsar B1937+21 (see the most recent study of Kinkhabwala and Thorsett [2]). B0531+21 is one of the youngest known pulsars, with a period of about 33 ms, whereas the first detected millisecond pulsar B1937+21 is one of the oldest, with a period of only 1.5 ms. However, these objects have two characteristics in common: first, they have a strong interpulse in addition to the main pulse, i.e., the magnetic axis of the neutron star is almost perpendicular to the rotation axis; second, both pulsars have magnetic fields at the light cylinder which are stronger than those in most other pulsars. According to this and some other criteria, searches for giant pulses from other pulsars have been carried out in recent years. Johnston *et al.* [3] and Kramer *et al.* [4] have reported the detection of anomalously strong micropulses from the Vela pulsar (B0833–45), and Romani and Johnston [5] have found some pulses exceeding the mean pulse strength by about an order of magnitude in pulsar B1821–24. Johnston and Romani [6] have also found similar "giant" pulses in pulsar B1706–44. Ershov and Kuz'min [7] have reported the detection of anomalously strong pulses from pulsar B1112+50 at 111 MHz. However, it remains unclear whether such strong pulses have the same nature as the giant pulses observed for B0531+21 and B1937+21.

The properties of the giant pulses from these two pulsars also differ in several respects. The giant pulses of the Crab pulsar (B0531+21) are in phase and observed within the main pulse or interpulse, whereas those of the millisecond pulsar B1937+21 are observed outside the main pulse and interpulse (at the trailing edge of the mean profile), within a very narrow time interval (± 3 μs). This particular feature of the giant pulses of B1937+21 was first confidently established by Kinkhabwala and Thorsett [2], who studied the giant pulses of this pulsar in detail using consecutive observations at three frequencies (430, 1420, and 2380 MHz) on the 300-m Arecibo radio telescope. They also pointed out another characteristic feature of the giant pulses of B1937+21: their extremely short duration, which was in all cases less than 1 μs. In fact, the giant pulses remained unresolved in time even with the 100-ns time resolution used by Kinkhabwala and Thorsett [2], so that these authors could only show that the observed shapes of giant pulses at

1063-7729/03/4708-0660$24.00

various frequencies are determined entirely by scattering on interstellar plasma inhomogeneities. The giant pulses of the Crab pulsar often have multiple components, with the durations of individual components being several microseconds and with these components having submicrosecond microstructure [8]. Soglasnov *et al.* [9] studied the giant pulses of B1937+21 at 1650 MHz with a time resolution of 31.25 ns on the 70-m Deep Space Network radio telescope at Tidbinbilla. They found 309 giant pulses in 39 min of observing time, the most powerful of which had a peak flux of about 60 000 Jy. All the detected giant pulses (except for one, which had multiple components) were unresolved, and their shape indicated scattering on a timescale of about 70 ns.

In January–February 2002, we carried out synchronous observations of the millisecond pulsar B1937+21 on the Westerbork Synthesis Radio Telescope (WSRT, 2210–2250 MHz) and the 64-m radio telescope in Kalyazin (1414–1446 MHz) in order to study the shapes and radio spectra of the giant pulses. The scattering timescale at 2210–2250-MHz should be about 25 ns, which is the time resolution provided by the PuMa recording system used in these WSRT observations. We report here the results of these observations.

2. OBSERVATIONS AND DATA PROCESSING

The observations were carried out on January 22, January 28, and February 3, 2002; each observing session lasted about one hour, and the total observing time was about three hours. At Westerbork, we used the specialized "Pulsar Machine" (PuMa) [10] system to record the pulsar signals, in a mode with direct recording of the video signals in four adjacent 10-MHz frequency channels. In Kalyazin, the video signal was also directly recorded in two adjacent 16-MHz frequency channels by the S2 recording system, intended for VLBI observations [11, 12]. The S2 recording was played back using a TCI interface developed at the Centre for Research in Earth and Space Technology (CRESTech) of York University (Toronto, Canada) and installed at the Astro Space Center of the Lebedev Institute of Physics. Both radio telescopes received right-hand circular polarization. The signal was recorded with two-bit sampling and four-level quantization. In Kalyazin, the boundary between low and high signal levels was set equal to the level of the rms fluctuations (1σ), while this boundary was set at the 2σ level for the WSRT. When decoding the signals, a correction depending on the current quantization level was applied, as described by Jenet and Anderson [13]. The decoded data were further processed using the predetector dedispersion method [14, 15]. In our case, the data processing consisted of calculating the Fourier transform of a decoded data set of duration T, with subsequent correction of the spectrum amplitudes for the nonuniform receiver passband and of the spectrum phases for the dispersion delay introduced into the radio signal during its propagation through the interstellar plasma. The phase corrections for corresponding harmonics of the Fourier spectrum were calculated as

$$\delta\phi(f) = \frac{2\pi \mathrm{DM}}{Df}\left(\frac{\Delta f}{f_0}\right)^2, \qquad (1)$$

where f_0 is the lower boundary of the recorded frequency band, f is the frequency for which the phase correction is calculated, $\Delta f = i\delta f$ is the deviation of this frequency from the limiting value f_0, i is the number of the spectrum harmonic, δf is the frequency step in the spectrum ($\delta f = \frac{1}{T}$), D is the dispersion constant ($D = 2.4100 \times 10^{-16}$ cm^{-3} pc s), and DM is the dispersion measure of the pulsar. This formula is derived from the relationship given by Hankins and Rickett [15].

After applying the amplitude and phase corrections to the spectrum, we calculated the inverse Fourier transform, which yields the actual restored signal. However, to perform digital detection (obtain the signal envelope), we must take the inverse Fourier transform of the corrected spectrum, in which the harmonics corresponding to negative frequencies are set to zero. This Fourier transformation yields a complex dataset, and the sum of the squares of the real and imaginary parts of each element of this dataset represents the required detected signal. To improve the time resolution, we can restore the signal over the full receiver bandwidth (2×16 MHz at Kalyazin and 4×10 MHz at the WSRT) by combining the spectra in adjacent frequency channels into a single synthetic spectrum and reducing the phase correction to a single frequency f_0 corresponding to the lower edge of the total band. In our case, this provides time resolutions of 31.25 ns at 1430 MHz and 25 ns at 2230 MHz.

We used the value DM=71.025 cm^{-3}pc, which was determined from the delay of the detected giant pulses between frequency channels during the data processing. We initially used DM=71.034 cm^{-3} pc, taken from Soglasnov *et al.* [9]. For this dispersion measure, the pulse smearing in a 16-MHz band at 1430 MHz is approximately 3280 μs, slightly less than two pulsar periods ($p = 1557.8$ μs). At 2230 MHz, the pulse smearing in a 10-MHz band is approximately 535 μs, or about one-third of the pulsar period. With such pulse smearing, data restoration only in time windows corresponding to the main pulse and interpulse is impossible at 1430 MHz

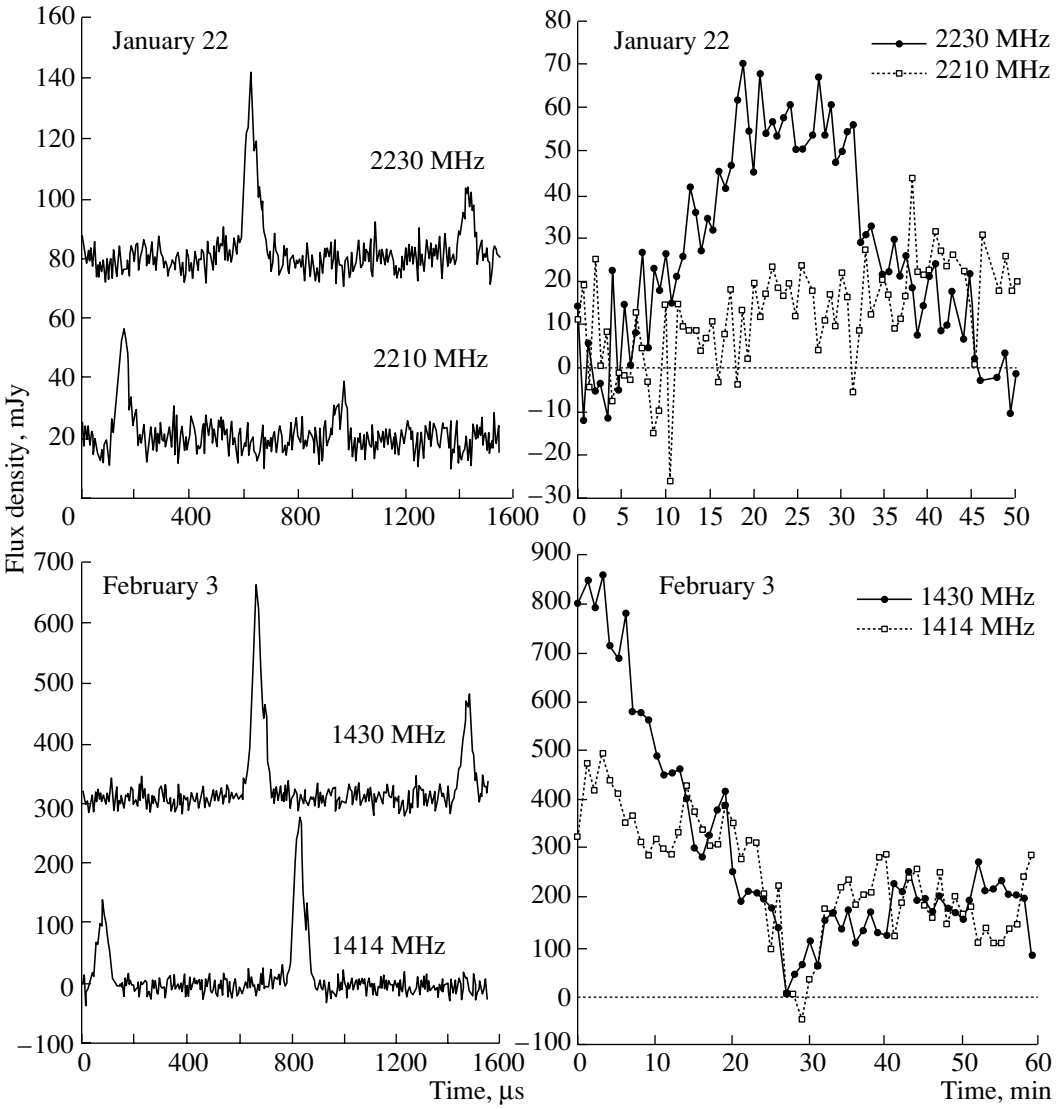

Fig. 1. Examples of mean profiles (left) and of the temporal behavior of the intensities of ordinary pulses (right) for selected observing sessions.

and inconvenient at 2230 MHz. Therefore, we restored the recorded signal in a piecewise continuous fashion. We used a time interval of 65.536 ms (a dataset of 2 097 152 points) when processing the Kalyazin recordings, and an interval of 26.2144 ms (524 288 points) for the WSRT recordings. To reconstruct the entire recording, we had to superimpose these time intervals with some overlap, since the information for a time segment equal to the timescale for the pulse smearing in the receiver band is lost each time.

In parallel with our search for giant pulses (using the algorithm described in Section 4), we accumulated the average profile over all frequency channels and calculated the radio spectrum of the restored and dedispersed, but not detected, signal in windows at the positions of the main pulse and interpulse, as well as in reference windows outside the pulse. We used these data to monitor the pattern of the diffractive distortions of the radio spectrum due to scattering on interstellar plasma inhomogeneities.

3. AVERAGE PROFILES AND DIFFRACTIVE SPECTRA OF THE SCINTILLATIONS

Figure 1 shows examples of average profiles obtained in an one-hour session in various frequency channels. For the WSRT data, the adjacent 10-MHz channels were combined when obtaining these mean profiles, so that the mean profiles in Fig. 1 were obtained for 2210–2230 MHz (lower profile) and 2230–2250 MHz (upper profile). The time delays between these frequency bands and between the 16-MHz

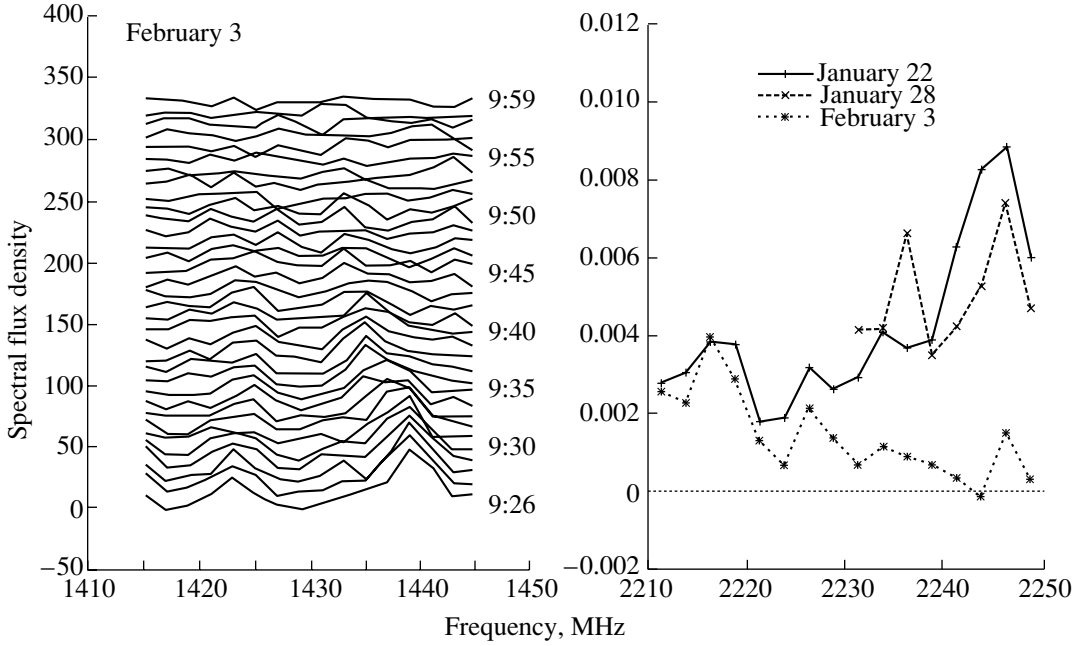

Fig. 2. Diffractive spectra due to scintillations on inhomogeneities of the interstellar plasma. The left panel shows the dynamic spectrum for the first 26 min of observations at Kalyazin on February 3, while the right panel shows the average spectra for each observing session at the WSRT (the January 28 observations were carried out only at 2230–2250 MHz).

bands for the Kalyazin data (1414, 1430 MHz), were not corrected in this figure. The flux-density scales are based on the equivalent system noise temperature at each radio telescope in Janskys, which we took to be 50 Jy for the WSRT and 150 Jy for the Kalyazin telescope. We believe that the uncertainty in these values is no greater than 10%. Figure 1 presents sample mean profiles obtained during the most successful sessions for each radio telescope, which were February 3 at Kalyazin and January 22 at the WSRT. Unfortunately, the modulation of the intensity of the pulsar radio emission by interstellar scintillations was unfavorable during our observations: the scintillation maxima at Westerbork fell predominantly at the scintillation minima at Kalyazin. The temporal pattern of the scintillations during the observing sessions for which the average profiles are presented is shown on the right in Fig. 1. The scintillation curves were obtained by calculating the average excess of the signal above the mean level outside pulses during time segments ("windows") corresponding to the position of the main pulse and interpulse. The durations of the time windows on the pulse and interpulse were 64 and 102.4 μs for the Kalyazin and WSRT data, respectively (2048 points). The averaging times were 1 min for Kalyazin and 40 s for the WSRT. We can see from Fig. 1 that the scintillation time scale is about 1 hour. During this time, the flux density of the pulsar radio emission varies by at least a factor of ten. The table lists measured values of the mean peak flux densities for the main pulse.

The study of the pattern of the radio-spectrum distortions due to diffractive scintillations is of great interest for the subsequent analysis. Figure 2 shows the mean diffractive spectra for three observing sessions at Westerbork and the dynamic spectrum obtained for 33 min of the observations at the beginning of the session of February 3 at Kalyazin. The pulsar intensity was highest in this time interval, as can also be seen from the scintillation curve in Fig. 1. We can distinguish two diffraction maxima in the dynamical spectrum in the total band of 1414–1446 MHz, which decay after 20 min. To determine the characteristic decorrelation bandwidth in the diffractive spectra, we constructed the mean autocorrelation function (ACF) of these spectra by adding together the individual ACFs computed for the difference between the spectra obtained on and outside the pulses. As a result,

Table. Measured peak flux densities for the main pulse (the January 28 WSRT observations were only at 2230 MHz.)

Date (2002)	F_{1414}, mJy	F_{1430}, mJy	F_{2210}, mJy	F_{2230}, mJy
January 22	190	130	40	65
January 28	250	165	–	65
February 3	265	350	30	8

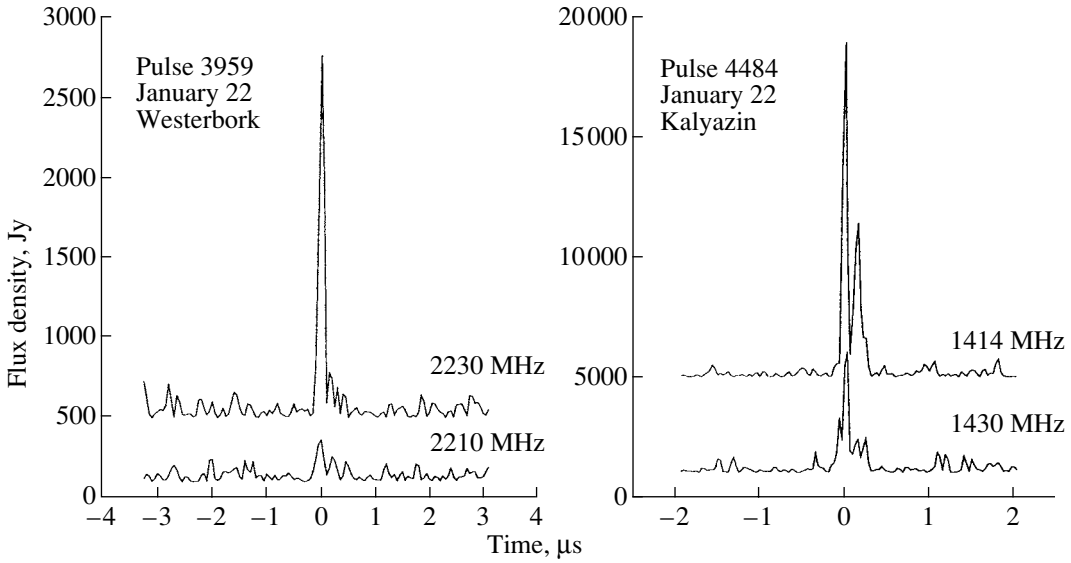

Fig. 3. Examples of giant pulses detected at 1430 and 2230 MHz.

we obtained the decorrelation bandwidths at the 0.5 level of the ACF: 1.5 ± 0.2 MHz at 1430 MHz and 9.6 ± 0.5 MHz at 2230 MHz.

4. CRITERION FOR THE GIANT-PULSE SEARCH AND THE SEARCH RESULTS

As was first clearly shown by Kinkhabwala and Thorsett [2], the giant pulses of B1937+21 appear within strictly limited longitude intervals, in two windows with widths of about 5 μs separated from the phase of the main pulse peak by 57 μs and from the phase of the interpulse peak by 65 μs. Soglasnov *et al.* [9] determined the positions of these windows more accurately; the corresponding delays turned out to be 58.2 and 66.6 μs, and the rms deviations in the arrival time of the giant pulses relative to the center of each window were 1.3 and 1.8 μs. We used this remarkable property in our search for new giant pulses and checked the intensity for an excess over some threshold only inside these narrow time intervals (± 5 μs). Since Soglasnov *et al.* [9] showed that the giant pulses remain unresolved in a 16-MHz band at 1650 MHz, we did not perform any averaging of the restored detected signal in our search for new giant pulses. The amplitude statistics of such a signal obey a χ^2 distribution with two degrees of freedom: $p(x > a) = \exp(-a)$, where the amplitudes of the analyzed signal are in units of the rms fluctuations σ of the signal. After reconstructing the signal using the predetector-dedispersion method at each pulsar's period, the amplitude of each sample inside the selected longitude windows was compared with the given threshold and, when the threshold was exceeded, the necessary information was saved for subsequent analysis. A one-hour session contains about 2.3 million periods of B1937+21, and there are two monitoring windows with a total duration of 400 samples in each period. Thus, about a billion tests for giant pulses were performed in each observing session. The expected number of random deviations in the detected signal obeying χ^2 statistics with two degrees of freedom is about a hundred for a 16σ threshold for each one-hour observing session, and only one random event is expected in such a session at a threshold of 21σ.

For subsequent comparison of suspected events at the two frequencies (1430 and 2230 MHz), we purposely selected a fairly low threshold for such events at each frequency. Since we have two adjacent frequency channels in the 1430-MHz band and four channels in the 2230-MHz band, we used an additional criterion to select events, namely an excess above the threshold simultaneously in two adjacent frequency channels, with a time delay corresponding to the adopted dispersion measure (the four frequency channels in the 2230-MHz band were processed in pairs: 2210–2220 MHz and 2230–2240 MHz). Thus, the initial selection threshold for the events was set at 16σ, and events exceeding the 16σ threshold in at least one of the two channels or having a total level of 16σ in the two frequency channels were recorded (e.g., 14σ in one channel and 2σ in the other, or 10σ in one channel and 6σ in the other).

In total, we compiled a list of several hundred events at each frequency. A comparison of the recorded events in the 1430- and 2230-MHz bands taking into account the dispersion delay between these frequencies and the geometrical delay between the

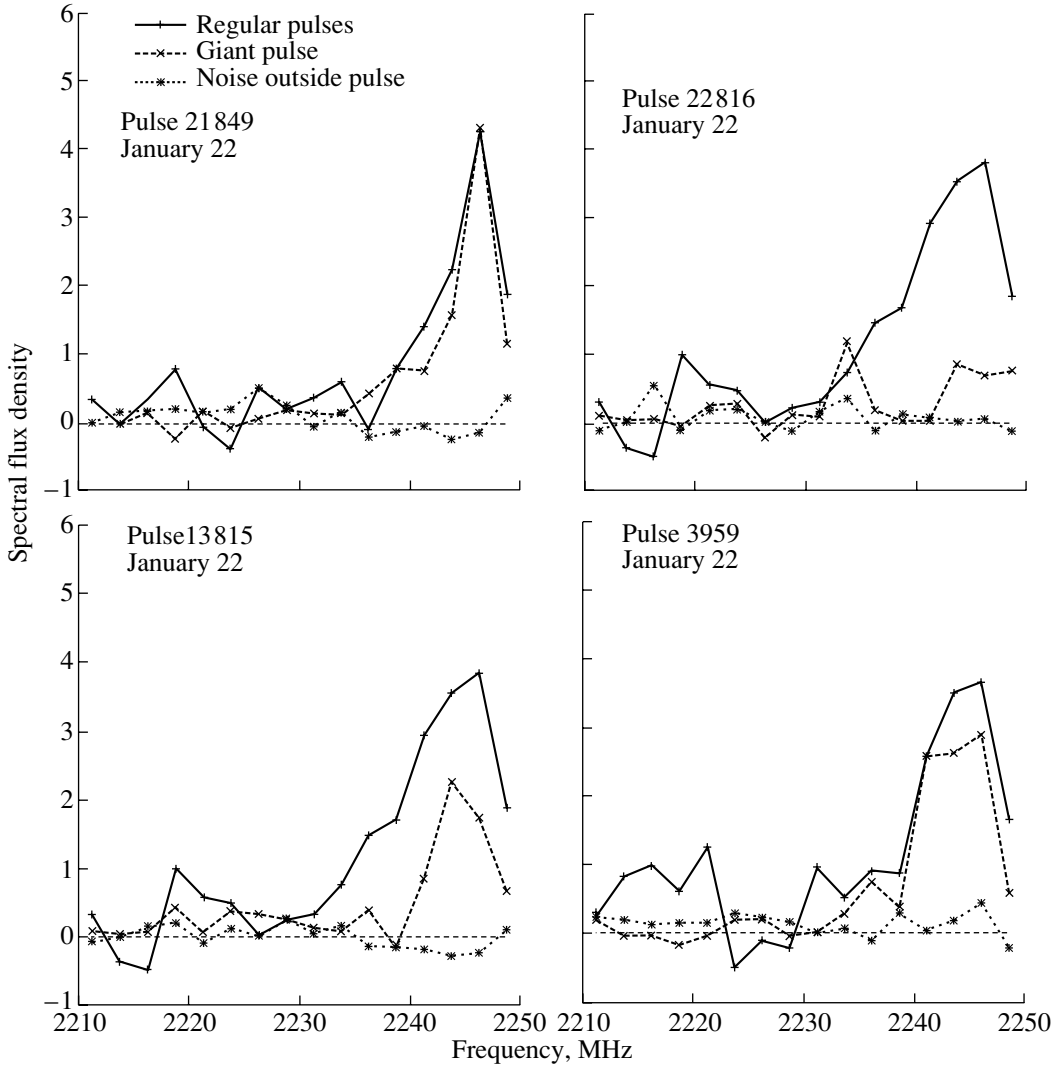

Fig. 4. Comparison of the radio spectra of selected giant pulses (pluses) with diffractive spectra derived from ordinary pulses (crosses) at 2230 MHz. To demonstrate the uncertainty in the spectral flux density of the giant pulses, the flux densities for the signal outside the pulsar pulse are also shown (asterisks).

observation points revealed no coincident events. We then included in the final list of detected giant pulses only those events exceeding the 21σ threshold in one frequency channel or in two adjacent channels using the above criterion. There were 15 such events at 1430 MHz and 10 at 2230 MHz. The strongest giant pulses at 1430 MHz and 2230 MHz had amplitudes of 63σ (9450 Jy) and 36σ (1800 Jy), respectively. These pulses are shown in Fig. 3.

For the 15 Kalyazin events, we carefully analyzed the selected segments of the WSRT data at the corresponding time intervals to search for excesses above the noise level. The accuracy with which we determined the dispersion measure from the time delay of the detected giant pulses between the frequency channels in the 1430- and 2230-MHz bands (71.025 ± 0.001) provides a time alignment between the 1430- and 2230-MHz signals to within about 1 μs. Accordingly, we searched the WSRT recordings for outbursts that could correspond to the Kalyazin events within an interval of ± 20 readings. In this interval, the outburst amplitude should exceed the 6σ level if we are to consider it to be significant with 90% confidence. No counterparts were found for any of the 15 Kalyazin giant pulses. A similar procedure was carried out for the ten Westerbork events using the Kalyazin recordings, with the result again being negative. Thus, the observed radio spectrum of the giant pulses we have recorded is limited in frequency to scales of at least $\frac{\Delta\nu}{\nu} < 0.5$. In the next section, we will consider the radio spectra of the individual giant pulses at 1430 and 2230 MHz.

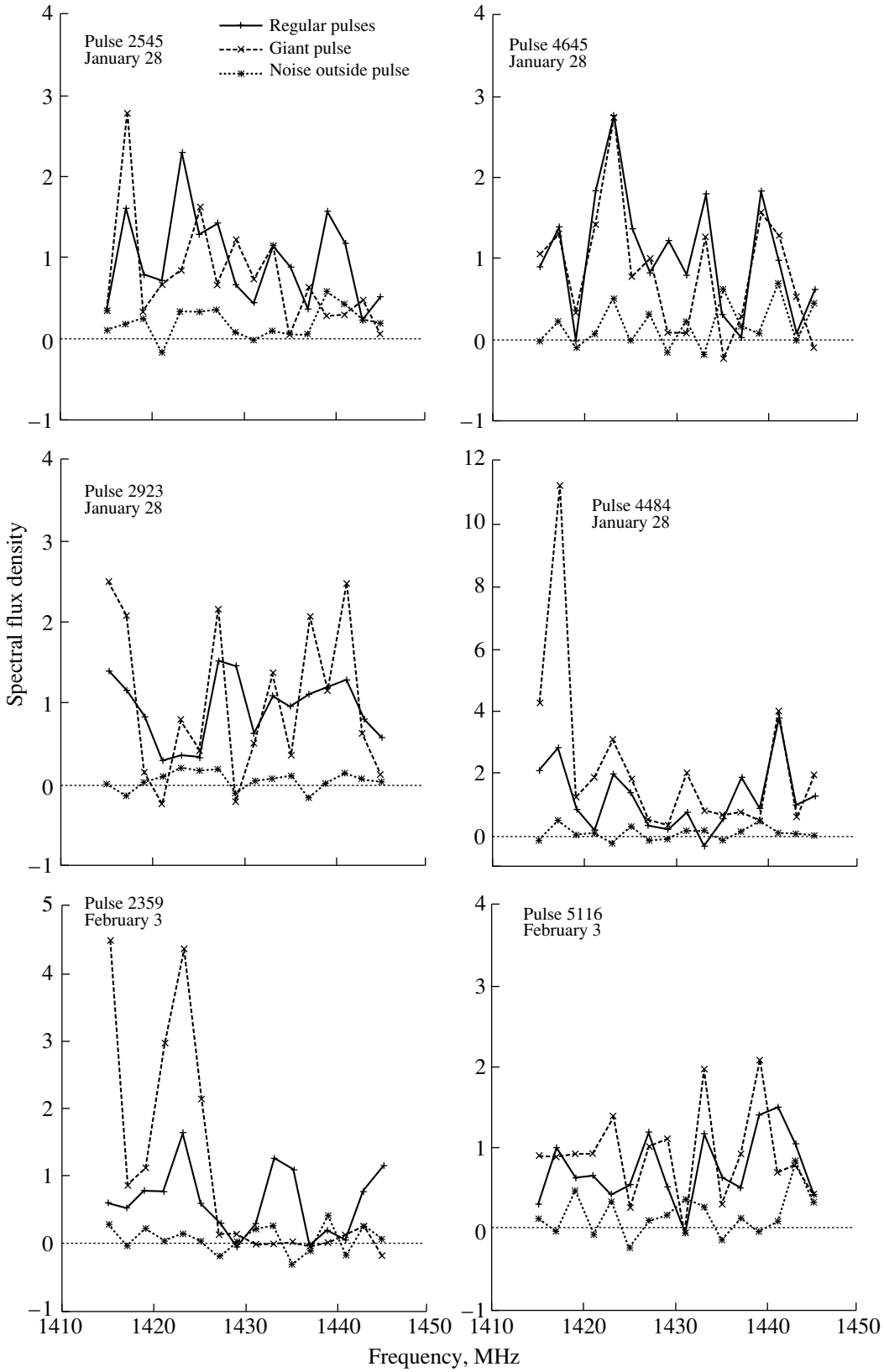

Fig. 5. Comparison of the radio spectra of selected giant pulses with diffractive spectra derived from ordinary pulses at 1430 MHz. The notation is the same as in Fig. 4.

5. RADIO SPECTRA OF INDIVIDUAL GIANT PULSES

We obtained the radio spectra of individual giant pulses by restoring the signal using the predetector-dedispersion method in individual spectral bands with bandwidths of 2.5 MHz for the WSRT data and 2.0 MHz for the Kalyazin data. Figures 4 and 5 show these radio spectra together with the diffractive scintillation spectra obtained for the ordinary pulses in three-minute intervals corresponding to the times of the giant pulses. Spectral flux-density fluctuations outside the pulse are also shown to demonstrate the uncertainties in the estimated spectral flux densities; these estimates were obtained using the same technique of numerical detection of the signal in the above spectral intervals, as for the giant pulses.

A comparison of the radio spectra of the giant pulses with the diffractive spectra at 2210–2250 MHz shows that the spectrum of some pulses repeat the diffractive spectrum within the errors (pulses 21 849 and 3959 in Fig. 4). Therefore, the radio spectra of such pulses are broader than 40 MHz, and their durations are less than 25 ns. The radio spectrum of pulse 13 825 is slightly narrower than the diffractive spectrum, while the radio spectrum of pulse 22 816 is fundamentally different from the diffractive spectrum. The same pattern is observed at 1414–1446 MHz (Fig. 5): the spectra of some giant pulses satisfactorily fit the diffraction pattern (pulses 4645, 2923, 5116), whereas the spectra of other giant pulses display an appreciable excess spectral flux density at some frequencies or a lack of radiation near diffraction peaks (pulses 4484 and 2359). In such cases, the scale for frequency modulations of the giant-pulse radio spectra is about 10 MHz. This modulation can be interpreted as a reflection of fine temporal structure of the giant pulses on time scales of 10–100 ns.

6. DISCUSSION

The most important result of our study is the limited extent in frequency of the radio spectra of giant pulses from the millisecond pulsar B1937+21. Giant radio pulses were detected in our synchronous observations at 1430 and 2230 MHz. If we compare the peak flux densities for the two brightest pulses detected at each frequency, we find a spectral index of -3.7 for a power-law frequency dependence of the peak flux density. If we perform the same procedure for all the detected giant pulses, we obtain a spectral index of -2.6. Kinkhabwala and Thorsett [2] obtained a spectral index of -3.1 in the same way. However, our synchronous observations have shown that individual giant pulses have a radio spectrum limited in frequency to scales $\frac{\Delta\nu}{\nu} < 0.5$. This is especially convincingly demonstrated by the absence of any traces of the Westerbork 2230-MHz giant pulses in the Kalyazin recordings. Any giant pulse exceeding the adopted 21σ threshold at 2230 MHz has a peak flux density higher than 1000 Jy, and the expected peak flux density of such a pulse at 1430 MHz should be about 4500 Jy (30σ) for the most conservative spectral index of -2.6. In fact, no 1430-MHz counterparts for the ten Westerbork giant pulses exceeding 6σ (900 Jy) were detected at the presumed positions of such pulses. Consequently, this would require that the spectral indices for all ten Westerbork giant pulses be positive and greater than 1.0. On the other hand, all 15 Kalyazin giant pulses would have to have spectral indices more negative than -5.0 for their amplitudes to be below the 6σ (300 Jy) level in the Westerbork recordings.

In his report of the results of simultaneous VLA observations of giant pulses from the Crab pulsar at 4.9 and 1.4 GHz, Hankins [8] showed that the spectral indices of giant pulses recorded simultaneously at these frequencies were generally distributed in a broad interval from 0 to -4, with a maximum between -1.5 and -2.0, but with two pulses with a spectral index of $+2$ also being observed. This study shows that the radio spectra of individual giant pulses from the Crab pulsar cannot be represented by a simple exponential function, much less by a single spectral index. However, to explain the absence of simultaneous giant pulses from the millisecond pulsar B1937+21 at 1430 and 2230 MHz as random variations of their radio spectra (similar to those observed for giant pulses of the Crab pulsar), we must suppose a special sorting of the giant pulses according to their spectra, which seems extremely improbable. It is possible that the relatively narrow-band radio spectrum of the giant pulses of this millisecond pulsar is one more distinctive feature of these pulses as compared to the giant pulses of the Crab pulsar.

These pulses also have other characteristic features, as was noted in the Introduction: the giant pulses from the millisecond pulsar appear in very narrow longitude intervals outside the mean profiles of the main pulse and interpulse, and these giant pulses have extremely short durations, remaining unresolved in all observations to date. Comparing the radio spectra of individual giant pulses with the diffractive spectra, we were able to show that some giant pulses can have multiple components on timescales of 10–100 ns.

7. CONCLUSIONS

Giant radio pulses from the millisecond pulsar B1937+21 represent the most short-lived phenomena ever observed in an astronomical object. Timescales of 10–100 ns correspond to spatial scales

of 3–30 m. The measured instantaneous power of the giant radio pulses implies a brightness temperature for the radiation of about 10^{38} K [9]. There is no doubt that, studying the properties of giant radio pulses, we are coming close to investigating the actual generation of coherent radio emission in a nonstationary stream of relativistic electron–positron plasma in the magnetosphere of a neutron star. At present, there is no generally accepted model for this coherent mechanism, in which the energy release is apparently rather sensitive to particular local parameters of the plasma; minor changes of these parameters (for instance, the density or distribution function of the relativistic particle energies) can result in huge changes in the instantaneous power of the radio emission.

Models for the formation of short micropulses in pulsar radio emission are based on nonlinear effects arising from interaction of a stream of charged relativistic particles with plasma waves in the pulsar magnetosphere (see, e.g., [16]). Weatherall [17, 18] has numerically simulated the development of instability in a turbulent flow of relativistic plasma. In this model, the origin of the electrostatic turbulence is the two-stream instability. When the turbulence becomes nonlinear, modulation instability results in the collapse of the wave packet along the magnetic field, leading to the generation of short radio pulses with durations of several nanoseconds and with a fairly narrow spectral bandwidth $\frac{\Delta\nu}{\nu} \sim 0.2$ near the local plasma frequency in the comoving coordinate frame.

This model agrees well with our conclusion that the frequency bandwidth of individual giant radio pulses from the millisecond pulsar B1937+21 is relatively narrow. Eilek *et al.* [19] indicate that, though the giant pulses of the Crab pulsar are observed simultaneously in a broad frequency band (at least from 1.4 to 4.8 GHz), the fine structure of these pulses is correlated only in narrow frequency intervals: 1.4–1.7 GHz, 4.5–5.0 GHz, and 8.4–8.5 GHz. For giant pulses of the Crab pulsar, the durations of pulse structural features are correlated with their intensities, in the sense that shorter features have primarily greater intensities [19]; precisely such a relation is predicted by nonlinear models for the generation of nanosecond pulses. It would be easier to study this relation using giant pulses from a millisecond pulsar, in which there is no need to select structural features, since the majority of these pulses have only one component. However, the temporal broadening of the pulse due to scattering on interstellar plasma inhomogeneities limits the time resolution to several tens of nanoseconds, even at 2230 MHz, as we have shown in this work (Fig. 2). Therefore, the actual shapes of giant pulses of the millisecond pulsar B1937+21 can be studied only using the 300-m Arecibo radio telescope at 5 GHz.

To conclude, we point out an interesting hypothesis explaining the origin of giant pulses. Istomin [20] considers they may be associated with the reconnection of limiting open magnetic lines near the zero line of the magnetic field in the vicinity of the light cylinder. For pulsars in which the rotation axis is almost perpendicular to the magnetic-dipole axis, such lines of force connecting two opposite magnetic poles emerge from regions having opposite signs for the equilibrium charge density of the magnetosphere. Reconnection of these force lines results in a short-lived electrical discharge between the poles, leading to the intense generation of energetic particles, which gives rise to a radio burst, observed as a giant radio pulse. Such giant pulses should arise in the region of the last closed line of force; i.e., at the very edge of the mean pulse profile, as is observed for the millisecond pulsar B1937+21.

ACKNOWLEDGMENTS

This work was supported by the Russian Foundation for Basic Research (project code 01-02-16871) and the State Science and Technology Program in Astronomy. M. V. Popov also received a NATO science grant (grant code NB 78-375), which supported his stay in the Netherlands for the data reduction. The authors are grateful to V. V. Oreshko for help with the complex of pulsar receiving equipment in Kalyazin, which is operated by the Pulsar Astrometry Department of the Pushchino Radio Astronomy Observatory, headed by Yu. P. Ilyasov. We also thank S. F. Likhachev and A. V. Chibisov for maintenance of the S2-TCI data-processing interface.

REFERENCES

1. S. Sallmen, D. C. Backer, T. H. Hankins, *et al.*, Astrophys. J. **517**, 460 (1999).
2. A. Kinkhabwala and S. E. Thorsett, Astrophys. J. **535**, 365 (2000).
3. S. Johnston, W. van Straten, M. Kramer, *et al.*, Astrophys. J. Lett. **549**, L101 (2001).
4. M. Kramer, S. Johnston, and W. van Straten, Mon. Not. R. Astron. Soc. **334**, 523 (2002).
5. R. W. Romani and S. Johnston, Astrophys. J. **557**, 93 (2001).
6. S. Johnston and R. W. Romani, Mon. Not. R. Astron. Soc. **332**, 109 (2002).
7. A. A. Ershov and A. D. Kuz'min, Pis'ma Astron. Zh. **29**, 1 (2003) [Astron. Lett. **29**, 91 (2003)].
8. T. H. Hankins, in *IAU Colloquium 177: Pulsar Astronomy – 2000 and Beyond,* Ed. by M. Kramer, R. Wex, and R. Wielebinski (Astron. Soc. Pac., San Francisco, 2000), Astron. Soc. Pac. Conf. Ser. **202**, 165 (2000).

9. V. A. Soglasnov, M. V. Popov, N. Bartel, *et al.*, submitted to Astron. Astrophys. (2003).
10. J. L. L. Voute, M. L. A. Kouwenhoven, P. C. van Haren, *et al.*, Astron. Astrophys. **385**, 733 (2002).
11. W. H. Cannon, D. Baer, D. G. Feil, *et al.*, Vistas Astron. **41**, 297 (1997).
12. R. D. Wietfeldt, W. van Straten, D. Del Rizzo, *et al.*, Astron. Astrophys., Suppl. Ser. **131**, 549 (1998).
13. F. A. Jenet and S. B. Anderson, Publ. Astron. Soc. Pac. **110**, 1467 (1998).
14. T. H. Hankins, Astrophys. J. **169**, 487 (1971).
15. T. H. Hankins and B. J. Rickett, Methods Comput. Phys. **14**, 55 (1975).
16. E. Asseo, Mon. Not. R. Astron. Soc. **264**, 940 (1993).
17. J. C. Weatherall, Astrophys. J. **483**, 402 (1997).
18. J. C. Weatherall, Astrophys. J. **506**, 341 (1998).
19. J. A. Eilek, P. N. Arendt, T. H. Hankins, and J. C. Weatherall, *Proc. of the 270th WE-Heraeus Seminar on Neutron Stars, Pulsars and Supernovae Remnants,* Ed. by W. Becker, H. Lesch, and J. Trumper, MPE Report No. 278 (Garching, Munchen, Max-Plank-Inst. Extraterr. Phys., 2002), p. 249.
20. Ya. N. Istomin, Astron. Zh. (2003, in press).

Translated by G. Rudnitskiĭ

Astronomy Reports, Vol. 47, No. 8, 2003, pp. 670–678. Translated from Astronomicheskiĭ Zhurnal, Vol. 80, No. 8, 2003, pp. 728–737.

Analysis of the Noise Background of the "ULITKA" Gravitational Antenna

A. V. Gusev, V. N. Rudenko, and A. V. Serdobol'skiĭ

Sternberg Astronomical Institute, Universitetskiĭ pr. 13, Moscow, 119992 Russia

Received March 14, 2003

Abstract—A long-term analysis of the noise background of the "ULITKA" gravitational-wave antenna is presented in connection with searches for anomalous impulsive signals and slow solar–terrestrial correlations with a period of 27 days. Automated selection and estimation algorithms are used, including nonparametric criteria for the statistical dependence of samples uniform in time. The upper limit for the gravitational-noise background is confirmed by the observational statistics. The presence of slow, anomalous correlations is not confirmed. © *2003 MAIK "Nauka/Interperiodica".*

1. INTRODUCTION

Long-term monitoring of the gravitational field is currently carried out using two global networks of gravitational detectors: one consisting of cryogenic gravimeters (to study variations of the vertical component of the gravitational force [1]) and another of cryogenic rigid gravitational antennas (to study variations of the longitudinal gradient of the gravitational field [2, 3]). The goal of the first of these networks is to detect fine global geodynamical effects due to slow dynamical processes in deep layers of the Earth, while the second network is intended for searches for weak gravitational perturbations at 10^2–10^3 Hz induced by gravitational waves from cosmic objects. Both systems currently have limiting sensitivities determined by their own instrumental noise: $\Delta g/g \approx 10^{-9}$–$10^{-11}$ for 100 s for the gravimeters and $h = \Delta L/L \approx 10^{-18}$–$10^{-21}$ for 1 s for the gravitational antennas. Several of the previous generation of such instruments continue to operate in a continuous-service regime: uncooled tidal gravimeters such as "SODIN" (10^{-6}–10^{-7}) and room-temperature gravitational antennas. One example of the latter is the uncooled "ULITKA" gravitational detector of the Sternberg Astronomical Institute of Moscow State University (10^{-16}–10^{-17}) [4]. The main argument for maintaining these systems is based on the possibility of detecting rare, anomalous events such as distant earthquakes, as well as nearby catastrophic cosmic events involving relativistic objects or explosive processes in the Sun. One such case was the detection of gravitational radiation by uncooled detectors during the explosion of supernova SN 1987A (52 kpc), which, however, was not subsequently reliably confirmed [5]. Recently, new data have indicated an excess of coincident flares by cryogenic antennas when the antenna beam has an optimum location in the plane of the Galactic disk [6]; this has also stimulated interest in a detailed analysis of the background noise of ULITKA.

In addition, gravitational instruments of this type represent one component of a long-term observational program on solar–terrestrial connections, which supposes the possible action of indirect gravitational effects via the Earth's atmosphere, ionosphere, etc. [7]. There are also groups of researchers who are trying to use such high-sensitivity equipment to search for non-standard global effects, or "new physics," such as gravitational screening during solar eclipses, magnetic polarization of the vacuum, and other global cosmic (cosmophysical) effects in the spirit of the Mach principle and so forth [8].

The noise background of ULITKA was used in this context by the group of Professor S. E. Snoll, to test their hypothesis that a universal cosmophysical force acts on various types of ground-based measuring devices [8–10]. Their analysis of long-term recordings by the ULITKA antenna based on the expert selection of smoothed empirical histograms (noise probability densities) led to the appearance of correlation peaks. One such peak has a characteristic period of 27 days. In principle, one possibility would be to try to explain this result as being due to the action on the antenna of Newtonian gravitational noise generated by a nonlinear parametric transformation of low-frequency perturbations of the atmosphere and the Earth's core (analogous to "acoustical emission" in geophysics). However, such estimates or references to such experiments are not given in [8–10].

In this connection, we undertook a reanalysis of the ULITKA noise background, avoiding as much as possible the application of subjective expert estimation. The results are presented below. We first briefly describe the structure and parameters of the

1063-7729/03/4708-0670$24.00

gravitational antenna, then present data on the statistics of its noise spikes. These data are important for estimating an empirical upper limit for the impulsive gravitational-wave background.

2. CHARACTERISTICS OF THE EXPERIMENTAL DATA

The ULITKA uncooled resonance gravitational antenna has been in a regime of quasicontinuous use since 1996. The basic device, properties of its construction, and the method used to form the resulting database are described in detail in [4]. Below, we briefly recall the main characteristics required for further analysis of the data.

ULITKA is an instrument that measures variations in the gradient of the gravitational field. The basic sensitive element of the system is a gravitational detector in the form of a high-Q aluminum cylinder with length $l \approx 1.5$ m and mass $m \approx 10^3$ kg. Rapid variations of the gravitational field lead to perturbations of the main longitudinal mode of this cylinder at the resonance frequency, $f_0 \approx 1.6$ kHz. Acoustical oscillations are transformed into electrical signals by piezoelectric transducers, which are then amplified and subject to optimal processing (see Appendix 1). The threshold sensitivity of the ULITKA antenna to variations in the amplitude of these oscillations in the optimal-filtration band, $\Delta f \approx 1$ Hz, is $\Delta x_{\min} \approx 10^{-14}$ cm/Hz$^{1/2}$. In terms of the variations of the metric $h(t)$ in the field of a weak gravitational wave, this yields $h_{\min} = \Delta x_{\min}/l \approx 10^{-16}$ 1/Hz$^{1/2}$ (which corresponds to a variation of the gravitational gradient at the Earth's surface of $(\partial g/\partial l)_{\min} = (\omega_0^2 \Delta x_{\min}/l) \approx 10$ E over 1 s, where $\omega_0 = 2\pi f_0$ is the resonance frequency of the main mode.

Impulsive stochastic background. When searching for effects due to gravitational waves, attention is drawn to short spikes in the output signal with durations less than one second, which exceed a threshold whose value depends on the selected relationship between the sensitivity and the frequency of events. In early measurements made in 1996 [4], two events per day were detected at the 5σ level, equivalent to an impulsive metric noise of 5×10^{-16}.

In 2001, the effective "pure" measurement time was 60.5% of the year, and the mean occurrence rate of spikes exceeding the 3.5σ threshold was nine every ten minutes. This corresponds to thermal noise statistics but is too high for use in estimating an upper limit for the gravitational-wave background. The amplitude distribution of these spikes, shown in Fig. 1, can be described fairly well with a biexponential curve.

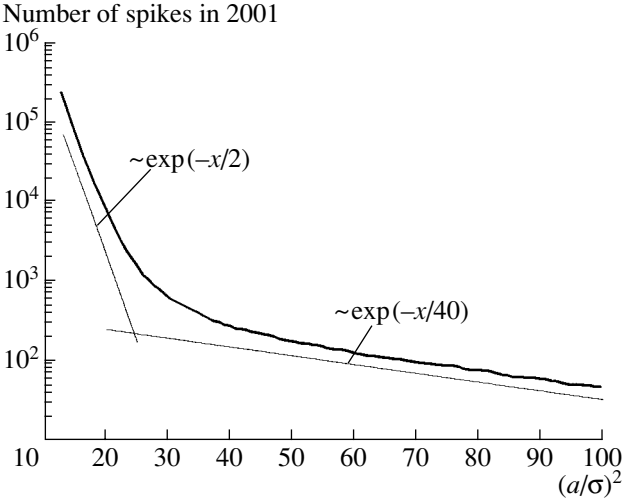

Fig. 1. Distribution of noise-spike amplitudes.

The long, weak, slowly decaying "tail" of the distribution can be explained by the presence of rare impulsive noise. The end of the zone in which the equipment is sensitive to the Brownian noise of the gravitational detector corresponds to a spike amplitude $\geq 5\sigma$.

About 1000 spikes were detected at this threshold over $365 \times 0.605 \approx 221$ days. Applying a selection according to "anticoincidences" with perturbations registered by seismotransducers mounted alongside ULITKA [4] enabled the rejection of 30% of these spikes, leaving a background of three events per day. This is in agreement with the 1996 result to within the measurement errors (to 50%), confirming the estimated upper limit to the "impulsive metric noise" presented in [4]: two to three impulse spikes per day with amplitudes of the order of 5×10^{-16}. Note also that the confirmation of this result testifies to some constancy of the background of local perturbations of ULITKA over the six years of its operation.

Background of slow variations. Searches for slow "solar–terrestrial" correlations require a transition from registered impulsive characteristics to mean values averaged on time scales of tens of minutes or more. Mathematically, the signal $y(t)$ at the output of the linear tract of the antenna (see Fig. 7 below) can be represented as a quasi-Gaussian, random, narrow-band process:

$$y(t) = a_1(t)\cos\omega_0 t - a_2(t)\sin\omega_0 t = r(t)\cos[\omega_0 t + \varphi(t)],$$

where $a_1(t)$ and $a_2(t)$ are quadrature components, and $r(t) = \sqrt{a_1^2(t) + a_2^2(t)}$ and $\varphi(t) = \arctan[a_2(t)/a_1(t)]$ are the envelope function and phase of this oscillation. The auto-frequency-adjustment system makes it possible to trace drifting of the

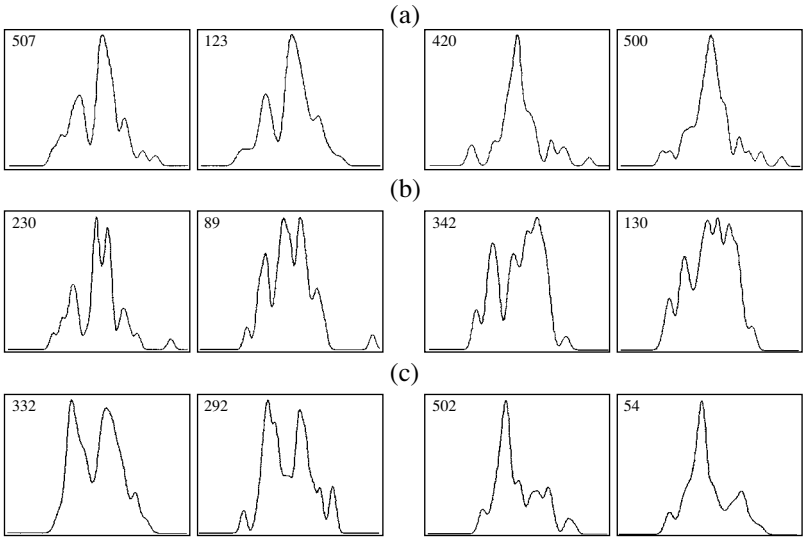

Fig. 2. Examples of pairs of PDEs: (a) selected by experts, with $\rho_{ij} = 0.92$; (b) selected by experts, with $\rho_{ij} = 0.50$; and (c) missed during the expert selection, with $\rho_{ij} = 0.93$.

resonance frequency of the gravitational detector ω_0 with high accuracy (no lower than 1%). The analog signals $a_1(t)$ and $a_2(t)$ are discretized in time with a discretization step of $\delta t \approx 1$ s. The discretized signals $a_{1m} = a_1(m\delta t)$ and $a_{2m} = a_2(m\delta t)$ are saved and used in the subsequent processing of the data.

Slow (technical) variations of the system parameters (the amplification of the electrical circuit, etc.) were taken into account by tracking the behavior of the sample dispersion $D(m)$ of the discretized signals a_{1m} and a_{2m}, calculated using a running average of the square of the envelope function $r(t)$ in intervals $(t, t - \Delta t)$, with $\Delta t = 10$ min:

$$D(m) = D(m\Delta t) = \frac{1}{2\mu} \sum_{i=m-\mu}^{m} r_i^2, \qquad (1)$$

where $r_i^2 = a_{1i}^2 + a_{2i}^2$ and $\mu \approx 600$. The sequence $D(m)$ was saved during the operation of the antenna, and was used by the group of Snoll and by us in our reanalysis, in order to search for anomalous correlations in the output signal $y(t)$.

During the preliminary data reduction, the realization of the random process $D(m)$ with a duration of 120 days was divided into 480 individual intervals $D_i(m)$, $i = \overline{1, 480}$, each with a duration of six hours. The time shift τ_{ij} between intervals was $\tau_{ij} = (1/4)|i - j|$ days. With the time step of $\Delta t = 10$ min, each interval contained 36 discrete readings.

We used the samples $\mathbf{D}_i = \{D_{im}\}$ to construct smoothed probability-density estimates (PDEs) $W_i(x)$, applying the potential-function method, well known in mathematical statistics (see Appendix 2). We used Gaussian curves as the approximating functions. The shapes of our PDE graphs and of the histograms of Snoll obtained using running averages coincide virtually perfectly.

We can treat the PDE graphs as a realization of a random process

$$W_i(x) = \langle W_i(x) \rangle + p_i(x),$$

where $\langle \ldots \rangle$ represents statistical averaging and $p_i(x)$ is a random, nonstationary process with zero mean. The dispersion of this random process is inversely proportional to the sample volume, $n = 36$. Applying the central limit theorem for $\Delta t \gg \tau^*$ (where $\tau^* \approx 7$ s is the relaxation time of the gravitational detector), we can consider the sample dispersion $D(m)$ (1) to be a random, asymptotically Gaussian process. In this case, it can be shown (see Appendix 2) that the mean $\langle W_i(x) \rangle$ of the smoothed PDEs $W_i(x)$ is also a Gaussian function, whose parameters can be calculated directly from the experimental data. This result depends only weakly on the specific form of the approximating function $\delta(x, \varepsilon^2)$.

In a Gaussian approximation, the fine structure of the shapes of the individual curves $W_i(x)$ is determined fully by the behavior of the "residual" $p_i(x) = W_i(x) - \langle W_i(x) \rangle$. This centering enables us to remove the "trivial" correlations (resemblances) of individual PDEs that are positive definite functions.

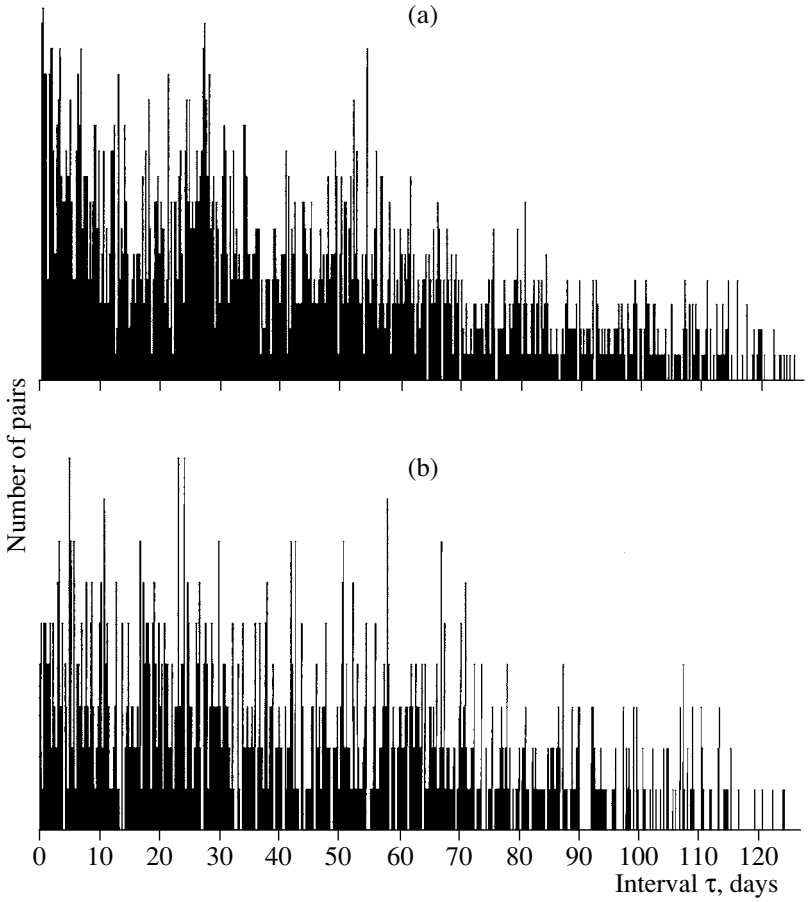

Fig. 3. Number of PDE pairs as a function of the time interval between them for (a) expert selection and (b) selection using the criterion $\rho_{ij} \geq \rho_{\min}$.

3. CORRELATION CRITERION FOR SELECTION

The correlation criterion for selection of a PDE we used in our reanalysis was based on computing the correlation coefficient ρ_{ij} between the functions $p_i(ax)$ and $p_j(x+b)$, $i \neq j$, where a is a compression factor and b is a shift,

$$\rho_{ij} = \max_{a,b} \left| \frac{\sum\limits_x p_i(ax) p_j(x+b)}{\sqrt{E_i(a) E_j}} \right|, \qquad (2)$$

$$E_i(a) = \sum_x p_i^2(ax), \quad E_j = \sum_x p_j^2(x).$$

The introduction of the parameters a and b provides the maximum degree of "fitting" of the shapes of the $p_i(ax)$ and $p_j(x+b)$ curves during the automated selection. Only those pairs of PDEs whose correlation coefficient (2) exceeds a specified threshold $\rho_{\min} = u_{1-\alpha}$ are selected, where $u_\gamma = F_{1\rho}^{-1}(\gamma)$ is the quantile of the sample distribution function $F_{1\rho}(\rho)$ of the ρ_{ij} values and α is the probability of false detection of a correlation. We used all possible pairs of PDEs when constructing the distribution function $F_{1\rho}(\rho)$.

The automated selection yielded a database of such curves based on all possible combinations of $i, j = \overline{1, 480}$. We then used this database to construct the dependence of the event rate $\rho_{ij} \geq \rho_{\min}$ on the time shift (see above) $\tau_{ij} = (1/4)|i-j|$ days. Figure 2a presents pairs of PDEs selected manually by experts that had anomalously high correlation coefficients, $\rho_{ij} \approx 0.92$. At the same time, some expert-selected pairs had correlation coefficients that were substantially lower; examples of such pairs with $\rho_{ij} \approx 0.5$ are shown in Fig. 2b. The mean correlation coefficient for the expert-selected pairs, 0.67, remains fairly high compared to the mean value for all possible pairs, $\langle \rho_{ij}^* \rangle \approx 0.3$. In addition, application of the automated correlation criterion revealed pairs with high correlation coefficients that had been missed by the expert selection, examples of which are shown in Fig. 2c.

Figure 3a presents the dependence of the relative rate of appearance of similarly shaped histograms on the time shift between them [8]. The appearance of a

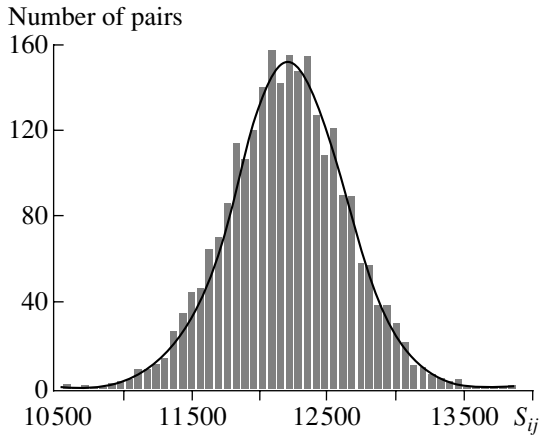

Fig. 4. Histogram of the distribution of the Spearman rank criterion calculated for expert-selected pairs.

characteristic peak near $\tau \approx 27$ days is interpreted in [7, 8] as a consequence of the Snoll effect. Figure 3b presents the same dependence for all pairs that were selected automatically using the correlation criterion. This characteristic period of 27 days disappears.

4. STATISTICAL METHODS FOR SEARCHING FOR ANOMALOUS CORRELATIONS

The selection of PDEs with similar shapes is essentially a specialized method for analyzing the distinctive properties of the random process $D(n)$, whose stability and power require further study, to say the least. Other well-developed probability criteria designed to test for the existence of anomalous statistical relationships in noise are known in mathematical statistics. The application of these criteria to a statistical analysis of the output signal of the ULITKA gravitational antenna enables us to avoid the construction of PDEs, and the results obtained provide additional information about the statistical properties of the input samples $\mathbf{D}_i$ and $\mathbf{D}_j$.

In the first stage of our reanalysis, we investigated the statistical dependences of the samples $\mathbf{D}_i$ and $\mathbf{D}_j$, which we used to construct expert-selected histograms with similar shapes. Let H_1 be the hypothesis that there is a statistical dependence between the samples $\mathbf{D}_i$ and $\mathbf{D}_j$ ($i \neq j$). The alternative hypothesis H_0 is that there is no such dependence. Under hypothesis H_0, the random functions $p_i(x)$ and $p_j(x)$ are statistically independent, so that the coincidence of some fragments of the fine structure of these functions should be considered random events.

One widely used criterion for testing the statistical dependences of samples is the Spearman rank correlation criterion [11]. One advantage of this criterion is that it can be used to study statistical dependences based on properties that cannot be conveniently described quantitatively.

When verifying the rank correlation, we use the samples $\mathbf{R}_i = (R_{i1}, R_{i2}, \ldots, R_{in})$ and $\mathbf{R}_j = (R_{ij}, R_{j2}, \ldots, R_{jn})$ in place of the input samples $\mathbf{D}_i$ and $\mathbf{D}_j$, where R_{ik} and R_{jk} are the ranks of the individual elements of $D_{ik} \in \mathbf{D}_i$ and $D_{jk} \in \mathbf{D}_j$ (the rank of a sample element is the ordinal number of this element in a variational series), and $n = 36$ is the sample volume. In this case, under hypothesis H_0, the rank statistic

$$S_{ij}(n) = \sum_{l=1}^{n} R_{il} R_{jl} \tag{3}$$

should be an asymptotically random Gaussian quantity, whose mean $\langle S_{ij}(n) \rangle$ and dispersion $\sigma_s^2(n)$ are determined by the formulas [11]

$$\langle S_{ij}(n)|H_0 \rangle = \frac{n(n+1)^2}{4}, \tag{4}$$

$$\sigma_s^2(n|H_0) = \frac{n^2(n+1)^2(n-1)}{144}.$$

As part of the reanalysis, we constructed the sample probability density for the random quantities (3) for all pairs of the samples $\mathbf{D}_i$ and $\mathbf{D}_j$ selected by experts during the identification of similar PDEs (Fig. 4). We can see from Fig. 4 that the sample probability density is in good agreement with the hypothetical Gaussian with the parameters (4) (solid curve). We tested the hypothesis that the statistic (3) had a Gaussian distribution with the parameters (4) using the criterion of Pearson [11, 12]. The result was the rejection of the hypothesis H_1 with probability $P \geq 1 - \alpha \approx 0.95$ (α is the probability of false detection of a correlation). Thus, the expert-selected samples $\mathbf{D}_i$ and $\mathbf{D}_j$ are statistically independent with high probability (in the sense of the criterion of the Spearman rank correlation). It follows that the "similarity" of the smoothed PDEs cannot be considered a trustworthy indication of the presence of some common external perturbation for ULITKA noise samples equally spaced in time.

A universal, nonparametric criterion for testing the statistical dependence of the samples $\mathbf{D}_i$ and $\mathbf{D}_j$ ($i \neq j$) is based on verifying the factorization of the two-dimensional (joint) distribution function $F_2(x_i, x_j)$ of the random processes $D_i(m)$ and $D_j(m)$. Let

$$F_2(x_i, x_j) - F_1(x_i)F_1(x_j) = \Delta(x_i, x_j|H_{0,1}),$$

where $F_1(x_j)$ are the one-dimensional distribution functions. We then have under the hypotheses H_0 and $H_1 \Delta(x_i, x_j|H_0) = 0$ and $\Delta(x_i, x_j|H_1) \neq 0$. Unfortunately, with the small volume $n = 36$ of the samples

$\mathbf{D}_i$ and $\mathbf{D}_j$, the resulting joint sample distribution function is too crude an estimate of the distribution function $F_2(x_i, x_j)$ to perform this test.

To overcome this problem, we did not form individual subintervals $D_i(m)$, instead investigating the statistical dependence of the random processes $X(m) = D(m)$ and $Y(m) = D(m+k)$, where $k = [[\tau/\Delta t]]$ and τ is an arbitrary time shift. The existence of anomalous correlations with a period of 27 days (hypothesis H_1) should lead to a statistical dependence between the random processes $X(m)$ and $Y(m)$ for some characteristic shift.

Let $(X_1, Y_1; X_2, Y_2; \ldots; X_M, Y_M)$ be a two-dimensional sample obtained by realizing the random processes $X(m)$ and $Y(m)$: $X_k = X(k)$, $Y_k = Y(k)$. These M sample pairs are distributed in x intervals of class r and y intervals of class s forming a "table of conjugate criteria" [11–13]. Then, assuming that m_{ij} is the number of pairs (X_k, Y_k) falling in the class i x interval and in the class j y interval, we have

$$f^2(r,s) = \sum_{i=1}^{r}\sum_{j=1}^{s} \frac{\left(\frac{m_{ij}}{M} - \frac{m_{ii}}{M}\frac{m_{jj}}{M}\right)^2}{\frac{m_{ii}}{M}\frac{m_{jj}}{M}} \qquad (5)$$

$$= \sum_{i=1}^{r}\sum_{j=1}^{s} \frac{m_{ij}^2}{m_{ii}m_{jj}} - 1 \le \min(r,s) - 1,$$

$f^2(r,s)$ is the root-mean-square conjugacy of the criteria (residual).

Under H_0 with $M \to \infty$ (in reality with $M \gg 1$), the probability statistics of Mf^2 converge to χ^2 statistics with $L = (r-1)(s-1)$ degrees of freedom. Normalization of the χ^2 distribution (with $m_{ij} > 10$) leads to the following critical rule: the hypothesis H_1 (the random processes $X(m)$ and $Y(m)$ are statistically dependent) should be adopted if

$$Mf^2 > \chi^2_{1-\alpha}(L),$$

$$\chi^2_{1-\alpha}(L) \approx \frac{1}{2}(\sqrt{2L-1} + u_{1-\alpha})^2,$$

where $L \gg 1$, u_P is the quantile of the Gaussian distribution, and α is the probability of false detection of a correlation. Otherwise, the alternative hypothesis H_0 should be adopted.

Figure 5 presents the dependence $f^2(r,s,\tau)$ as a function of the shift $\tau = m'\Delta t$ constructed for a realization of the random process $D(n)$ (for $r = s = 10$, $M = 10\,000$, and $0 \le \tau \le 60$ days). For the case of $L = 81$ degrees of freedom and $\alpha = 0.05$, the curve $f^2(r,s,\tau)$ lies completely below the threshold level $\chi^2_{0.95}(81) \approx 107.3$. Consequently, we can consider the analog (continuous) random processes $D(t)$ and $D(t+\tau)$ to be statistically independent with the fairly high confidence level $P = (1-\alpha) = 0.95$. This conclusion enables us to reject the hypothesis that there exist anomalous periodic perturbations in the output signal of ULITKA.

5. SPIKE CORRELATION ANALYSIS

Geophysical studies of the intensity of seismic interference during periods of strong earthquakes often apply statistical analyses of the rate of spikes in the output signal of a high-frequency seismometer [14] (by a spike, we mean an event in which the real noise crosses some threshold level C.) The statistics of such spikes for the case of a high threshold are closely related to the behavior of the tails of probability-density distributions. During the expert selection of the smoothed histograms according to their shapes, the behavior of the distribution tails was not taken into account. Therefore, we can consider tracing spikes associated with the random process $D(m)$ to be an additional test for the presence of quasi-periodic "impulsive" events at the antenna. External quasi-periodic perturbations of a low-frequency gradient of the gravitational field should have led to periodic variations in the rate of appearance of spikes.

Let $\Delta N(m, C)$ be the number of spikes of the process being analyzed in the interval $(m-\mu, m)$ (for analog processing in the interval $(t-\Delta t, t)$). Figure 6 presents the sample estimate of the autocorrelation function of a random impulsive process $\eta(m) = \Delta N(m, C)$ for a high threshold $C = 4\sigma_D$, where σ_D^2 is the sample dispersion of the random process $D(m)$. No characteristic "flares" of the autocorrelation function are observed (for a periodic signal with a period of $\tau = \tau_0 \approx 27$ days). When testing the reliability of this result, the confidence interval is calculated using the Moire–Laplace asymptotic. In a "Gaussian" approximation, the confidence coefficient is $\gamma \approx 0.96$.

6. DISCUSSION OF MAIN RESULTS

Summarizing the results of the tests presented above, we are able to draw the following conclusions.

We have estimated the metric noise during searches for impulsive perturbations of the high-frequency background of the gravitational gradient to be 5×10^{-16}, in agreement with the earlier results of [4]. This testifies to the stability of impulsive interference in the kilohertz range, as well as to the operational stability of the ULITKA gravitational antenna in its quasi-continuous monitoring regime. In connection with the detection of anomalous coincidences of gravitational events reported in [6], it will be of interest to test the ULITKA noise background for coincidences with the signals of the Explorer and Nautilus antennas.

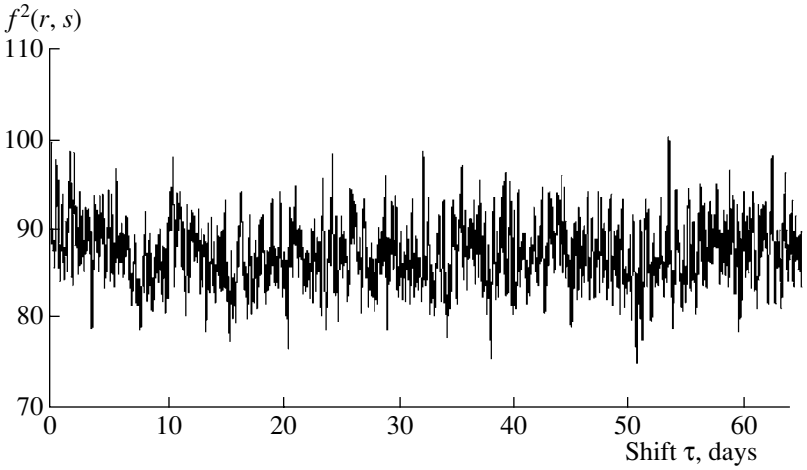

Fig. 5. Root-mean-square conjugacy for various time shifts; $r = s = 10$.

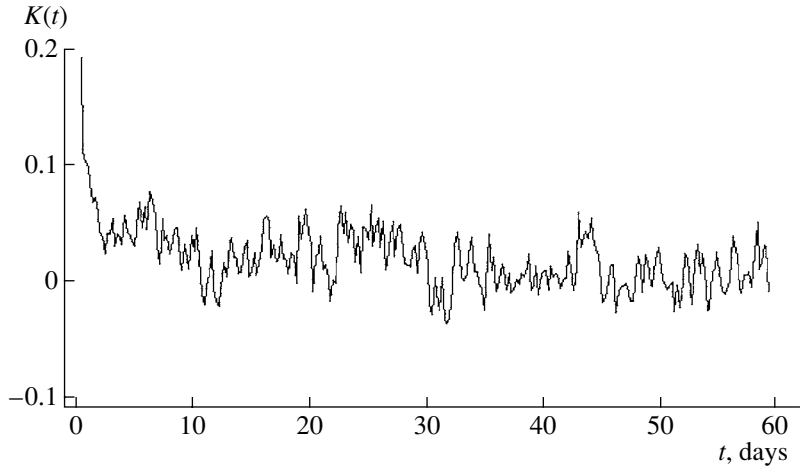

Fig. 6. Correlation function of the number of spikes.

Our attempts to find hidden periodicities in the output signal of the ULITKA gravitational antenna were not successful. In particular, "anomalous" effects with a period close to the rotational period of the outer envelope of the Sun (27 days) were not detected in the antenna noise. The probability that this lack of detection is erroneous does not exceed 0.05.

In contrast to the subjective method of expert selection, we have applied an automated algorithm for selecting smoothed PDEs with similar shapes. This procedure incorporated the obvious *a priori* information that the analyzed probability-density estimate $W_i(x)$ is constructed from a realization of the quasi-Gaussian process $D(m)$. By centering these functions, we were able to exclude the trivial part of the correlations that are positive definite PDEs and to work with the random component $p_i(x)$. The presence of such a component is due to the finite volume of the sample, $n = 36$. Comparison and conformal fitting of the PDEs and calculation of the correlation coefficient ρ_{ij} (2) simulated the process of expert selection.

The automated selection gave a negative result: the relative repeatability of PDEs with similar shapes does not have a significant peak at a time shift of $\tau \approx 27$ days.

We have paid special attention to verifying the statistical dependence of the samples $\mathbf{D}_i$ and $\mathbf{D}_j$ selected in expert searches (i.e., which gave rise to similar PDEs). A test of this dependence using the nonparametric Spearman criterion demonstrated that there is no rank correlation between the elements of these samples. Note that, in tests for the existence of anomalous correlations of samples that are uniform in time, applying rank criteria is more effective than comparing the PDEs $W_i(x)$ and $W_j(x)$ constructed from variational series, since information about the

mutual locations of individual elements in the samples $\mathbf{D}_i$ and $\mathbf{D}_j$ is lost during the construction of such series.

In addition, to search for hidden periodicity in the ULITKA noise, we investigated the statistical relationship between the input process $X(t) = D(t)$ and the auxiliary process $Y(t) = D(t + \tau)$. In this case, we adopted a "narrow" meaning for the statistical independence of these random processes: the joint distribution function $F_2(X, Y)$ was factorized under the null hypothesis H_0. We verified the correctness of this factorization during the reduction of the real data using a standard method based on the application of a table of "conjugate criteria." The alternative hypothesis H_1 (the random processes $X(t)$ and $Y(t)$ are statistically dependent for the shift $\tau \approx 27$ days) can be rejected with a probability exceeding 0.95.

In our opinion, applying probability criteria for the analysis of individual samples is preferable, since the "fine structure" in the samples is more fully taken into account in this approach, and the need to smooth the PDEs constructed from these samples is reduced.

Returning to the question of a hypothetical gravitational action on the ULITKA antenna, we note that it is not possible to identify the origin of such an action, even at low frequencies. For example, the daily variations of the gravitational gradient at the ULITKA sensitivity threshold (10 E) correspond to inadmissibly large variations in the density of the atmosphere, exceeding the density of its lower layers by three to four orders of magnitude. In principle, we could attempt to relate the appearance of anomalous correlations in the output signal of the antenna with possible non-linear parametric effects due to ionospheric perturbations on the electric circuit of the recording system. However, since the formation of the auxiliary process $D(n)$ (1) used in our reanalysis makes it possible to trace slow variations in the gain coefficient, this mechanism should be considered improbable.

7. ACKNOWLEDGMENTS

The authors thank S.L. Snoll and A.A. Konradov for useful discussions and for presenting certain material, and also A.M. Cherepashchuk for clarification of a number of astrophysical questions and for his continued interest in this work.

APPENDIX 1

Data Collection System for the ULITKA Gravitational Antenna

Figure 7 shows a flowchart of the detector system of the ULITKA gravitational antenna. The electrical

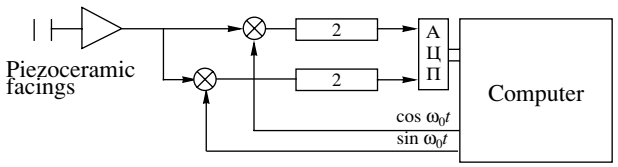

Fig. 7. Data-collection system.

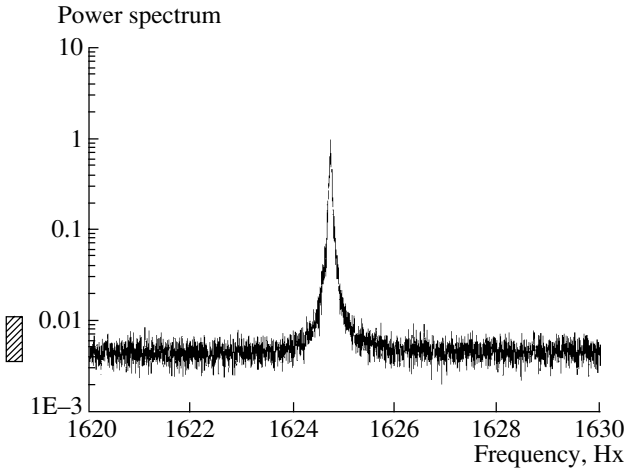

Fig. 8. Noise spectral density at the output of ULITKA.

narrow-band signal $x(t)$ from the piezo-ceramic facings is routed to the input of a synchronous detector (filtration bandwidth 1 Hz), which distinguishes the quadrature components $a_1(t)$ and $a_2(t)$. The analog (continuous) signals $a_1(t)$ and $a_2(t)$ are routed to the input of an analog-to-digital converter (ADC). The discretization frequency is ten readings per second. The following tasks are carried out during the subsequent digital processing of the data:

(1) The complex envelope $c(t) = a_1(t) + ja_2(t)$ is formed; the reference frequency of the synchronous detector is synthesized.

(2) A running average is used to calculate the dispersions of the quadrature components $a_1(t)$ and $a_2(t)$ in ten-minute intervals; the resulting data are stored on disk.

(3) The normalized quadrature components are processed using an optimum scheme for Gaussian noise (the quadratures are passed through a difference chain, after which the sum of their squares is calculated). Information about the characteristics of spikes exceeding the 3.5σ detection threshold is saved in a database.

(4) The internal clock of the computer is tied to an accurate time signal.

Figure 8 presents the spectral density of the noise at the output of the low-noise amplifier. This spectrum was constructed using a duration of 5 min and

a 2×10^6 accurate fast Fourier transform (with a discretization frequency of about 6 kHz), then averaged over 20 realizations. The narrow resonance peak corresponds to the spectral density of the thermal antenna noise. The pedestal in the probability density function is determined by the intensity of the broadband electrical noise. When the signal-to-noise ratio is ≈100, the effective bandwidth of the Gaussian receiver is 1 Hz.

APPENDIX 2

Method of Potential Functions for Estimating an Unknown Probability Density (the Parzen–Nadaray Method)

Let

$$F_{1i}(x) = \frac{1}{n}\sum_{m=1}^{n} V(x - D_{im}) \qquad \text{(A1)}$$

be the sample distribution function of the random process $D(m)$, constructed using real data in the ith subinterval, and $V_1(x)$ be the unit function: $V(x) = 1$ when $x \geq 0$ and $V(x) = 0$ when $x < 0$.

Formally differentiating both sides of expression (A2), we find the unshifted sample PDE of the random process $D(m)$:

$$W_i(x) = \frac{dF_{1i}(x)}{dx} = \frac{1}{n}\sum_{n=1}^{n} \delta(x - D_{im}), \qquad \text{(A2)}$$

where $\delta(x)$ is the delta function. In the potential-function method, the delta function $\delta(x)$ is replaced by "smoothed" approximating functions $\delta(x, \varepsilon^2)$ that depend on the smoothing parameter ε^2. Gaussian curves can be used as these functions [11–13]:

$$\delta(x, \varepsilon^2) = \frac{1}{\sqrt{2\pi\varepsilon^2}} \exp\left\{-\frac{x^2}{2\varepsilon^2}\right\}, \qquad \text{(A3)}$$
$$-\infty < D < \infty, \quad \delta(x, 0) = \delta(x).$$

Using expressions (A2) and (A3), we can find the smoothed PDE for the Parzen–Nadaray method:

$$W_i(x) = \frac{1}{n}\sum_{m=1}^{n} \delta(x - D_{im}, \varepsilon_i^2). \qquad \text{(A4)}$$

The "smoothing" parameter ε_i^2 in (A4) was chosen in accordance with the condition $\varepsilon_i^2 \ll \hat{\sigma}_i^2$, where $\hat{\sigma}_i^2$ is the sample dispersion of the random process $D(m)$ in the ith interval:

$$\hat{\sigma}_i^2 = \frac{1}{n-1}\sum_{m=1}^{n} (D_{im} - \hat{m}_i)^2, \quad \hat{m}_i = \frac{1}{n}\sum_{m=1}^{n} D_{im}.$$

Let $\langle W_i(D)\rangle$ be the mean value of the random [13] process $W_i(x)$ (A4), and the random process $D(m)$ be asymptotically Gaussian with the parameters (m_i, σ_i^2). We then find using (A3) and (A4)

$$\langle W_i(x)\rangle \approx \frac{1}{\sqrt{2\pi\hat{\sigma}_i^2}} \int_{-\infty}^{\infty} \delta(x - z.\varepsilon_i^2) \qquad \text{(A5)}$$
$$\times \exp\left\{-\frac{(z - \hat{m}_i)^2}{2\hat{\sigma}_i^2}\right\} dz$$
$$= \frac{1}{\sqrt{2\pi(\hat{\sigma}_i^2 + \varepsilon_i^2)}} \exp\left\{-\frac{(x - \hat{m}_i)^2}{2(\hat{\sigma}_i^2 + \varepsilon_i^2)}\right\}.$$

Consequently, for a Gaussian random process $D(m)$ and Gaussian approximating functions $\delta(x, \varepsilon^2)$, the mean value $\langle W_i(x)\rangle$ of the smoothed PDE $W_i(x)$ is also Gaussian. We note especially that, when $\varepsilon_i^2 \ll \sigma_i^2$, the shape of the smoothed PDEs depends only weakly on the specific form of the approximating functions $\delta(D, \varepsilon^2)$.

REFERENCES

1. N. Courtier, B. Duccorne, J. Goodkind, *et al.*, Phys. Earth Planet. Inter. **117**, 3 (2000).
2. P. Astone *et al.*, Astropart. Phys. **7**, 231 (1997).
3. P. Astone, M. Bassan, and P. Bonifazi, Phys. Rev. D **47**, 362 (1993).
4. A. V. Gusev, V. V. Kulagin, S. I. Oreshkin, *et al.*, Astron. Zh. **74**, 287 (1997) [Astron. Rep. **41**, 248 (1997)].
5. V. N. Rudenko, A. V. Gusev, V. K. Kravchuk, and M. P. Vinogradov, Zh. Éksp. Teor. Fiz. **118**, 979 (2000) [JETP **91**, 845 (2000)].
6. P. Astone, D. Babusci, M. Bassan, *et al.*, Class. Quantum Grav. **19**, 5449 (2002).
7. A. V. Bruns and B. M. Vladimirskiĭ, Izv. Krym. Astrofiz. Obs. **92**, 129 (1995).
8. S. E. Snoll, V. A. Kolombet, E. V. Pozharskiĭ, *et al.*, Usp. Fiz. Nauk **168**, 1129 (1998) [Phys. Usp. **41**, 1025 (1998)].
9. S. E. Snoll, T. A. Zenchenko, E. V. Pozarski, *et al.*, *Proc. of 2nd Alexander Gurwitsch Conference "Biophotonics and Coherent Systems"* (Moscow State Univ., Moscow, 2000), p. 43.
10. S. E. Snoll, Itogi Nauki Tekh., Ser.: Obchsh. Probl. Fiz.-Khim. Biol. **5**, 130 (1985).
11. B. R. Levin, *Theoretical Foundations of Statistical Radio Engineering* [in Russian] (Sov. Radio, Moscow, 1976), Vol. 3.
12. E. P. Kulikov, *Measuring the Parameters of Random Processes* [in Russian] (Sov. Radio, Moscow, 1982).
13. M. G. Kendall and A. Stuart, *Theory of Statistics*, Vol. 2: *Inference and Relationship* (Charles Griffin, London, 1961; Nauka, Moscow, 1973).
14. O. B. Khavroshkin, Itogi Nauki Tekh., Ser.: Obchsh. Probl. Geofiz. Seĭsmol. **3**, 93 (1998).

Translated by D. Gabuzda

Astronomy Reports, Vol. 47, No. 8, 2003, pp. 679–684. Translated from Astronomicheskiĭ Zhurnal, Vol. 80, No. 8, 2003, pp. 738–743.

The Lower Temperature Limit of Accretors

M. K. Abubekerov[1] and V. M. Lipunov[1,2]

[1] *Physics Department, Moscow State University, Moscow, 119992 Russia*

[2] *Sternberg Astronomical Institute, Universitetskiĭ pr. 13, Moscow, 119992 Russia*

Received June 20, 2002; in final form, January 10, 2003

Abstract—There should be a universal correlation between the main observational parameters of magnetized accreting stars (neutron stars, white dwarfs, and possibly T Tauri stars): their luminosities, periods, and temperatures. To first approximation, such a dependence is obeyed reasonably well for X-ray pulsars, intermediate polars, and T Tauri stars. In contrast, the parameters of anomalous pulsars (so-called "magnetars") and soft gamma-ray repeaters differ sharply from this dependence, and even occupy a "forbidden" region in the parameter space. This presents a serious argument against the idea that these are accreting neutron stars. © *2003 MAIK "Nauka/Interperiodica".*

1. INTRODUCTION

The theory of accretion onto magnetized stars was developed in connection with the discovery and subsequent study of X-ray pulsars in binary systems [1]. Although we are still far from being able to construct a complete theory, to first approximation, the main elements of the theory discussed as early as the 1970s can still be considered to be on firm ground. The most important of these include the following.

(1) The size of the magnetosphere of the accreting star is close to the so-called Alfven radius:

$$R_A = \left(\frac{\mu^2}{2\dot{M}\sqrt{2GM_x}}\right)^{2/7}.$$

(2) During its evolution under the action of the accelerating and decelerating torques in the system, the accreting star tends to approach an equilibrium state in which the size of the magnetosphere is close to the corotation radius ($\kappa \simeq 1$) [2]:

$$R_A = \kappa R_c = \kappa(GM_x/\omega^2)^{1/3}.$$

(3) The time over which this equilibrium is attained is always less than the characteristic lifetime of the star in the accretion stage:

$$t_{eq} = \frac{I\omega}{\dot{M}\sqrt{GMR_c}} = \frac{M_x}{\dot{M}}\left(\frac{R_x}{R_c}\right)^3 \ll \frac{M_x}{\dot{M}}.$$

Generally, speaking, these last two points suppose that a disk-accretion regime is realized; this is obviously applicable for systems in which there is a flow of material through the inner Lagrange point but is also a quite likely scenario for accretion of material from a stellar wind. Here, we are not considering only systems in which there is disk accretion. Recall that the main observational quantities associated with X-ray pulsars are their luminosity L, period P, period derivative ($\dot{P}$), and characteristic spectral temperature (kT_{spec}). The first three quantities are obviously interconnected, since the luminosity is determined by the accretion rate, which also determines the rate of change of the period. Here, we concentrate on the fact that the three points listed above imply that the luminosity and period of any accreting star (accretor) should be correlated with the characteristic temperature of its radiation.

2. A NEW PICTURE FOR X-RAY PULSARS

Let us consider a lower limit for the characteristic temperature of the radiating region of an accretor. As a first approximation, we can use the Stefan–Boltzmann formula

$$L = S\sigma T^4. \quad (1)$$

We can estimate the size of the region onto which the accreting material falls based on the dipole structure of the magnetic field of the accretor [3]:

$$S = 2\pi R_x^2 \epsilon^2, \quad (2)$$

where ϵ is the opening angle of the polar column, which is determined by the accretor's radius R_x and the size of the Alfven zone R_A via the expression

$$\epsilon = \left(\frac{R_x}{R_A}\right)^{1/2}. \quad (3)$$

Let us now also take into consider the fact that, during its evolution, the accretor tends toward a state

1063-7729/03/4708-0679$24.00

Table 1. Temperatures of accretors

Type	Name	$kT_{\min}$, eV	kT_{spec}, eV	$kT_{\rm eff}$, eV	$f(L)$
Neutron stars	Her X-1	3754	19000	13593	1.398
	4U 0115+63	4965	8000	5631	1.421
	X0331+53	4633	15500	11089	1.398
	Cen X-3	7045	14300	8511	1.680
	Vela X-1	6954	17500	13112	1.335
Magnetars	AXJ 1845−0258	1752	640	541	1.182
	1E 2259+586	1259	410	365	1.121
	1E 1841−045	1911	550	465	1.182
	4U 0142+615	2456	390	314	1.240
	1E 1048−5937	1964	640	530	1.206
	1RXS J17084.9	1986	460	386	1.190
Soft gamma-ray repeaters	SGR 1900+14	696	500	486	1.027
	SGR 1806−20*	76000	9000	5357	1.680
	SGR 1627−41	1107	1300	1181	1.10
Burster	SAXJ 1808.4−36	81	200	223	0.896
Polar	AM Her	3.868	28	16	1.68
Intermediate polars	DQ Her	0.937	20	11.9	1.68
	SW UMa	3.307	70	41.6	1.68
T Tauri star	T Tau	0.290	0.43	0.25	1.68

* The temperature of the X-ray flare of the source is indicated.

in which the Alfven radius approaches the corotation radius R_c, i.e.,

$$R_A = \kappa R_c, \qquad (4)$$

where κ is a dimensionless coefficient that is close to unity. Further, using the definition of the corotation radius and (1)–(4), we obtain the minimum temperature of the accretion zone in the blackbody approximation

$$kT_{\min} = 0.94\frac{M_1^{1/12}L_{35}^{1/4}P^{1/6}}{R_6^{3/4}}\ \text{keV}. \qquad (5)$$

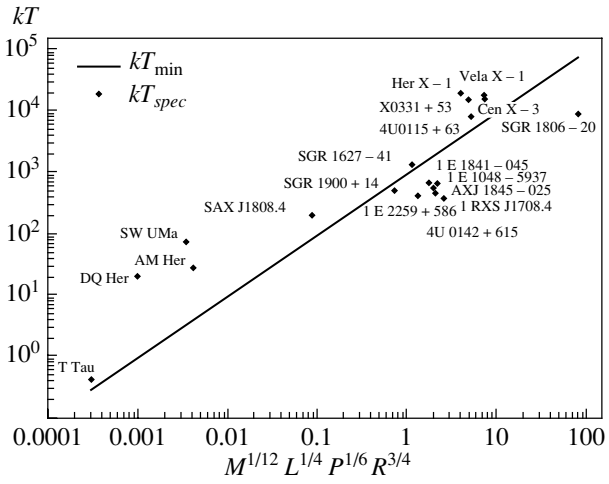

Dependence of the spectral temperature on the parameters of the accretor. kT is measured in eV, M in $M_\odot$, L in 10^{35} erg/s, P in s, and R in 10^6 cm.

In (5), the mass is normalized to one solar mass, the luminosity to 10^{35} erg/s, the period to one second, and the radius to 10^6 cm. The corresponding relation is shown by the line in Fig. 1.

We emphasize again that (5) gives a lower limit for the temperature of the accretor's radiation zone. As a consequence of Rayleigh–Taylor instability, the accreting material channeled in the near-polar zones by the magnetic force lines falls not onto the polar cap of the accretor but instead into a narrow ring of much smaller area [1]. It is obvious that the resulting lower limit for the temperature can be applied to any magnetized accretor independent of its nature—a neutron star, white dwarf, or ordinary star. The main thing is that we are dealing with magnetized objects accreting from a disk. There is no doubt that such objects are found among X-ray pulsars, X-ray bursters, cataclysmic variables (polars and intermediate polars), and possibly T Tauri stars [4].

Table 2. Used numerical values of main accretor characteristics

Type	Name	P, s	L, 10^{35} erg/s	R, 10^6 cm	$M/M_\odot$
Neutron stars	Her X-1	1.24	200	1.0	1.4
	4U 0115+63	3.61	300	1.0	1.4
	X0331+53	4.38	200	1.0	1.4
	Cen X-3	4.84	1000	1.0	1.4
	Vela X-1	283	63	1.0	1.4
Magnetars	AXJ 1845−0258	6.97	3	1.0	1.4
	1E 2259+586	6.98	0.8	1.0	1.4
	1E 1841−045	11.76	3	1.0	1.4
	4U 0142+615	8.69	10	1.0	1.4
	1E 1048−5937	6.44	5	1.0	1.4
	1RXS J17084.9	10.99	3.6	1.0	1.4
Soft gamma-ray repeaters	SGR 1900+14	5.16	0.09	1.0	1.4
	SGR 1806−20*	7.47	10^7	1.0	1.4
	SGR 1627−41	6.41	0.5	1.0	1.4
Burster	SAXJ 1808.4−36	0.0025	0.003	1.0	1.4
Polar	AM Her	11139.2	0.0002	700	1.0
Intermediate polars	DQ Her	71.07	0.00002	700	1.0
	SW UMa	954	0.0005	700	1.0
T Tauri star	T Tau	432000	0.0044	140000	1.0

* The luminosity of the X-ray flare is indicated. The masses and radii of neutron stars are not intended to be extremely accurate, but to represent their most likely values.

3. THE ROLE OF COMPTONIZATION

In the case of accreting neutron stars, we will use the model atmosphere of [5] to specify the relationship between the spectral X-ray temperature of the accretor kT_{spec} (which we will take to be the temperature in the best-fit approximation to the observed spectrum of the form $I \propto \exp^{-h\nu/kT_{spec}}$) and the effective temperature of the radiating region.

We wish to elucidate the effect of comptonization on the spectrum. We write for the relationship between kT_{spec} and $kT_{\rm eff}$

$$T_{spec} = f(L)T_{\rm eff}, \tag{6}$$

where the function $f(L)$ has the form

$$f(L) = \begin{cases} 1.51(L/L_{\rm edd})^{0.04}, & L \ll L_{\rm edd} \\ 1.68, & L \simeq L_{\rm edd}. \end{cases}$$

The results of correcting for the effect of comptonization are presented in Table 1. We can see that, as before, the temperatures of observed accretors

Table 3. References to observational data for the accretors

Type	Name	Reference
Neutron stars	Her X-1	[6, 7]
	4U 0115+63	[6, 7]
	X0331+53	[6, 7]
	Cen X-3	[6, 7]
	Vela X-1	[6, 7]
Magnetars	AXJ 1845−0258	[8−10]
	1E 2259+586	[8−10]
	1E 1841−045	[8−10]
	4U 0142+615	[8−10]
	1E 1048−5937	[8−10]
	1RXS J17084.9	[8, 10, 11, 12]
Soft gamma-ray repeaters	SGR 1900+14	[13−16]
	SGR 1806−20	[17−20]
	SGR 1627−41	[21−23]
Burster	SAXJ 1808.4−36	[24, 25]
Polar	AM Her	[6, 26, 27]
Intermediate polars	DQ Her	[6, 28]
	SW UMa	[6, 29]
T Tauri star	T Tau	[4, 6]

are higher than their minimum values. The effect of comptonization is somewhat smaller in the case of other types of accretors—polars and T Tauri stars—but the discrepancy between the effective temperature and the minimum temperature remains large, even when the largest value of $f(L)$ is used for the correction (Table 1).

4. POLAR AND T TAURI SYSTEMS

The cataclysmic variable AM Her is a member of the subclass of polars. It is a binary system containing a magnetized white dwarf and a red dwarf. The red dwarf fills its Roche lobe. The orbital period and rotational period of the white dwarf are nearly coincident, $P_{spin} = 0.77P_{orb}$. It is thought that the magnetic field at the white-dwarf surface is $\sim 10^9$ G [6].

DQ Her is a cataclysmic variable classified as an intermediate polar. It is a binary system containing a white dwarf and a K−M star (the latter star's spectral type has not been established more precisely). The synchronization coefficient is $P_{spin} = 0.004P_{orb}$. The magnetic field at the white-dwarf surface is believed to be $\sim 10^6$ G [6].

SW UMa is another intermediate-polar cataclysmic variable and periodically produces nova-like flares. It is a binary system containing a white dwarf and an M2 or later-type companion. The relationship between the orbital period of the sys-

tem and the rotational period of the white dwarf is $P_{spin} = 0.195 P_{orb}$ [6].

T Tauri stars are young stars whose accretion luminosities lie in the range from $0.02 L_\odot$ to $0.2 L_\odot$; we have adopted the luminosity $0.1 L_\odot$) for our calculations for T Tau. The period of T Tau varies from 3 to 10 days, being on average 5 days. The mass of the white dwarf is $1-1.5 M_\odot$, and the magnetic field at its surface reaches 10^4 G [4].

The numerical values for the characteristics of the accretors we have considered are listed in Table 2. References to this information are given in Table 3.

5. DISCUSSION

Let us consider the dependence for the lower limit of the accretor temperature (5) shown in the figure, which plots the X-ray spectral temperature as a function of the generalized coordinate

$$\frac{M^{1/12} L^{1/4} P^{1/6}}{R^{3/4}}.$$

We chose the generalized coordinate so as to transform (5) into a linear relationship. Recall that the collection of accretor parameters in (5) is the result of combining expressions (1)–(4), so that the right-hand side of (5) and therefore the generalized coordinate plotted in the figure carries information about the accretor's rotational period, its luminosity, and, indirectly, its moment of inertia.

This same plot shows the temperatures kT_{spec} characterizing the observed spectra. Since the theoretical area of the accretion zone is clearly overestimated, and taking into account the effect of comptonization on the emerging radiation, we can be confident that points with kT_{spec} should lie above their theoretical values, or at the very least not be below them. The region below the theoretical line (5) is therefore a "forbidden zone" for sources whose luminosities are associated with accretion.

We can see from the figure that the anomalous X-ray pulsars (magnetars) and soft gamma-ray repeaters lie in the "forbidden zone." Only SGR 1627–41 deviates slightly from this tendency. However, in contrast to the undoubted accretors, for which $kT_{spec} \gg kT_{\min}$, we have $kT_{\min} \simeq kT_{spec}$ for SGR 1627–41. We also emphasize that the position of SGR 1627–41 above the line corresponding to minimum accretor temperatures does not necessarily imply that the luminosity of this source cannot have a non-accretion nature.

The above discussion brings into doubt the accretional nature of the radiation of magnetars and soft gamma-ray repeaters. It is possible that another mechanism is responsible for their X-ray radiation. For example, one possible mechanism is the dissipation of magnetic fields $\sim 10^{14}-10^{15}$ G [30, 31]. Thus, our proposed universal dependence based on the relationships between the characteristic temperature of the radiation zone of an accretor and its main properties—luminosity, period, mass, and radius—can add weighty arguments that the X-ray radiation of an individual object has an accretional (or non-accretional) origin.

6. ACKNOWLEDGMENTS

The authors thank S.A. Lamzin, N.I. Shakura, and S.B. Popov for useful discussions. This work was supported by the Russian Foundation for Basic Research (project code 00-02-17164a), the State Science and Technology Program "Astronomy" (1.4.4.1), and the Science and Technology Program "Astronomy" (1.4.2.3).

REFERENCES

1. V. M. Lipunov, *Astrophysics of Neutron Stars* [in Russian] (Nauka, Moscow, 1987), p. 280.
2. V. M. Lipunov and N. I. Shakura, Pis'ma Astron. Zh. **2**, 343 (1976) [Sov. Astron. Lett. **2**, 133 (1976)].
3. K. Davidson and J. P. Ostriker, Astrophys. J. **179**, 585 (1973).
4. E. Gullbring, L. Hartmann, C. Briceno, and N. Calvet, Astrophys. J. **492**, 323 (1998).
5. S. Miyaji and Y. Tanaka, *Physics of Neutron Stars and Black Holes*, Ed. by Y. Tanaka (Universal Academy Press, Tokyo, 1988), p. 269.
6. A. M. Cherepashchuk, N. A. Katysheva, T. C. Khruzina, and C. Yu. Shugarov, *Highly Evolved Close Binary Stars: Catalog* (Gordon and Breach Sci., Netherlands, 1996), Vol. 1, Part 1.
7. F. Nagase, *ISAS Symp. of Astrophysics,* Ed. by F. Makino and F. Nagase (1992), p. 2.
8. E. V. Gotthelf and G. Vasisht, New Astron. **3**, 293 (1998).
9. R. Perna, J. Heyl, L. Hernquist, A. Juett, and D. Chakrabarty, Astrophys. J. **557**, 18 (2001).
10. D. Marsden, R. Lingenfelter, R. Rotshild, and J. Higdon, Astrophys. J. **550**, 397 (2001).
11. M. Sugizaki, Publ. Astron. Soc. Jpn. **49L**, 25 (1997).
12. G. Israel, T. Oosterbroek, L. Stella, *et al.*, Astrophys. J. Lett. **560**, L65 (2001).
13. K. Hurley, P. Li, C. Kouveliotou, *et al.*, Astrophys. J. Lett. **510**, L111 (1999).
14. C. Kouveliotou, A. Tennant, P. Woods, *et al.*, Astrophys. J. Lett. **558**, L47 (2001).
15. E. Gogus, C. Kouveliotou, P. Woods, *et al.*, Astrophys. J. **577**, 929 (2002).
16. P. Woods, C. Kouveliotou, E. Gogus, *et al.*, Astrophys. J. **552**, 748 (2001).
17. C. Kouveliotou, M. Weisskopf, P. Woods, and R. Fender, Nature **393**, 235 (1998).

18. S. Corbel, P. Wallyn, T. Dame, *et al.*, Astrophys. J. **478**, 624 (1997).
19. D. Kaplan, D. Fox, S. Kulkarni, *et al.*, Astrophys. J. **564**, 935 (2002).
20. E. Fenimore, J. Laros, and A. Ulmer, Astrophys. J. **432**, 742 (1994).
21. P. Woods, C. Kouveliotar, J. van Paradus, *et al.*, Astrophys. J. **519**, 139 (1999).
22. S. Corbel, C. Chapius, T. Dame, and P. Durouchoux, Astrophys. J. Lett. **526**, L29 (1999).
23. K. Hurley, T. Strohmayer, P. Li, *et al.*, Astrophys. J. Lett. **528**, L21 (2000).
24. L. Stella, S. Campana, S. Mereghetti, *et al.*, astro-ph/0005429 (2000).
25. J. J. M. in't Zand, J. Heise, J. M. Muller, *et al.*, Astron. Astrophys. **331**, L25 (1998).
26. D. T. Wickramasinghe, J. Bailey, S. M. Meggit, *et al.*, Mon. Not. R. Astron. Soc. **251**, 28 (1991).
27. I. R. Tuohy, F. K. Lamb, G. P. Garmire, and K. O. Mason, *X-ray Astronomy Advance in Space Exploration,* Ed. by W. A. Baity and L. E. Peterson (Pergamon Press, 1979), p. 197.
28. J. Paterson, Publ. Astron. Soc. Pac. **106**, 209 (1994).
29. A. W. Shafter, P. Szkody, and J. R. Thorstensen, Astrophys. J. **308**, 765 (1986).
30. R. C. Duncan and C. Thompson, Astrophys. J. Lett. **392**, L9 (1992).
31. R. C. Duncan and C. Thompson, Mon. Not. R. Astron. Soc. **275**, 255 (1995).

Translated by D. Gabuzda

Astronomy Reports, Vol. 47, No. 8, 2003, pp. 685–693. Translated from Astronomicheskiĭ Zhurnal, Vol. 80, No. 8, 2003, pp. 744–752.

Equation of State for the Internal Structure of Solar-Type Stars

V. A. Baturin[1] and W. Däppen[2]

[1] *Sternberg Astronomical Institute, Universitetskiĭ pr. 13, Moscow, 119992 Russia*

[2] *University of Southern California, Los Angeles, USA*

Received February 15, 2003; in final form, March 14, 2003

Abstract—The physical basis for thermodynamical modeling of plasma under the conditions typical of moderate-mass stars is considered. We apply the method of thermodynamic potentials to introduce chemical and physical plasma models that represent basic, modern descriptions of a nondegenerate, weakly nonideal plasma. Ionization of an ideal multicomponent plasma at low temperatures is used as a basic approximation for the solar convection zone and in the corresponding chemical picture. The effects of Coulomb free–free and bound–free electron interactions are classified according to their appearance in the solar interior. Modeling internal stellar structure requires a formalism with nonideal ionization at high densities (frequently called pressure ionization). Perspectives for describing such ionization are considered in the framework of several models. © *2003 MAIK "Nauka/Interperiodica"*.

1. INTRODUCTION

The theoretical description of the thermodynamics of matter in stellar interiors is a fundamental problem of astrophysics and the theory of stellar structure. While "extreme" conditions and processes often attract the most attention, the material making up the majority of stars can be considered to be a weakly degenerate, low-temperature plasma. The term "low-temperature" may sound paradoxical, but, from the standpoint of plasma physics, this is the case [1]. In the present paper, we consider the thermodynamic conditions in the interiors of the Sun and solar-mass stars.

The Sun as a star plays a unique role in the theory of stellar structure. Evolutionary calibrations based on the Sun's well-known radius, luminosity, mass, and age enable us to determine the two most important parameters of stellar structure—the convective efficiency and the initial helium abundance in the model. It is difficult to determine these parameters using other methods.

Solar-mass stars have similar temperature and density profiles in their interiors. The outer parts of these stars form a convective zone, i.e., a region that is unstable to mixing. The extent of the convective zone is quite substantial, though it decreases rapidly with the mass of the star: for $M = 1.4\,M_\odot$, its depth is only 10% (while it is 29% in the Sun). Convection in the outer parts is initiated by the ionization of matter and the increase of its opacity. However, ionization does not explain the considerable depth of the convective zone. The bulk of the convective zone can be described by an adiabat (the temperature profile is close to $T \sim \rho^{2/3}$) and is characterized by a relatively rapid increase of the temperature. The temperature grows by a factor of 450 in the solar convective zone, but by only a factor of six in the central radiative zone. In the radiative zone, outside the stellar core, the temperature profile can be approximated by the law $T \sim \rho^{2/7}$. The core boundary can be defined as the region for which the temperature is half the temperature at the center of the star. It is convenient to describe the essentially adiabatic convective zone in terms of the specific entropy of the matter s. The derivative ds/dr is negative in the convective zone, but its absolute value drops very rapidly with increasing density, and any deviation from adiabaticity levels off over a distance of several pressure scale heights. This property suggested [2] that the entropy of the convective zone is a parameter of the stellar structure rather than of convection theory. On the other hand, this parameter (as well as the depth of the convective zone) is determined by the thermodynamic conditions in the radiative zone [3]. Bearing in mind that the temperature and density profiles remain nearly constant during the course of a star's evolution, this implies that, for any fixed temperature, the density (entropy) will decrease (rise) with the mass of the star (Fig. 1).

Interest in the equation of state (EOS) has increased in recent decades due to progress in helioseismology. First, the requirements for the accuracy of solar models have increased, especially for the outer layers. Second, one must know additional parameters, such as the adiabatic exponent, for helioseismic analyses. As a result, it was shown that problems associated with the disagreement between the observed

1063-7729/03/4708-0685$24.00

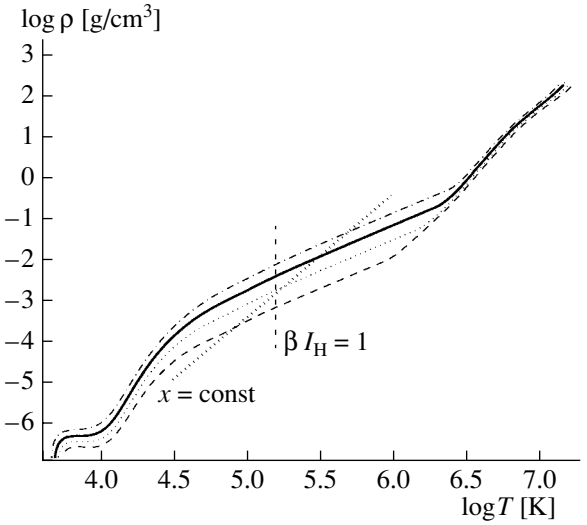

Fig. 1. Profiles of the temperature and density in solar-mass stars. Profiles are shown for stars with four different masses: $0.9M_S$ (dash–dot curve), $1M_S$ (solid curve), $1.1M_S$ (dotted curve), and $1.2M_S$ (dashed curve). The vertical dashed line shows the level $\beta I_{\rm H} = 1$. The dotted line intersecting the profiles corresponds to a constant nonideality of the material.

and theoretical oscillation spectra originate precisely due to the inaccuracy of thermodynamic models (see, e.g., [4]).

Currently, two systems of EOS tables are used most often. The first are the EOS tables of Mihalas, Hummer, and Däppen [5] (abbreviated MHD), which are based on a chemical model for the plasma and are distinguished by their high internal consistency. The only example of an EOS based on the physical picture is the OPAL EOS, which are currently available only as tables [6]. In the present paper, we also use the EOS of Baturin; an example of applying this EOS in a helioseismic analysis can be found in [7].

Comparing the MHD and OPAL EOS's, we can assert that neither is unambiguously preferable. While the problem of helioseismic calibration of the EOS's remains open, some results indicate that the OPAL EOS is more accurate for deep layers of the convective zone [8], whereas the MHD EOS may be better for modeling zones of ionization [9].

2. PHYSICAL AND CHEMICAL PLASMA MODEL

Usually, the EOS refers only to the thermal EOS relating the density, pressure, and temperature: $P = P(T, \rho, X_i)$. However, for computations of the structure of the convective zone and for helioseismic analyses, we must know several additional quantities that cannot be derived using the thermal EOS alone. These are the specific heat $c_P = T(\partial S/\partial T)_P$ and the adiabatic derivatives: the adiabatic temperature gradient $\nabla_S = (\partial \ln T/\partial \ln P)_S$ and adiabatic exponent $\Gamma_1 = (\partial \ln P/\partial \ln \rho)_S$. Not all of these quantities are independent, and they must obey relations that are a consequence of the first and second laws of thermodynamics. This is especially important for numerical EOS's (for instance, the OPAL EOS), for which the accuracy of the control relations is essentially the accuracy of the thermodynamic functions.

To this end, at the basis of modern EOS's lies the method of thermodynamic potentials, i.e., the use of functions whose derivatives give all the thermodynamic quantities and guarantee thermodynamic consistency. The best known potential is the free energy $F(T, \rho, N_i)$. The first-order thermodynamic quantities are computed as first partial derivatives of F:

$$P = -\left(\frac{\partial F}{\partial V}\right)_{T,N_i}, \quad U = -T^2\left(\frac{\partial (F/T)}{\partial T}\right)_{V,N_i},$$
$$S = -\left(\frac{\partial F}{\partial T}\right)_{V,N_i}, \quad \mu_i = \left(\frac{\partial F}{\partial N_i}\right)_{T,\rho,N_{j,j\neq i}}.$$

The choice of potential is not unique. For instance, the internal energy is a potential in the form of the function $U(S, V)$ (there is an incomplete EOS in the form $U(P, V)$, which is sufficient for solving a number of problems [1]). Use of the free energy is popular due to the fact that its variables are "natural" measurable quantities. One key issue is the choice of the number of particles as an argument of the free energy. This is the basis for a chemical picture of the plasma. In such a model, it is easy to describe the noninteracting particles using some assumed statistics, i.e., using an ideal EOS. It is also possible to describe reactions of particles of one sort into particles of another sort, i.e., ideal ionization (for nonideal ionization, see Section 4).

The free energy is related to the concept of a canonical ensemble. Such an ensemble is formed by systems with a given volume V, temperature T, and number of particles N. The temperature of the systems is constant, while the energy can fluctuate. The occupation probability is given by

$$w(\mathbf{K}; V, \beta, N) = \exp \beta[F - E(\mathbf{K})],$$

where $\mathbf{K}$ denotes a system from the ensemble and $\beta \equiv (kT)^{-1}$. The condition for normalization of this probability defines the free energy:

$$-\beta F = \ln \sum_{\mathbf{K}} \exp[-\beta E] = \ln \Sigma.$$

In the case of an ideal gas, the statistical sum Σ is determined by the number of degrees of freedom in the configuration space and, if the particles do not interact, the configuration space is equal to the product

of the phase spaces of the separate particles. Finally, the free energy reduces to an additive expression for each kind of particle; specifically, for electrons, ions, and radiation:

$$F = F_{\rm e} + F_{\rm i} + F_{\rm rad}.$$

The corresponding expressions for the pressure and internal energy are also additive. The free energy remains additive in the case of weak nonideality.

We should note here the role of the chemical potential μ, which is seldom discussed in astrophysical applications. It plays a substantial role in computations of the derivative of the internal energy if the number of particles is variable. This problem remains still poorly understood in astrophysical applications in the case of nonstationary (irreversible) evolutionary processes; for instance, in the presence of diffusion or nuclear reactions. The best known application is associated with the ionization-equilibrium equations.

The chemical potential is a conjugate variable to the number of particles and is associated with the *grand canonical ensemble*. This ensemble is formed by systems with a given volume V and by the quantities β and $-\beta\mu$. The temperature and chemical potential are taken to be constant, while the number of particles of any sort (as well as the energy) can vary.

We obtain for the grand potential, from the condition for normalization of the probability

$$\beta PV = \ln \sum_N \sum_{\mathbf{K}} \exp \beta[N\mu - E(\mathbf{K})]$$
$$= \ln \Sigma(V, \beta, -\beta\mu).$$

The grand potential is a function of the system in terms of V, T, and μ, and the remaining thermodynamic functions are determined as

$$S = -\left(\frac{\partial \Pi}{\partial T}\right)_{V,\mu}, \quad p = -\left(\frac{\partial \Pi}{\partial V}\right)_{T,\mu},$$
$$N_i = -\left(\frac{\partial \Pi}{\partial \mu_i}\right)_{V,T}.$$

This approach is employed in a physical picture for the plasma. Applying an expression for the activity $z_a = e^{\beta\mu_a}/\Lambda_a^3$, we obtain an expression for the particle density:

$$n_a = z_a \left(\frac{\partial \beta p}{\partial z_a}\right).$$

The thermodynamic formalism of the grand potential shows why an expansion of the pressure in degrees of the activity is sufficient for a complete description of the system.

Let us underline certain properties of the chemical picture. Components for every sort of particle enter every term of the potential additively, and, in the ideal case, every term is independent of the densities of the other components. The equilibrium state in terms of the number of particles is found by minimizing the free energy. The chemical picture has a logical basis only for the case of constant internal statistical sums. Variable statistical sums are self-contradictory, since there are no terms corresponding to forces providing this variability.

3. IONIZATION OF THE MATERIAL

Matter is ionized in three possible limits [1]. Two correspond to ideal ionization: high temperature at fixed density and low density at fixed temperature.

There is a third limit: ionization when the density increases while the temperature remains constant. This is commonly named "pressure ionization," although it would probably be more correct to call it density ionization. This limit is fundamentally nonideal, since it corresponds to the action on (disruption of) bound quantum states by the surrounding particles (see Section 4 for more detail).

The ionization of material in stars occurs along adiabats in the convective zone. Along an adiabat, the electron-degeneracy parameter $\eta_e = \ln(n_e\Lambda_e^3/2)$ varies only with the density, i.e., with the degree of ionization. The equation of ionization equilibrium (Saha equation) has the form $\mu_a - \mu_{a^+} = \mu_e = kT\eta_e$. Considering the ratios of the densities of nuclei with a given degree of ionization, we obtain an equation for the point where half of the matter is ionized $(n_{a^+}/n_a = 1)$ in the form $-\ln\left(\Sigma_{\rm int}^a/\Sigma_{\rm int}^{a^+}\right) = \eta + \beta I$. Thus, since it is natural to consider the statistical sums to be constant in the chemical picture, the position of the zone of ionization in the convective zone is determined by the entropy of the adiabat. Another expression for the same relation is $\mu_e \approx I$. In other words, the lower the degree of degeneracy of the star (the higher its mass), the lower the ionization temperature (i.e., the larger the value of βI). For the Sun, $\beta I_{\rm H} \simeq 10$, but for helium, $\beta I_{\rm He} \simeq 6$ (since helium is ionized against the background of hydrogen ionization).

This parameter also determines the depth in perturbations of thermodynamic quantities that have sharp spikes resembling Dirac δ-functions, such as the adiabatic exponent. The width of the ionization zones varies in the opposite sense.

4. COULOMB INTERACTION OF FREE CHARGES

The main nonideal effects are due to the Coulomb attraction and repulsion of charged particles (electrons and nuclei). To some extent, this interaction

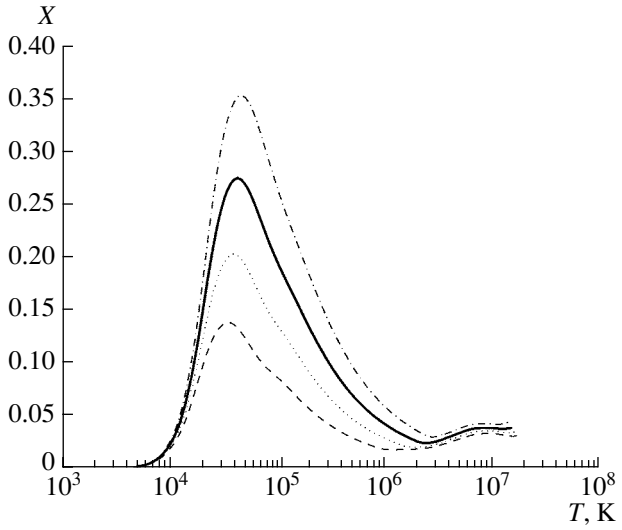

Fig. 2. Coulomb nonideality parameter x in several stellar models. Notation is the same as in Fig. 1.

is already included in the chemical picture, in its description of atoms and partially ionized ions. In the physical picture, all particles are assumed to be structureless; i.e., compound atoms are the result of Coulomb interactions. In this sense, the description in the physical picture is more self-consistent, although much more labor-intensive, especially in the case of a weakly ionized plasma.

It is common to start the description of the Coulomb nonideality with the interaction of free charges, i.e., with a fully ionized plasma. This approach can be traced to the seminal study of Debye and Hückel [10]. The analysis of any nonideality requires matching of the interaction potentials with the thermodynamic parameters. In doing this, we must necessarily go beyond the limits of a simple thermodynamic model. This is obvious in the chemical picture, where it is assumed that the EOS can be based on any stable expression for the free energy. However, for a given potential, we can suggest several methods for the calculation of corrections to the thermodynamic parameters, which, in general, do not lead to the same results [1]. This raises the problem of the statistical consistency of such a model.

The chemical picture is convenient when the degree of nonideality is low and corrections represent additional terms in the sum for the free energy. One example is the short-range interaction potentials for neutrals in rarefied media. However, the Coulomb potential decreases so slowly that it is not even possible to compute the energy of pair interactions. Therefore, in place of the Coulomb potential, an effective screened potential is introduced, which takes into account the electric neutrality of the plasma on certain scales. Without going into the details of deriving expressions for the screened potential in various ways (which can be found in [11]), we present the well-known result:

$$\phi = \frac{\beta e^2}{r}\exp(-r/r_D),$$

where the effective radius r_D, with $r_D^{-2} = 4\pi\beta e^2 \sum n_a Z_a^2$, is called the Debye radius. The screened potential is efficiently limited to the Debye radius. It is important that this potential enables the computation of the potential energy of any charged particle in place of computing a large number of pair-interaction energies. It is convenient to use a dimensionless parameter describing the Coulomb nonideality in the nondegenerate case in the form $x = l/r_D$, where $l = \beta e^2$ is the Bjerum parameter. (In the physical literature, another dimensionless nonideality parameter is often used: $\Gamma = l/d = \beta e^2(4\pi n/3)^{1/3} \sim x^{2/3}$).

In the limit of a linear Debye approximation, the correction to the specific free energy of each charged particle α is

$$f_{es}^0 = \beta F_{es}/(VN_\alpha) = -x/3,$$

while the corrections to the pressure and internal energy have the form

$$\delta p_{es}^0 = \beta P_{es}/n_\alpha = -x/6,$$
$$u_{es}^0 = \beta U_{es}/(VN_\alpha) = -x/2.$$

Let us consider the behavior of corrections in the solar model. Along an adiabat, the nonideality $x \sim (n_\alpha/T^3)^{1/2}$ will decrease in proportion to the square root of the density. In accordance with the approximate law given in Section 2, the nonideality will increase in the radiative zone, but very slowly, approximately as $\rho^{1/14}$ (Fig. 2).

On the other hand, the nonideality is proportional to the number of charged particles, i.e., the maximum nonideality is located just beneath the ionization zone. The maximum value of x in the solar model is 0.27.

In the linear approximation of a fully ionized plasma and small x, these corrections lead to an increase of the adiabatic exponent $\delta^{es}\Gamma_1 \simeq x/36$. This makes it possible to match the accuracy of Γ_1 in model profiles and the accuracy of x in various models of the nonideality (see the end of this Section).

The discovery of the role of the Coulomb nonideality under the conditions of the solar interior was a fundamental contribution of helioseismology to stellar-structure theory. Estimates of the Coulomb interaction had been known for a long time [12], but it

remained unclear whether they had any applications. Their role seemed to be important for the center of the Sun, although in this region $x \leq 0.06$ and reduction of the pressure is only about 1%. The thermodynamics of the outer layers seemed to be not very important, since these layers only weakly influence the structure of the Sun as a whole. However, in the beginning of the 1990s, it was shown that it is absolutely essential to take Debye corrections into account in the EOS if we wish to match theoretical and observed spectra of oscillations [4, 13]. Although this assertion is related to several different problems, we shall discuss the simplest interpretation only.

The spectrum of low-degree solar-oscillation modes ($\ell \leq 4$) having high radial orders ($n \geq 10$) consists of nearly equidistant peaks. The distance between peaks is related to the inverse time for sound to propagate along the solar radius. The main origin of mismatches between theoretical and observed spectra was the lack of corrections for the Coulomb interaction in the models; these corrections reduce the sound speed in the outer layers, where their contribution to the timescale for the propagation of sound waves is most important.

Let us note one more problem related to the Coulomb potential. The integral of the potential (for opposite charges) also diverges at small distances. This is due to quantum effects, since we are dealing with a description of electron statistics close to a nucleus or ion. However, in a rarefied medium, a free electron appears within a small vicinity of an nucleus fairly rarely, and the problem is not so obvious.

The solution was already suggested in [10], by introducing a minimum distance of approach; i.e., the ions were treated like hard spheres. For a fixed ion radius a, it is possible to obtain all necessary corrections, e.g., $u_{es}^{DH} = u_{es}^0(1 + (a/r_D))^{-1}$ and $\delta p_{es}^{DH} = \delta p_{es}^0(3(1 + a/r_D)^{-1} - 2\tau(a/r_D))$. The function $\tau(z) = 3z^{-3}(\ln(1 + z) - z + z^2/2) = 3z^{-3}\int_0^z y^2(1 + y)^{-1}dy$ appears in these expressions. However, the ions in a stellar plasma do not have a natural radius. Therefore, the choice of such a radius represents an attempt to extrapolate the solution beyond the limit of small x. It was suggested in [16] to adopt the Landau length, equal to $2l/3$, for the ion radius, and to retain the expression for the free energy taking into account this substitution; i.e., setting $f_{es}^\tau = f_{es}^0\tau(2x/3)$. This expression remains quite consistent from the standpoint of the chemical picture. (For more details on the introduction of the τ correction, see [17]).

This form of correction is consistent with the Klein theorem, which states that the corrections for a classical gas should be functions of x alone [18]. For small degrees of nonideality, $\tau \to 1$ and $f_{es}^\tau \to f_{es}^0$; i.e., τ is a correction to the linear approximation of Debye and Hückel (the DH correction). However, when x is large, one can argue that this form of correction reduces the nonideality too much. Indeed, $\tau \sim 1/x$, so that $f_{es} \to$ const, and the correction to the pressure is $p_{es}^\tau \to 0$; i.e., the gas tends to become ideal!

The importance of the τ correction is related to its use in the MHD EOS, which is currently the main EOS used for the chemical picture. More accurately, in the MHD EOS, these expressions are given for the more general case of partial degeneracy of the electrons, and the argument of the function τ has a factor related to the average ion charge.

In the solar model with the maximum x, the value of $\tau(0.3) \approx 0.82$; i.e., the DH correction is reduced by nearly 20%. Thus, the τ correction represents a lower limit for the electrostatic correction.

Note that, if the correction to the free energy is expressed as the product $f^0\zeta(z)$, where the argument z is known, it is possible to derive expressions for all the thermodynamic functions starting from the correction to any one of them. Thus, for instance, more accurate forms of the Coulomb-interaction corrections are often given in terms of the corrections to the pressure $p^0\zeta(x)$, since this is more natural in the physical picture (examples are given below). The corresponding corrections to the free energy then have the form $f^0\left(x^{-1}\int\zeta(x_1)dx_1\right)$. Therefore, we do not present all the corresponding expressions.

In attempts to derive more narrow limits for possible errors in the DH correction, it is possible to consider models with other asymptotic behaviors. In a ring approximation for the expansion in the grand canonical ensemble [19], a solution was found that predicts the computed DH correction using the modified parameter $\bar{x}$, which is a solution of the equation

$$\bar{x}^2 = 4\pi(\beta e^2)^3 \sum\nolimits_\alpha \frac{Z_\alpha^2 n_\alpha}{1 + Z_\alpha^2\bar{x}/2}.$$

If we assume that the charges are equal to unity, this equation becomes cubic: $\bar{x}^2(1 + \bar{x}/2) = x^2$. It can be solved analytically, but even without solving the equation, it is clear that the modified parameter is always smaller than the classical one, $\bar{x} \leq x$, and, for high degrees of nonideality, $\bar{x} \sim x^{2/3} + c$. In this approximation, the pressure correction has an upper limit in the form of a fraction of the ideal pressure. Under solar conditions, the minimum of the ratio $\bar{x}/x$ is no lower than 0.93; i.e., the predicted DH correction will be larger than in the case of the τ correction. However, even in this case, the asymptotic behavior of the correction is underestimated. Based on a quasicrystal model, it is usual to assume that the asymptotics must have order $f_{es}^{cr} \sim x^{2/3}$ [1]. In none

of these cases does the problem of a negative total pressure arise, when the correction for the electrostatic interaction is greater than the ideal component.

If we do not attempt to describe the whole region of nonideality and densities that are very high, we can derive estimates for corrections that are valid only for the case of small nonideal effects but nevertheless, encompass the conditions in the solar interior. In a model with a continuous electron background, two terms of the expansion in x were already obtained in [20]:

$$p_{es}^{Abe} = p_{es}^{0}\,(1 + x(C - 2/3 + \ln(3x)/2))\,.$$

Comparing this correction with those indicated above, we see that it predicts an even lower reduction of the correction for the solar interior than does the linear DH term: no more than 0.03. The next two terms of the expansion in x are also known [15], but their contribution does not exceed several tenths of a percent. Note the difference between the asymptotic models discussed above and the expansions in x. The latter are strictly limited to certain regions of application, outside of which they lead to nonphysical results. Furthermore, in a given model (e.g., a classical plasma in a static potential) we must not use too many terms, since such "more accurate approximation" does not make the physics of the model more meaningful unless other physical effects are taken into account.

The model can be made more accurate by taking quantum effects into account. We can consider quantum effects to be a manifestation of the uncertainty principle [14], so that we expect a "repulsion" of charges at small distances. There are also a number of other corrections related to quantum, diffraction, and exchange effects. A rigorous estimation of these effects is still lacking, and there is the danger of of taking into account the same interactions more than once during a simple summation of various corrections. A model that makes it possible to qualitatively take into account corrections due to quantum-mechanical effects is suggested in [15]. The expression for the free energy has the form $f_{es}^{\Lambda} = f_{es}^{0}\tau(\Lambda_e/8r_D)$; i.e., the charges are not brought together closer than the thermal wavelength Λ_e. This correction can easily be estimated qualitatively, if we take into account the substitution of argument τ by $\sqrt{2\pi}x/8\xi$, where the quantum parameter $\xi = \sqrt{2\pi}\beta e^2/\Lambda_e$ depends only on the temperature. As a result, the role of the τ correction will level out at low temperatures, since $\xi \geq 1$. Thus, in the region of the convective zone of interest to us, differences from the linear DH correction will be completely absent. Only when $T > 3 \times 10^6$ K will the coefficient of x become larger than unity, and it attains about two for the solar core. Thus, uncertainty in quantum effects may reduce the Debye correction at the center of the Sun to 10%.

Note that most theoretical results are obtained in models with a single-component plasma, and must be generalized for the case of a multicomponent mixture of charges. As an example, in the numerical modeling of a strongly nonideal plasma [14], the form $(\langle Z^{5/3}\rangle\langle Z^{1/3}\rangle)^{1/2}$ was obtained for the average charge.

Interactions between the charges lead to displacements of the ionization equilibrium. Attraction leads to the formation of quasistates and reduces the electron potential. As a result, ionization becomes easier, sometimes described as a lowering of the ionization potential. Note that this effect has no relationship to the interaction of free and bound electrons described in the next section and cannot be used to describe pressure ionization.

The results of this section can be summarized as follows. The classical, linear Debye-Hückel correction is quite adequate for the conditions of weak nonideality that are typical for solar-mass stars. The possible reduction of this correction appears to be best described by the formula of Abe [20]. The reduced correction is only 0.957 in the region of maximum nonideality. The probable accuracy of this value (in units of x, i.e., accuracy of the correction itself) is several percent. The described correction for the electrostatic interaction is close to the corresponding terms in the OPAL EOS based on a physical picture.

5. INTERACTION OF BOUND AND FREE CHARGES

The next most important manifestation of the Coulomb nonideality is related to the interaction of free and bound electrons. This interaction leads to ionization as the density is increased and is called pressure ionization.

The problems with including this effect in the EOS are not associated with its influence on various thermodynamic quantities. As we show below, the thermodynamic corrections are not large, and the main effect is to prevent the recombination of electrons at high densities that would be predicted by the classical Saha equation. The problems are related to the methodological basis of chemical pictures. In a chemical picture, it is assumed that there exist fixed states of particles (a spectrum) and some probability for their distribution over various states. The inclusion of pressure ionization requires that we reject these assumptions.

Two classes of models are used to describe pressure ionization. We shall attempt to separate them based on their thermodynamic manifestations. On the one hand, we assume that the energy spectrum of

bound states varies. It is simplest to assume that certain states disappear when some density or temperature is achieved (the radius of the state is larger than the average distance between ions, or $\beta E_s < 1$, respectively). In more elaborate models, not only the number of states but also the energy spectrum itself is variable, for instance, as a result of changing the eigensolutions for the Coulomb potential in an external screened potential. In any case, the disappearance of the ground state of an atom leads to full ionization of the material, called the Mott transition [15]. It is thought that this transition occurs in hydrogen plasma at densities of 0.5–1.0 g/cm^3.

It is clear that the disappearance of states is the result of quantum-mechanical modeling, and cannot be the result of lowering the ionization potential. Since both the temperature and density grow monotonically with depth, the desired full ionization will be achieved in any model with a limited number of states.

However, such simple pressure-ionization models have serious problems during the computation of thermodynamic parameters. The statistical sum over the internal states of the atom is

$$\Sigma_{\rm int} = \sum_{i=1}^{N} s_i w_i \exp(-\beta E_i).$$

For an infinite number of states N (an isolated atom), the sum diverges for any temperature, since $s_i \sim i^2$ (we assume for now that the weight coefficients $w_i = 1$). The formal divergence of this statistical sum points to the existence of the pressure-ionization problem but does not provide a means for its solution. The main problem is related to the fact that, if we assume some $N(\beta, \rho)$, the statistical sum becomes a discontinuous function and cannot be used to compute the thermodynamic corrections. This is a result of the absence of information on the amplitudes of the corresponding corrections: the amplitude of the corrections depends on the assumed width of the transition.

Another approach is used in the MHD EOS. In this case, the statistics of the distribution over states is changed instead of the structure of the spectrum. Additional weights $w_i(\beta, E_i)$ are introduced, which decrease sufficiently rapidly with the state number i and the density to ensure both the convergence of the sum and its convergence to zero with increasing density. Naturally, the choice of weights is based on the independent modeling of the interaction. One of the difficulties of such models is the impossibility of isolating the key parameters describing the transition.

Finally, in a physical picture, it is usual to apply a specific expression for the statistical sum called a

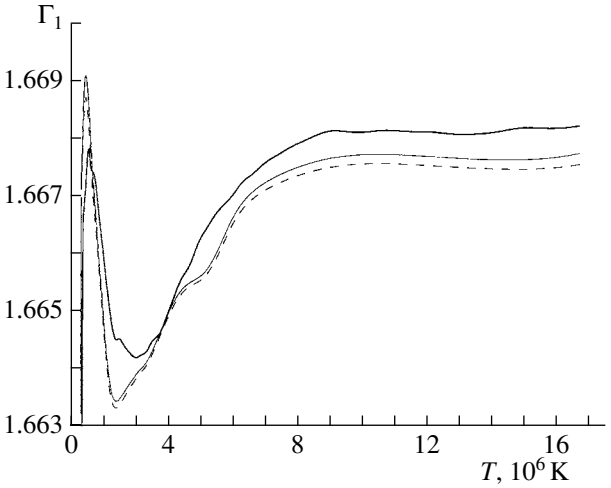

Fig. 3. Comparison of adiabatic exponent Γ_1 in the MHD EOS (thin solid and dashed curves) and the OPAL EOS (thick solid curve). The MHD EOS was computed for the same heavy-element abundance adopted in the OPAL EOS. The dashed curve corresponds to the MHD EOS without the τ correction.

Planck–Larkin partition function [21]:

$$\Sigma_{\rm int}^{PL} = \sum_{i=1}^{\infty} s_i \left[\exp(-\beta E_i) - 1 + \beta E_i\right].$$

Although the formal usage of such an expression in the chemical picture is considered to be an unjustified extrapolation (the expression itself is obtained by summing the series in the quantum-mechanical expansion in physical picture), it is clear that the Mott transition can be expected to occur at a temperature on the order of the ionization potential; i.e., at $\beta I \simeq 1$ (for hydrogen, this is about 1.6×10^5 K). It is important that the partition function does not depend on the density.

Thus, two conditional limits constrain the pressure-ionization models: a transition to complete ionization that depends on the density and a transition that depends only on the temperature. The position of the transition region inside the star is somewhat different for the two limits. In the Sun, the transition due to the temperature occurs earlier (in the outer parts of the convective zone) than the transition due to the density. The distance between the transitions grows with the stellar mass; i.e., the critical density is attained at higher temperatures.

The main thermodynamic effect of pressure ionization is to increase the degree of ionization. This increase may occur at any density, since the statistical sum includes all states. However, the main transition to full ionization occurs at temperatures of the order of $\beta I \simeq 1$ or higher, when the matter

is already strongly ionized. Therefore, the thermodynamic corrections are relatively small. For instance, for the Sun, the degree of ionization in the hydrogen convective zone approaches 98%, yet the expected effect is proportional to the fraction of neutral atoms remaining. In higher-mass stars, the effect is even weaker, since the degree of ionization is higher for the same temperature. At low temperatures, in ionization zones, the phenomenon of a "freezing" of inner states is observed. This is related to the fact that, for large βI (low temperatures), there exists a considerable range of limiting values $N \sim 5$–20, within which the choice of N does not influence the resulting Σ_{int} at al (due to the small exponential coefficient). Thus, the effect is relatively small and the process of ionization in the chemical picture can be described relatively precisely.

However, there also exists an indirect manifestation of pressure ionization. The variability of the statistical sum implies variations of the chemical potential. As a result, corrections to the pressure and other quantities appear in the EOS. These corrections can be computed in the chemical picture, and are proportional to the derivatives of the statistical sum: $\beta\delta p^Z \sim -n_s\left(\partial \log Z^s_{\text{int}}/\partial \log \rho\right)$ and $\beta u^Z \sim n_s\left(\partial \log Z^s_{\text{int}}/\partial \log T\right)$. The pressure correction is always nonnegative (the effective forces are repulsive). In a model with a statistical sum Σ^{PL}_{int} that depends on the temperature alone, only corrections to the internal energy exist, and, in a linear approximation, the variation of the adiabatic exponent is positive. A preliminary analysis shows that, in the same approximation, the statistical sum of a restricted atom (the transition due to density) should lead to negative corrections to Γ_1. The conditional character of this last statement is due to the fact that the resultant sign of the variation of Γ_1 depends on several additional assumptions: the precise form of Σ_{int}, the variation of Γ_1 as a result of variations of the statistical sum itself, and the indirect correction to the chemical potential. We can make the general statement that the variation of the adiabatic exponent enables us to discriminate between the models for the transition to full ionization. Moreover, a method close to the Planck–Larkin function is realized in the OPAL EOS. A comparison of Γ_1 in the MHD and OPAL EOSs reveals some excess adiabatic exponent in the deep part of convection zone (Fig. 3). This excess adiabatic compressibility can be considered as an incentive to bring the solar model into agreement with the results of helioseismic inversion [8].

6. CONCLUSIONS

Let us briefly summarize the picture described above (specific conclusions on the thermodynamic models were given at the end of the corresponding sections). In stars with weak degeneracy, ionization occurs at low temperatures. This means that the ionization zone and the region where the temperature is of the order of the hydrogen ionization potential are separated (in dense stars, the gap between them may disappear, and the situation becomes much more complicated).

The maximum Debye nonideality occurs just beyond the ionization zone, in a low-temperature region. The thermodynamic model profile through the ionization zone lies steeper than the level of constant nonideality. Therefore, the nonideality decreases with decreasing degeneracy parameter. The thermodynamic effect of the pressure ionization shows up in the region of high temperatures, where the material is already strongly ionized and the fraction of nonionized atoms is small. Thus, its direct manifestations in the EOS are not large, and they should decrease for more massive stars.

The regions of temperature and pressure ionization are critical for both the chemical and physical pictures. The chemical picture has difficulties in describing the pressure ionization but is accurate enough for the region of lower temperatures. The physical picture appears to be quite accurate at high temperatures, right up to the ionization zones. Thus, the most important problem is the matching of the two models in this intermediate region.

7. ACKNOWLEDGMENTS

This study was supported by the Russian Foundation for Basic Research (project code 00-02-16226). The authors also acknowledge support from the National Science Foundation (grant AST 9987391).

REFERENCES

1. *Encyclopedia of Low-Temperature Plasma,* Ed. by V. E. Fortov [in Russian] (Nauka, Moscow, 2000), Vol. 1.
2. D. O. Gough and N. O. Weiss, Mon. Not. R. Astron. Soc. **176**, 589 (1976).
3. V. A. Baturin and S. V. Ayukov, Astron. Zh. **73**, 259 (1996) [Astron. Rep. **40**, 233 (1996)].
4. J. Christensen–Dalsgaard and W. Däppen, Astron. Astrophys. Rev. **4** (3), 267 (1992).
5. W. Däppen, D. Mihalas, D. G. Hummer, and B. W. Mihalas, Astrophys. J. **332**, 261 (1988).
6. F. J. Rogers, F. J. Swenson, and C. A. Iglesias, Astrophys. J. **456**, 902 (1996).
7. V. A. Baturin, W. Däppen, D. O. Gough, and S. V. Vorontsov, Mon. Not. R. Astron. Soc. **316**, 71 (2000).
8. V. A. Baturin and S. V. Vorontsov, in *IAU Symp. 181: Sounding Solar and Stellar Interiors,* Ed. by J. Provost and F.-X. Schmieder (Obs. Cote d'Azur, Nice, 1998), Poster Vol., p. 67.

9. S. Basu, W. Däppen, and A. Nayfonov, Astrophys. J. **518**, 985 (1999).
10. P. Debay and E. Hückel, Physic. Zeit. **24** (9), 185 (1923).
11. A. B. Schmidt, *Statistical Thermodynamics of Classical Plasmas* [in Russian] (Énergoatomizdat, Moscow, 1991).
12. H. Shibahashi, A. Noels, and M. Gabriel, Astron. Astrophys. **123**, 283 (1983).
13. S. V. Vorontsov, V. A. Baturin, and A. A. Pamyatnykh, Mon. Not. R. Astron. Soc. **257**, 32 (1992).
14. V. E. Fortov and I. T. Yakubov, *Physics of Non-Ideal Plasmas* [in Russian] (Chernogolovka, 1984).
15. W. Ebeling, W.-D. Kraft, and D. Kremp, *Theory of Bound States and Ionization Equilibrium in Plasmas and Solids* (Academie, Berlin, 1976; Mir, Moscow, 1979).
16. G. M. Harris, J. E. Roberts, and J. G. Trulio, Phys. Rev. **119**, 1832 (1960).
17. V. A. Baturin, W. Däppen, X. Wang, and F. Yang, in *Stellar Evolution: What Should be Done,* Ed. by A. Noels, D. Fraipont-Caro, M. Gabriel, *et al.*, Univer. Liège, 23.
18. W. Ebeling, G. Kelbg, and G. Schmitz, Ann. Phys. **18**, 29 (1966).
19. A. A. Likal'der, Zh. Éksp. Teor. Fiz. **56**, 240 (1969) [Sov. Phys. JETP **29**, 133 (1969)].
20. R. Abe, Prog. Theor. Phys. **21**, 475 (1959).
21. F. J. Rogers, Astrophys. J. **310**, 723 (1986).

Translated by L. Yungel'son

Astronomy Reports, Vol. 47, No. 8, 2003, pp. 694–700. Translated from Astronomicheskiĭ Zhurnal, Vol. 80, No. 8, 2003, pp. 753–760.

MHD Simulations of Current-Sheet Formation over a Bipolar Active Region

I. M. Podgorny[1] and A. I. Podgorny[2]

[1] *Institute of Astronomy, Russian Academy of Sciences, Pyatnitskaya ul. 48, Moscow, 109017 Russia*

[2] *Lebedev Institute of Physics, Russian Academy of Sciences, Leninskiĭ pr. 53, Moscow, 117924 Russia*

Received January 25, 2003; in final form, March 14, 2003

Abstract—We present the results of numerical simulations of the development of a current sheet in the solar corona over a bipolar region during the emergence of two new sunspots arranged collinearly with older spots. Two fronts of increased plasma density form at the boundary of the rising new magnetic flux. One of these is due to the generation of a current sheet, whose magnetic field accumulates energy for a flare. The other front is a branch of the density perturbation, and separates the old and new magnetic fluxes in a region where the magnetic field lines have the same direction on both sides of the boundary. The development of this perturbation is not associated with the energy accumulation in the corona, and hinders observation of the preflare state and complicates analysis of the results. This second front can be interpreted as the eruption of a filament before the onset of the flare. A scheme conservative with respect to magnetic flux was introduced in the *Peresvet* code that solves the MHD equations, in order to suppress numerical instabilities in regions of large magnetic-field gradients. © *2003 MAIK "Nauka/Interperiodica"*.

1. INTRODUCTION

Bipolar regions are rather widespread features consisting of two sunspots of opposite polarities, which move over the solar disk from the eastern to the western limb. The two spots are called the preceding, or leading, spot and the following spot. Leading spots in the northern and southern hemispheres normally have opposite polarities (see, e.g., [1]). These regularities in the appearance of bipolar regions are among the principal arguments for the existence of an azimuthal magnetic field of the Sun, which periodically alternates with the dipolar field because of the differential rotation of the Sun [2]. The appearance of a bipolar region is interpreted as the emergence of a small segment of a magnetic flux tube of azimuthal field, while the spots are sites where the tube issues from or returns below the photosphere.

As two new sunspots (i.e., a new magnetic arch) nearly aligned with the older spots appear in a bipolar region, the oppositely directed magnetic field lines of the old and new fluxes can reconnect, forming a current sheet. The energy stored in the current sheet can be released during a flare. The field configuration necessary for the development of a current sheet can arise if the polarities of the four sunspots alternate. A flare of this type was first observed by Dere [3], and we have performed numerical MHD simulations of the development of a current sheet during such an event [4]. Simulation of the slow growth of the magnetic field of the new spots requires time-consuming computations to reproduce the large magnetic-field gradients at the photospheric boundary. Large gradients lead to numerical instabilities due to the fact that the finite-difference analog of div$\mathbf{B}$ is not exactly equal to zero. The resulting parasitic current distorts the plasma flow and prevents accurate reproduction of the physical pattern of the flare-energy accumulation. Although the first simulations of [4] were relatively imperfect, we were able to convincingly demonstrate the formation of a current sheet resulting from the emergence of new flux, with an accumulation of flare energy over an active region.

Here, we attempt to numerically reproduce the overall pattern of the plasma dynamics during the formation of a current sheet. To suppress numerical instabilities at the photospheric boundary, we use a modified version of the *Peresvet* code based on a scheme conservative with respect to magnetic flux. The growth time of the emerging flux is increased by an order of magnitude. The use of new computing facilities enabled us to employ a 241×241 grid instead of the 41×41 grid used in previous studies. All these improvements enable detailed studies of the changes in the field configuration accompanying the emergence of new sunspots and make it possible to trace the formation and evolution of the current sheet until the sheet thickness becomes comparable to the spatial-integration step. Together with the formation of a current sheet, strong coronal disturbances unrelated to the flare-energy accumulation develop over the active region.

1063-7729/03/4708-0694$24.00

2. THE NUMERICAL SIMULATIONS

We employed a new version of the *Peresvet* code that solves the full set of MHD equations [5]. All dissipative processes, the compressibility of the plasma, and the anisotropy of the plasma's thermal conductivity in a magnetic field were taken into account. An implicit scheme ensuring highly stability of the computations was used. We developed a finite-difference scheme conservative with respect to magnetic flux to suppress numerical instabilities in regions of large magnetic-field gradients at the photospheric boundary. We used the averaged magnetic fluxes through the faces of the computational-grid cells per unit area as the magnetic-field values. The current density at the cell edges was determined by computing a finite-difference analog of the curl of the magnetic field from the field values at the faces adjacent to a given edge. The velocity components, plasma density, and temperature were determined at the grid points, or cell corners. The magnetic field and electric-current density in the equations of motion and energy transfer were determined at the grid points by interpolating their values at the cell faces and edges. The velocity components normal to an edge, which appear in the cross product of the velocity and the magnetic field, were determined by interpolating over the grid points at the ends of the edge. The magnetic-field component that is multiplied by the velocity component orthogonal to it was taken at the edge of the adjacent cell, at the side opposite to the direction of this velocity component. The finite-difference analog of the curl of the electric field, which forms the right-hand side of the magnetic-field equation, was calculated at the face corresponding to the given magnetic-field component, using the electric-field values at the edges adjacent to this face.

The magnetic flux through the boundary of each cell remains zero as a time step is made, since any edge adjoins two faces of the given cell. The electric fields subject to the curl operator in the right-hand side of the equation cancel when the magnetic fluxes are summed over the faces of the given cell. This summation determines the magnetic flux through the cell boundary. The vanishing magnetic flux through the boundary means that the finite-difference analog of the divergence is zero.

The basic principles of simulating coronal MHD processes are presented in [5, 6]. A detailed description of the system of equations that are solved and the corresponding boundary conditions are given in [7].

All the computation results are represented in dimensionless units and are valid for any plasma parameters in the region over the active region. We chose the size of the computational domain L_0 to be the unit length. This scale corresponds to the typical size of an active region, i.e., $L_0 \sim 10^{10}$ cm. Thus, the computations were carried out for the domain $0 \le X \le 1, 0 \le Y \le 1$. The mean photospheric magnetic field B_0 in the active region is used as the unit of the magnetic field. The units of the plasma density, ρ_0, and temperature, T_0, are their values in the solar corona, which we took to be constant in space at the initial time. As the units of the velocity, time, plasma density, current density, and dipole magnetic moment, we used the Alfvén speed $V_0 = V_A = B_0/\sqrt{4\pi\rho_0}$, $t_0 = L_0/V_0$, the coronal density ρ_0, $j_0 = cB_0/(4\pi L_0)$, and $M_0 = B_0 L_0^3$. For a magnetic flux in the bipolar region of 10^{22} Mx, an average magnetic field of $B_0 \sim 100$ G and a density of the hydrogen plasma over this region of $\sim 10^8$ cm^{-3}, the Alfvén speed is $V_A \sim 2 \times 10^9$ cm/s and the time unit is ~ 10 s. The speed of sound is $C_S = V_A(\beta\gamma/2)^{1/2} \sim 7 \times 10^7$ cm/s. The main results were obtained with a 241×241 grid.

The field of the bipolar region was specified in the form of two vertical dipoles of opposite polarities placed under the photosphere. The following nondimensional parameters were chosen for the main computational runs: magnetic Reynolds number $\mathrm{Re}_m = 10^4$, normal Reynolds number $\mathrm{Re} = 10^4$, gas-to-magnetic pressure ratio $\beta = 10^{-4}$, Peclet number $\Pi = 100$, and Peclet number for thermal conduction across the magnetic field $\Pi_B = 10^8$. As the moment of the two new dipoles was increased, a current sheet developed, and solar-flare energy was accumulated in its magnetic field.

3. CURRENT-SHEET FORMATION

Figure 1a shows the magnetic field of a bipolar region approximated by two vertical magnetic dipoles placed under the photosphere. Their magnitudes and positions are as follows: $\mu_1 = 0.25$, $\mathrm{X}_1 = 0.1$, $\mathrm{Y}_1 = -0.5$, and $\mu_2 = -0.25$, $X_2 = 0.45$, $Y_2 = -0.5$. At $t = 0$, the magnetic moments of two other dipoles, μ_3 and μ_4, begin increasing linearly; they are located at the points $X_3 = 0.78$, $Y_3 = -0.2$ and $X_4 = 0.85$, $Y_4 = -0.2$. By $t_{\mathrm{cease}} = 50$ (which corresponds to about 10 min), their magnitudes reach $+0.2$ and -0.2, respectively. At $t > 50$, the magnetic moments of all the dipoles are kept constant. Simultaneous with the appearance of a magnetic arch between the dipoles μ_3 and μ_4, a current sheet begins to form at the interface between the oppositely directed field. The current sheet separates the coronal plasma expelled by the growing magnetic flux and the fresh plasma ascending from the chromosphere together with the frozen-in magnetic field. By $t \sim 10$, the current sheet can clearly be distinguished in the magnetic configuration. The magnetic-field lines at $t = 11$ are shown

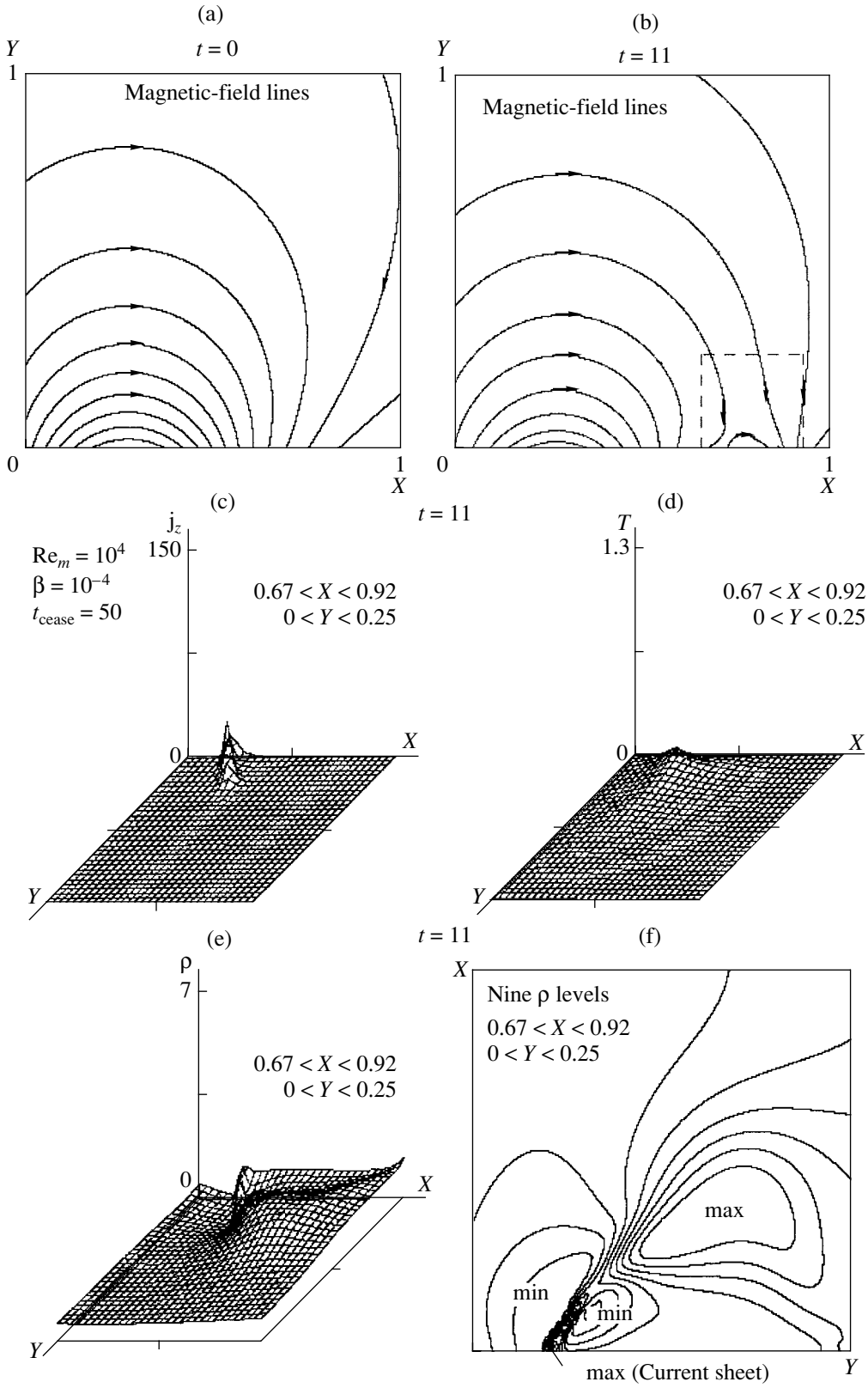

Fig. 1. (a) Magnetic-field lines in the bipolar region, (b) magnetic-field lines after the formation of two new sunspots at $t = 11$, (c) current-density distribution in the current sheet, (d) temperature distribution, (e) density distribution, and (f) nine density contours.

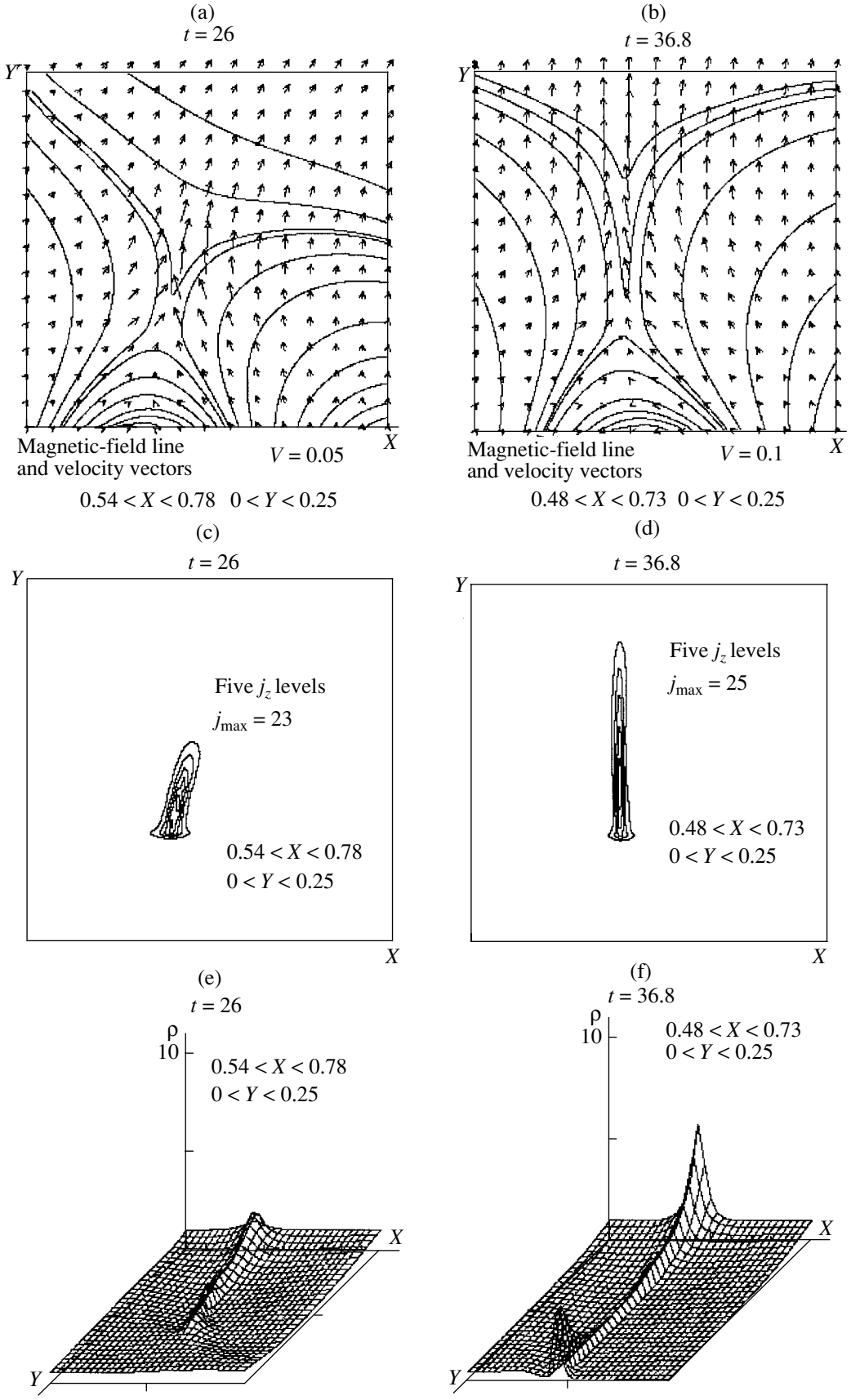

Fig. 2. Magnetic-field lines near the current sheet at (a) $t = 26$ and (b) $t = 36$; (c, d) contours of current density and (e, f) plasma-density distributions for the same times.

in Fig. 1b. The region of formation of the current sheet is outlined by the dashed square. Below, we represent all events on the scale of this square. The current-density distribution in the sheet is illustrated in Fig. 1c, and Fig. 1d shows the temperature distribution. The increase in temperature is due to Ohmic heating in the current sheet.

The distribution of plasma density is fairly complex (Fig. 1e). In addition to the increased plasma density in the current sheet, there is a flat, higher peak to the right of the current sheet, as follows from the balance of the magnetic and plasma pressures. The structure of the plasma-density distribution is more clearly visible in Fig. 1f, which shows contours of the plasma density. The plasma-density increase in the current sheet can clearly be seen. There are extended regions of reduced density (min) on both sides of the layer. These are a characteristic feature of current-sheet formation, since the flow of plasma into the sheet produces regions of reduced plasma density, and the ambient plasma has no time to fill these regions. The flow pattern is quite evident from Figs. 2a and 2b. The plasma flows into the sheet through both sheet boundaries. The velocity component normal to the sheet increases as the plasma approaches the sheet boundaries, leaving behind regions of reduced density. This acceleration of the flow as it approaches the sheet and the thinning of the sheet with time are manifestations of the pinch effect. As this takes place, the length of the sheet continuously increases, as does the energy stored in the magnetic field.

A broad maximum in which the direction of the field does not vary is located to the right of the current sheet. The field strength is nearly the same on both sides of the maximum, and the current is vanishingly small in this region. No magnetic energy is accumulated there. Like the current sheet, this diffuse plasma-density peak separates the old coronal plasma and the fresh plasma that ascends together with the emerging field lines. The rate of the displacement of the maximum is about 0.02, or $\sim 0.5 C_S$.

Thus, the interface between the old and fresh plasmas has two branches. The left branch, which separates fields with opposite directions, is the current sheet. This current sheet, like all current sheets that are formed in nature or in the laboratory, is not neutral. The plasma is accelerated by the magnetic tension, mainly in the upward direction. Downward acceleration is less efficient, since downward-moving reconnected field lines produce a new magnetic arch with a high plasma density below the current sheet, and this arched field subsequently decelerates the moving plasma. Plasma streams directed downward from a region of reconnection were observed by McKenzie and Hudson [8]. The high plasma density in the region of arched field lines below the current sheet can be seen in Fig. 2f. This process of concentrating arched field lines with high plasma densities below the sheet forms the outer part of the postflare loop below the vertical current sheet [9].

The evolution of the current sheet is illustrated in Fig. 2. As it accumulates magnetic energy, the current sheet becomes progressively longer and thinner. It turns, approaching the vertical direction. By $t \sim 30$, its thickness becomes comparable to the spatial integration step. In contrast to the rapidly moving right branch, the current sheet remains almost stationary. Its further development is largely determined by numerical rather than physical effects.

4. PROPAGATION OF THE FRONT OF ENHANCED DENSITY

We studied the propagation of the front of enhanced density (which is not directly related to the formation of the current sheet) for conditions under which the current sheet cannot form. We considered the emergence of two spots in a region where no spots were originally present. We specified the conditions $\mu_1 = \mu_2 = 0$, while the growth of the dipoles μ_3 and μ_4 followed the same law as in the preceding computational run.

In this case, the front of enhanced density propagates upward with a speed exceeding the speed of sound by almost a factor of 1.5 ($V \sim 10^8$ cm/s), producing a shock wave. Recall that, when this front traveled in the strong magnetic field of a bipolar region, its speed was half the sound speed. The front separates the coronal plasma, in which $B = 0$, from the plasma coupled with the frozen-in emerging magnetic flux. The velocity field of the expanding plasma is shown in Figs. 3a and 3b together with density contours and magnetic-field lines. The density distribution is symmetric in this case (Fig. 3c). The density of the expanding plasma decreases slowly with distance from the Sun (Fig. 3d) and increases sharply at the front. The plasma-velocity front coincides with the plasma-compression front due to interaction with the coronal plasma. It also coincides with the boundary of the region occupied by the magnetic field, in which $\mathrm{curl}\mathbf{B} \neq 0$. The current-density maximum also coincides with the density maximum, which develops due to the deceleration of the plasma expanding together with the magnetic field as this plasma interacts with the coronal plasma, in which $B = 0$. The absence of a magnetic field in the coronal plasma reduces the pressure $P + B^2/8\pi$, which decelerates the ascending front, and the front travels more rapidly in this case than in the preceding run (Fig. 1). As the plasma expands, its velocity increases (Fig. 1d) and reaches its maximum at the

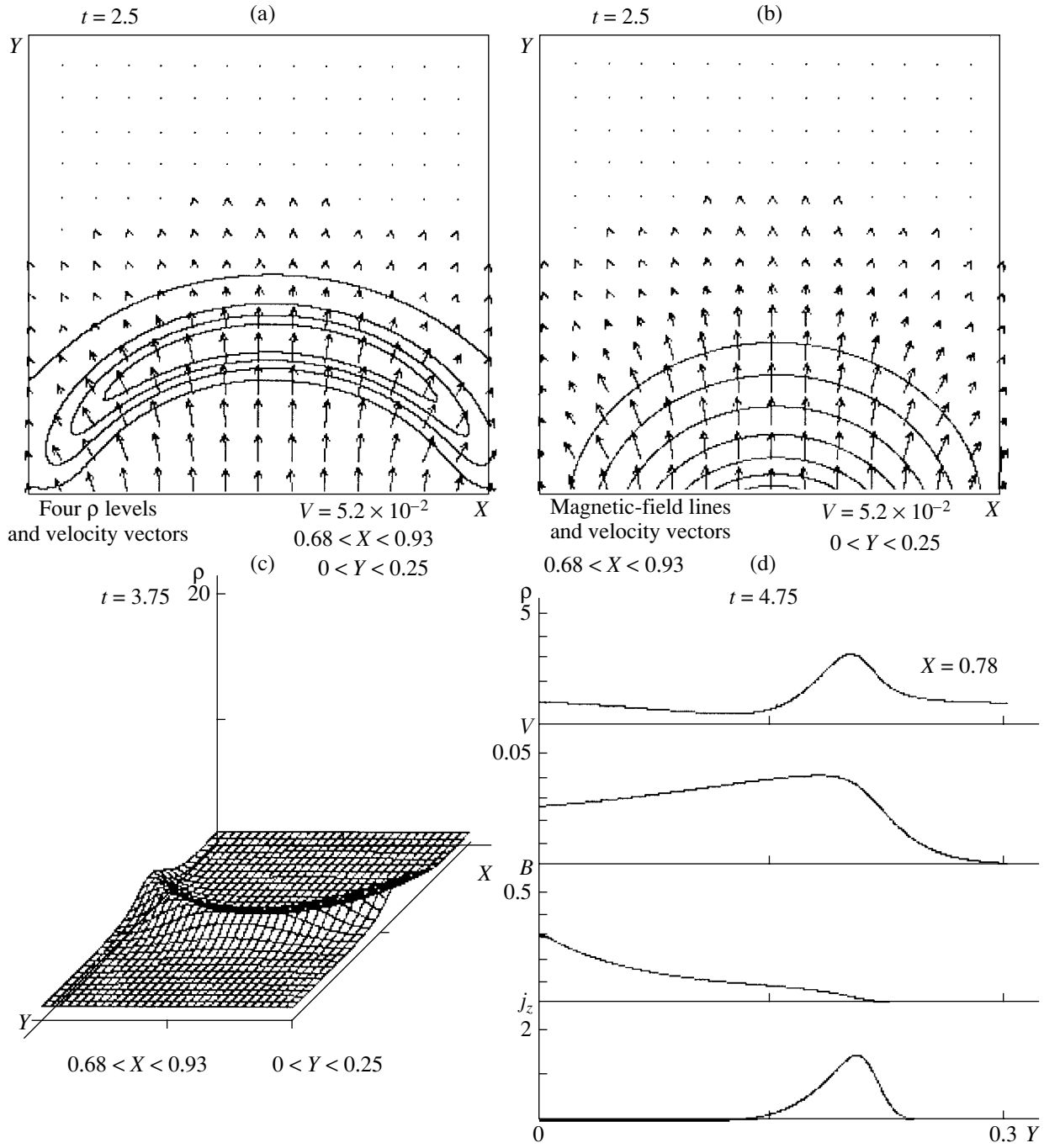

Fig. 3. Emergence of magnetic flux in the absence of an initial field: (a) density contours and velocity vectors, (b) magnetic-field lines and velocity vectors, (c) plasma-density distribution, and (d) vertical profiles of the parameters of the plasma and magnetic field.

front, after which it falls abruptly at the boundary with the unperturbed corona.

The plasma-compression front leaves the active region at a high velocity, while the current sheet remains virtually stationary during the preflare phase, only slowly changing its inclination to the solar surface. This highly dynamic behavior of the compression front can produce the illusion that this front plays a leading role in the initial stage of the flare.

5. CONCLUSIONS

The slowly increasing magnetic field of two new spots in a bipolar region expels the coronal plasma

together with the frozen-in magnetic field lines. Simultaneously, the cavity is filled with ascending chromospheric plasma carrying fresh magnetic flux. In the numerical simulations, the chromospheric-plasma density was kept constant, and the vertical temperature gradient was neglected. A front of enhanced density arises at the interface between the fresh and old (coronal) plasmas. This front consists of a left and a right branch. The slowly evolving left branch is a classic current sheet with a normal magnetic-field component, i.e., a layer of increased density and temperature separating oppositely directed magnetic fields. The plasma flows into this layer through its side boundaries and is accelerated along the layer by the magnetic tension. The magnetic field of the layer accumulates a magnetic energy $\int (B^2/8\pi)dv$, which can be released during the breakdown of the current sheet, giving rise to a flare. The upward acceleration of plasma along the sheet by the magnetic tension should lead to its ejection into interplanetary space during the flare. The downward acceleration of plasma results in the formation of a postflare loop.

Energy is accumulated in the field of the current sheet because of the high stability of the sheet when it is forming. The sheet is stabilized by the plasma flow along the sheet due to the $\mathbf{j} \times \mathbf{B}/c$ force, provided a normal component of the magnetic field is present. This quasisteady flow should be maintained until the transition to an unstable state takes place due to the decrease in the plasma density near the sheet. The regions of density decrease are shown in Fig. 1f. The transition to the unstable state results from the mass loss by the sheet as the plasma is expelled by the magnetic tension, and the mass loss is no longer balanced by the inflow of plasma through the side boundaries of the sheet. The formation of the current sheet is possible only because it is not neutral. Numerous theoretical studies appearing after 1963 have suggested that the instability of a neutral current sheet grows rapidly; therefore, a neutral sheet can only develop (if this is possible at all) on a time scale shorter than the time for the development of the instability. Thus, a neutral current sheet cannot be a reservoir for a slow preflare accumulation of energy that is then rapidly released during a flare. For this reason, a neutral current sheet cannot exist in a steady or quasisteady state. Indeed, all current sheets observed in nature or simulated numerically possess a normal magnetic-field component.

The right branch of the front of enhanced density moves upward fairly rapidly as the region occupied by the freshly emerging magnetic flux expands. This branch is not related to the accumulation of magnetic energy that could be released during a flare, since the magnetic fields on either side of this branch have the same direction and are nearly equal. The current density $\mathbf{j} = (c/4\pi)\mathrm{curl}\mathbf{B}$ is negligibly small here. The profile of the right-branch density front is determined by the deceleration of the plasma expanding together with the emerging field as this plasma interacts with the coronal plasma. Electrodynamic forces do not seem to be the determining ones here. According to our computations, the ejection of such a front of increased density is also possible in the absence of spots in the region considered. In such cases, the current at the front (Fig. 3d) produces a $\mathbf{j} \times \mathbf{B}/c$ force that accelerates the expanding plasma, in addition to the acceleration produced by the pressure gradient. As a result, the front propagation becomes supersonic.

Observationally, the appearance of the right branch of the density-increase profile can mask the main phenomena related to the formation of the current sheet and the accumulation of flare energy. This is especially important in the earliest stages, when the left branch of the front is still near the chromosphere. The two branches of the front can be misinterpreted as loops whose interaction gives rise to a flare [10]. The propagation of the right branch of the front can also be considered a possible preflare ejection of a filament.

ACKNOWLEDGMENTS

This work was supported by the Russian Foundation for Basic Research (project code 01-02-16186) and the State Science and Technology Program "Astronomy."

REFERENCES

1. E. Priest, *Solar Magnetohydrodynamics* (Reidel, Dordrecht, 1982; Mir, Moscow, 1985).
2. R. B. Leighton, Astrophys. J. **156**, 1 (1969).
3. K. P. Dere, J.-D. F. Bartoe, G. E. Brueckner, *et al.,* J. Geophys. Res. **96**, 9399 (1991).
4. A. I. Podgorny and I. M. Podgorny, Astron. Zh. **78**, 71 (2001) [Astron. Rep. **45**, 60 (2001)].
5. A. I. Podgorny and I. M. Podgorny, *Solar Drivers of the Interplanetary and Terrestrial Disturbances*, ASP Conf. Ser. **95**, Ed. by K. S. Balasubramaniam, S. L. Keil, and R. N. Smartt (Astron. Soc. Pacif., San Francisco, 1996), p. 66.
6. A. I. Podgorny, Solar Phys. **156**, 41 (1995).
7. I. L. Bilenko, A. I. Podgorny, and I. M. Podgorny, Solar Phys. **207**, 323 (2002).
8. D. E. McKenzie and H. S. Hudson, Earth Planet. Space **53**, 577 (2001).
9. A. I. Podgorny and I. M. Podgorny, Astron. Zh. **79**, 73 (2002) [Astron. Rep. **46**, 67 (2002)].
10. J. Zhang and J. Wang, Solar Phys. **196**, 377 (2000).

Translated by A. Getling

Astronomy Reports, Vol. 47, No. 8, 2003, pp. 701–708. Translated from Astronomicheskiĭ Zhurnal, Vol. 80, No. 8, 2003, pp. 761–768.

Electron Acceleration in the Ionosphere of Io

V. V. Zaĭtsev[1], V. E. Shaposhnikov[1]*, and H. O. Rucker[2]

[1] *Institute of Applied Physics, Russian Academy of Sciences, ul. Ul'yanova 46, Nizhni Novgorod, 603600 Russia*

[2] *Space Research Institute of Austrian Academy of Sciences, Schmiedlstrasse 6, Graz, A-8042 Austria*

Received February 18, 2003; in final form, March 14, 2003

Abstract—A mechanism for the acceleration of electrons in the ionosphere of Io due to the moon's motion through the Jovian magnetic field and the presence of Io's ionosphere is considered. Attention is drawn to the important role of the anisotropic conductivity of the ionosphere, which results in the formation of a longitudinal (with respect to the planetary magnetic field) component of the charge-separation electric field. Owing to this anisotropy, the electric field induced by the motion of Io, $\mathbf{E}_i$, produces in Io's ionosphere not only a Pedersen electrical current along $\mathbf{E}_i$ but also a Hall current that is approximately perpendicular to the moon's surface in the "upstream" and "downstream" parts of the ionosphere. However, this current cannot be closed through the surface, leading to the formation of a powerful charge-separation field in Io's ionosphere. This field has a component parallel to the magnetic field, with an amplitude comparable to that of the induced electric field. Electron runaway along the magnetic field is also considered, and the occurrence of "active longitudes" and preferred locations for the sources of decametric radio emission in the northern hemisphere of Jupiter are interpreted. The characteristic energies and fluxes of the accelerated electrons injected into Io's flux tube are estimated. The energy of these electron fluxes is sufficient to produce the electromagnetic radiation observed from Io's magnetic tube. © *2003 MAIK "Nauka/Interperiodica"*.

1. INTRODUCTION

Electromagnetic interactions between Io, the large moon that is closest to Jupiter, and the Jovian magnetosphere substantially affects processes in the ionosphere and lower magnetosphere of the planet. The first (and, for a long time, the only) observational evidence for this interaction was a correlation between the occurrence of Jovian decameter radio emission and the position of Io, discovered in 1964 by Bigg [1]. This correlation points to an electron-acceleration mechanism associated with Io. Further observational evidence for an electrodynamic interaction between Io and the Jovian magnetosphere is the appreciable increase in the fluxes of energetic electrons with energies $\lesssim 100$ keV and of ions with energies ~ 100 eV in the L shells of Io, discovered by the *Pioneer* and *Voyager* spacecraft [2–5]. Recent observations by *Galileo* in the vicinity of Io have provided new confirmation of the presence of strong electrodynamic interactions of Io with the planetary magnetosphere [6–10]. Magnetometer measurements have revealed a decrease in the magnetic-field intensity in the tail of Io by almost 40%. In addition, passing over the surface of Io at an altitude of about 900 km, *Galileo* detected beams of fast electrons with energies exceeding 15 keV near the satellite's poles, moving along magnetic-field lines passing through Io. These beams propagate in both directions along the magnetic field and have approximately equal intensities. On the other hand, *Galileo* did not detect fast electrons with energies over 150–200 keV. This may provide evidence that only some fraction of the induced electric potential ~ 500 kV [11] applied to Io is manifest in the form of accelerated electrons moving along the magnetic field.

The acceleration of charged particles in the Jupiter–Io system has been studied in many papers. For example, the electrical circuit composed of Io, a magnetic tube, and the Jovian ionosphere was analyzed in [12–14] assuming a steady-state current. The aim was to determine the region in which there is a sufficiently large component of the electric field along the magnetic field to imply a substantial potential difference. It has usually been assumed that this takes place in double plasma layers localized either near Io's surface [12, 13] or in the magnetic tube, near the surface of Jupiter [14]. However, the existence of such double plasma layers does not follow directly from the analysis of the electric circuit and is only postulated. As is noted in [15], the Alfvén velocity decreases sharply when Io crosses the plasma torus, so that Alfvén waves generated by Io and carrying a longitudinal electric current cannot close the electric circuit composed of Io, the magnetic tube, and the Jovian ionosphere. In this case, the electrons are assumed to be accelerated by interaction with the

*E-mail: sh130@appl.sci-nnov.ru

1063-7729/03/4708-0701$24.00

Alfvén waves (similar to Fermi acceleration). However, this acceleration depends on the availability of a sufficiently large number of fast particles, which can be synchronous with the Alfvén waves propagating from Io. Another mechanism for the formation of the longitudinal electric field due to ionization processes in Io's ionosphere was considered in [16], but this mechanism can accelerate electrons only to a few eV and, therefore, can only facilitate the injection of particles into the main acceleration regime.

Therefore, the acceleration mechanism resulting in the formation of well-collimated electron beams moving in opposite directions along the magnetic-field lines intersecting Io remains unclear.

In the present paper, we will pay special attention to the important role of anisotropic conductivity in the formation of the longitudinal electric-field component in Io's ionosphere. If the magnetic field is taken into consideration, the conductivity of Io's plasma envelope is a three-component tensor, which depends substantially on the density of neutral particles in the ionosphere. Owing to the anisotropic conductivity, the induced electric field in a coordinate system comoving with Io,

$$\mathbf{E}_i = \frac{1}{c}\mathbf{V}\times\mathbf{B}, \qquad (1)$$

not only generates in the ionosphere Pedersen currents directed along $\mathbf{E}_i$ but also tends to produce a Hall current orthogonal to Io's surface. The quantity $\mathbf{V}$ in (1) is the velocity of Io with respect to the corotating magnetospheric plasma of Jupiter, $\mathbf{B}$ is the magnetic field near Io, and c is the speed of light. However, the Hall current cannot be closed through the moon's surface. The resulting charge separation generates a powerful electric field, which has a component along the direction of the magnetic field. The amplitude of this electric field depends on the density of neutrals in Io's ionosphere and, under favorable conditions, could be comparable to the induced field E_i.

The electric fields and currents in a layer of partially ionized plasma moving with constant velocity $\mathbf{V}$ through the magnetic field of Jupiter (modeling separate parts of Io's ionosphere) will be calculated in Section 2. The acceleration of electrons in this layer by the longitudinal component of the charge-separation electric field will be considered in Section 3, taking into account the runaway of electrons and probable collective effects, such as the Buneman and ion-acoustic instabilities. Finally, we present an interpretation of the "active longitudes" in the radio emission of Jupiter in Section 4.

2. THE ELECTRIC FIELD IN A LAYER OF PARTIALLY IONIZED PLASMA MOVING THROUGH A GIVEN MAGNETIC FIELD

According to *Galileo* data [6], the ionosphere of Io is at rest with respect to the moon, so that an electric field $\mathbf{E}_i$ given by (1) is induced in the ionosphere by the motion of Io through the magnetic field. In addition, a charge-separation electric field $\mathbf{E}_\mathrm{s}$ is generated in the upstream and downstream regions near Io due to the ionosphere's motion through the magnetic field of Jupiter and the unequal magnetization of the electrons and ions. The corresponding field system is shown schematically in Fig. 1.

Our aim in this section is to estimate the charge-separation electric field generated by the motion of Io through the magnetic field of Jupiter. Let some part of Io's ionosphere be described as a two-dimensional layer of partially ionized plasma with thickness $L \ll R_\mathrm{Io}$ moving with respect to the external magnetic field $\mathbf{B}_0$. This is a reasonable approximation, since the characteristic thickness of the plasma envelope surrounding Io is about an order of magnitude smaller than Io's radius. Let us adopt a coordinate system whose x axis is in the plane of the vectors $\mathbf{V}$ and $\mathbf{B}_0$ and is directed at an angle α to the velocity $\mathbf{V}$ (i.e., perpendicular to the layer boundary), and whose y axis is orthogonal to $\mathbf{V}$ and $\mathbf{B}_0$ (Fig. 2). We will take the plasma to be a partially ionized gas of electrons (e) with density n_e and mass m_e, ions (i) with density n_i and mass m_i, and neutral atoms (a) with density n_a and mass m_a. For simplicity, we will assume that the ions are singly ionized, so that $n_e \simeq n_i \simeq n$.

To study the electric fields generated by the motion of the plasma layer in the magnetic field $\mathbf{B}$, let us write the generalized Ohm's law [17]:

$$\mathbf{E}+\mathbf{E}_i = \frac{\mathbf{j}}{\sigma} + \frac{1}{nec}[\mathbf{j}\times\mathbf{B}] - \frac{\nabla p_e}{en} - \xi\frac{F}{c^2 n m_i \nu'_{ia}}[[\mathbf{j}\times\mathbf{B}]\times\mathbf{B}], \qquad (2)$$

where $\mathbf{E}_i$ is the "external" electric field generated in the layer due to its motion through the magnetic field $\mathbf{B}_0$ and described by (1), $\mathbf{j}$ is the electric current density, $\mathbf{B}$ is the self-consistent magnetic field in the acceleration region, e is the electron charge,

$$\sigma = \frac{e^2 n}{m_e(\nu'_{ea}+\nu'_{ei})} \qquad (3)$$

is the plasma conductivity along the magnetic field, and

$$\nu'_{ea} = \frac{m_a}{m_a+m_e}\nu_{ea}, \quad \nu'_{ia} = \frac{m_a}{m_a+m_i}\nu_{ia}, \quad \nu'_{ei} = \frac{m_i}{m_i+m_e}\nu_{ei} \qquad (4)$$

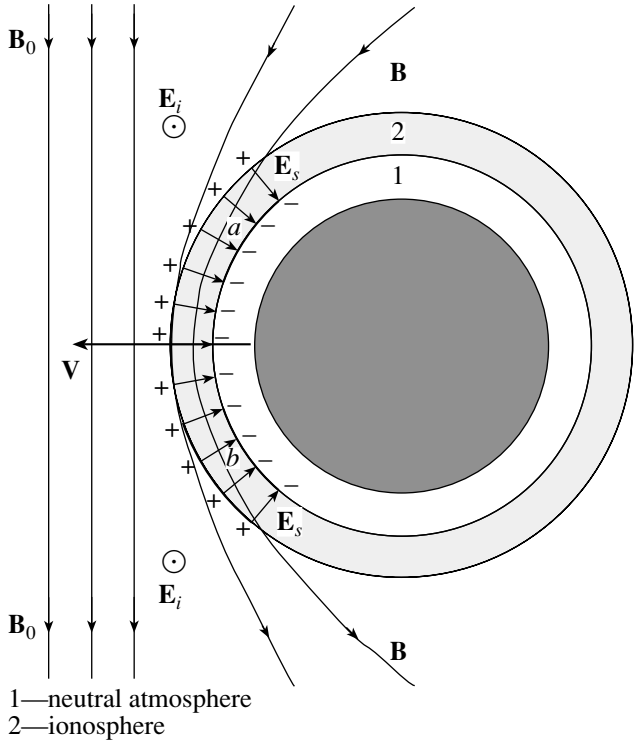

Fig. 1. Field system generated by the motion of Io through the planetary magnetic field $\mathbf{B}_0$. The component of the charge-separation field $\mathbf{E}_s$ along the magnetic field $\mathbf{B}$ has different signs in regions a and b.

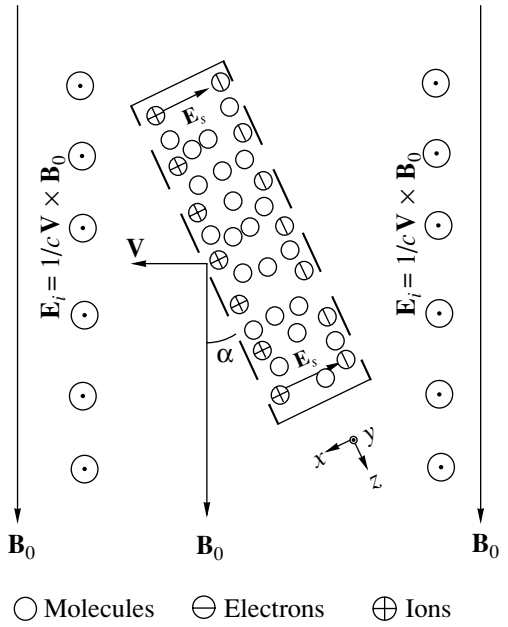

Fig. 2. Schematic of motion of a two-dimensional layer of partially ionized plasma through the external magnetic field $\mathbf{B}_0$. The layer walls are inclined at the angle α with respect to the magnetic field lines.

are the effective rates of collisions of electrons with ions (ν'_{ei}), electrons with neutral particles (ν'_{aa}), and ions with neutrals (ν'_{ia}). The coefficient ξ in (2) depends on the relative density of the neutral component,

$$F \simeq \frac{n_a m_a}{n_a m_a + n_i m_i}, \tag{5}$$

and is determined by the expression

$$\xi = \frac{F^2 m_i}{2m_a(1-F) + m_i F}. \tag{6}$$

If the plasma is weakly ionized ($F \to 1$), $\xi \simeq F$. On the other hand, if the degree of ionization is high ($F \to 0$), $\xi \simeq \frac{F^2 m_i}{2m_a}$. It was assumed in (2) that the plasma is at rest in a coordinate system fixed to the layer—i.e., that the pressure gradient $\nabla p = \nabla p_a + \nabla p_i + \nabla p_e$ is balanced by the Ampère force ($\nabla p = \frac{1}{c}\mathbf{j} \times \mathbf{B}$)—and that the plasma is isothermal ($T_a = T_i = T_e$). Generally speaking, this last condition is not satisfied in Io's ionosphere, but this is not of critical importance for estimating the charge-separation electric field.

Because of the geometric configuration of the problem, all parameters depend only on x; i.e., $\frac{\partial}{\partial y} = \frac{\partial}{\partial z} = 0$. The problem is stationary in a coordinate system fixed to the layer. Therefore, from the relation $\mathrm{rot}\mathbf{E} = -\frac{1}{c}\frac{\partial \mathbf{B}}{\partial t}$, we find that

$$E_y = -\frac{1}{c}VB, \qquad E_z = 0. \tag{7}$$

Taking projections of (2) onto the x, y, and z axes, we obtain

$$E_x = \frac{1}{enc}(j_y B_z - j_z B_y) - a(j_z B_x B_z + j_y B_x B_y), \tag{8}$$

$$-\frac{1}{c}VB = \frac{j_y}{\sigma} + \frac{1}{enc} j_z B_x + a\left[j_y(B_z^2 + B_x^2) - j_z B_y B_z\right], \tag{9}$$

$$0 = \frac{j_z}{\sigma} - \frac{1}{enc} j_y B_x + a\left[j_z(B_x^2 + B_y^2) - j_y B_y B_z\right], \tag{10}$$

where

$$a = \frac{\xi}{c^2 n m_i \nu'_{ia}}. \tag{11}$$

As follows from (10), we can assume without loss of generality that $B_y = 0$, since the condition $E_z = 0$ can be satisfied by compensating the term due to the Hall effect $\frac{1}{enc} j_y B_x$ in (10) by the conduction current $\frac{j_z}{\sigma}$ and the z component of $a\,[\mathbf{j} \times \mathbf{B}] \times \mathbf{B}$.

Solving the system of equations (8)–(10) containing the unknown quantities j_y, j_z, and E_x, we obtain

$$j_y = -\frac{1}{c}VB\sigma\frac{1+\xi\omega_e\tau_e\omega_i\tau_i\sin^2\alpha}{A}, \quad (12)$$

$$j_z = -\frac{1}{c}VB\sigma\frac{\omega_e\tau_e\sin\alpha}{A}, \quad (13)$$

$$E_x = -\frac{1}{c}VB\frac{\omega_e\tau_e\cos\alpha}{A}, \quad (14)$$

where

$$A = 1+\xi\omega_e\tau_e\omega_i\tau_i + (\xi\omega_e\tau_e\omega_i\tau_i + \xi^2\omega_e^2\tau_e^2\omega_i^2\tau_i^2 + \omega_e^2\tau_e^2)\sin^2\alpha, \quad (15)$$

$\omega_e = \frac{eB}{m_e c}$, $\omega_i = \frac{eB}{m_i c}$, $\tau_e = (\nu'_{ei}+\nu'_{ea})^{-1}$, and $\tau_i = (\nu'_{ea})^{-1}$. It follows from (14) that the charge-separation field is directed toward the moon's surface in the upstream part of the region near Io and away from the surface in the downstream part. The component of this field along the magnetic field **B**, which is responsible for the particle acceleration, is described by the formula

$$E_{||} = -\frac{1}{c}VB\frac{\omega_e\tau_e\sin\alpha\cos\alpha}{1+\xi\omega_e\tau_e\omega_i\tau_i + (\xi\omega_e\tau_e\omega_i\tau_i + \xi^2\omega_e^2\tau_e^2\omega_i^2\tau_i^2 + \omega_e^2\tau_e^2)\sin^2\alpha}. \quad (16)$$

The quantity $E_{||}$ has different signs on opposite sides of Io's equator (regions *a* and *b* in Fig. 1). Consequently, the charge-separation field formed in Io's ionosphere will produce beams of fast electrons moving along the magnetic field in opposite directions. If the electrons are magnetized more strongly than the ions ($\omega_e^2\tau_e^2 \gg 1$, $\omega_e\tau_e \gg \xi\omega_i\tau_i$), the longitudinal component of the electric field is maximum when $\sin\alpha^* \simeq 1/\omega_e\tau_e$, i.e., when the magnetic field of the incoming stream of particles is almost tangential to the plane of the layer. Then,

$$E_{||}^{\max} \simeq -\frac{1}{2c}VB. \quad (17)$$

When the magnetic-field direction deviates further from the plane of the plasma layer ($\sin\alpha \gg \sin\alpha^*$), the field sharply decreases:

$$E_{||}(\alpha) \simeq -\frac{1}{c}VB\frac{\cos\alpha}{\omega_e\tau_e\sin\alpha}. \quad (18)$$

The topology of the magnetic field near Io is not accurately known. However, it is commonly assumed that the magnetic field of the incoming stream is deformed due to the conduction of Io, so that its field lines adopt the shape of the moon, as if they were flowing around it [18]. This means that a longitudinal electric-field component with values of the order of $E_{||}^{\max}$ can exist on scales about equal to Io's radius. If the magnetic field in the vicinity of Io is $B \simeq B_0 \simeq 1.8\times10^{-2}$ G [7], Io's velocity relative to the corotating Jovian magnetosphere is $V = V_{\rm Io} \simeq 5.7\times10^6$ cm s^{-1}, and Io's radius is $R_{\rm Io} \simeq 1.8\times10^8$ cm, the energy of the accelerated electrons could be as large as $W_e^{\max} \sim \frac{e}{c}V_{\rm Io}BR_{\rm Io} \simeq 100$ keV. This estimate is in agreement with the data obtained by *Galileo*; as was noted in the Introduction, *Galileo* did not detected beams of fast electrons with energies above 150–200 keV.

3. ELECTRON ACCELERATION IN Io's IONOSPHERE

Let us consider in more detail the acceleration of electrons in Io's ionosphere by the field $E_{||}$, described by (16) and (17). The plasma in Io's ionosphere is weakly ionized. According to the model of [19], the electron density in the maximum of the ionospheric layer reaches $n \simeq 6\times10^4$ cm^{-3}, whereas the density of neutrals is $n_a \simeq 10^{10}$ cm^{-3}. The neutral component is composed for the most part of SO_2 molecules, with small admixtures of O, SO, O_2, and Na. The ion component is composed of SO^+, SO_2^+, S^+, O^+, S^{++}, and O^{++} in various proportions. In accordance with the model of [20], we will assume that the main ion in Io's ionosphere is sulphur oxide SO^+ and that the average charge number is 1.5. The atmospheric temperature at the altitude $h \simeq 50$ km (in the maximum of the F layer) is $T \simeq 900$ K.

In addition to the electric field $E_{||}$, the accelerated electrons are also affected by a resistive force due to electron–ion and electron–atom collisions. We will not take into account the electron–ion collisions, since the electric field under consideration is considerably greater than the Dreicer field, defined as [21]

$$E_{\rm d} = \frac{mv_{\rm Te}\nu'_{ei}}{e}, \quad (19)$$

where $v_{\rm Te}$ is the thermal velocity of the electrons. The corresponding equation of motion of an electron is

$$m_e\frac{dv}{dt} = eE_{||} - m_e\nu'_{ea}v, \tag{20}$$

where the effective rate of collisions between electrons and neutrals ν'_{ea} can be written

$$\nu'_{ea} = n_a S_{ea}(v)v. \tag{21}$$

The quantity v in (20) and (21) is the relative velocity of the electrons and neutrals, and $S_{ea}(v)$ is the cross section for elastic collisions of the electrons with molecules. When the electron energies are small ($W_e \lesssim 1-3$ eV), the cross section can be taken to be constant for many kinds of atoms, but this constant varies over a wide range, 5×10^{-14}–10^{-16} cm^2 for various atoms, reaching its largest values in alkali metals. On the other hand, for sufficiently fast electrons satisfying the inequality

$$v \gg \frac{e^2}{\hbar} \quad (W_e \gg 10\text{eV}), \tag{22}$$

we can use the Born approximation. In this case, $S_{ea}\sim 1/v^4$ (see, for example, [22]); i.e., the cross section decreases sharply with increasing velocity. For simplicity, we will use the following approximation for the dependence of the cross section on the velocity in our subsequent analysis:

$$S_{ea} = S_0, \quad v < v_{\rm B}, \tag{23}$$

$$S_{ea} = S_0\frac{v_{\rm B}^4}{v^4}, \quad v \geq v_{\rm B}, \tag{24}$$

where $v_{\rm B} = \frac{e^2}{\hbar} \simeq 2.2\times10^8$ cm s^{-1} and $S_0 = 5\times10^{-14}$ cm^2.

Since collisions with ions can be ignored, the electric field $E_{||}$ will accelerate the electrons of the ionosphere until the force $eE_{||}$ is balanced by the frictional force produced by the neutrals. As follows from (20), this balance is established when the electron velocity reaches

$$v_{\rm l} = \left(\frac{eVB}{2m_e n_a S_{ea} c}\right)^{1/2}, \tag{25}$$

where S_{ea} is determined by (23). For the parameters characteristic of Io's plasma environment, this velocity is $v_{\rm l} \simeq 5\times10^7$ cm s^{-1}, and exceeds the thermal velocity of the electrons in Io's ionosphere ($v^0_{\rm Te} = \sqrt{\frac{\kappa T_0}{m_e}} \simeq 1.2\times10^7$ cm s^{-1} at the electron temperature $T_0 = 900$ K). As a result, the Buneman instability will develop in the region where $E_{||}$ acts, which should considerably heat the electrons. Consequently, the number of electrons satisfying condition (22) (whose cross sections for electron–atom collisions decrease with increasing velocity) will increase considerably. In other words, heating of Io's ionosphere will generate an appreciable population of electrons in the runaway regime, which can be accelerated by the electric field (17) up to the maximum possible energy. Taking into account (17), (20), (21), and (24), we can find the threshold velocity v_* for which the runaway regime is possible:

$$v_* = \left(\frac{2cm_e n_a S_0 v_{\rm B}^4}{\text{e}VB}\right)^{1/2}. \tag{26}$$

When $n_a = 10^{10}$ cm^{-3}, $V = V_{\rm Io} \simeq 5.7\times10^6$ cm s^{-1}, and $B = 2\times10^{-2}$ G, this formula gives $v_* \simeq 10^9$ cm s^{-1}.

If the heated electrons are characterized by a Maxwellian velocity distribution with temperature T_e, the density of the runaway electrons will be described by the formula

$$n_r = \frac{n}{2}\text{erfc}(Z), \tag{27}$$

where erfc(Z) is the Fresnel probability integral, whose asymptotics at large values of the argument ($Z \gg 1$) can be written [23]

$$\text{erfc}(Z) = \frac{1}{\sqrt{\pi}Z}\exp(-Z^2). \tag{28}$$

The argument appearing in (27) and (28) is

$$Z = \frac{v_* - v_{en}}{\sqrt{2}v_{\rm T}}, \tag{29}$$

where $v_{\rm T} = \sqrt{\frac{\kappa T_e}{m_e}}$ is the thermal velocity of the heated electrons and v_{en} is the velocity shift of the electron distribution function with respect to the neutrals due to the longitudinal electric field (17), which is approximately equal to the velocity shift between the ions and electrons u that is established by the Buneman instability. Therefore, to calculate the density of the accelerated electrons, we must know $v_{\rm T}$ and u, which are determined by the kinetics of the Buneman instability.

During the development of the Buneman instability, Ohm's law can be written [24]

$$j_{||} = \frac{1}{2}\left(\frac{m_i}{m_e}\right)^{1/3}\omega_{pe}E_{||}. \tag{30}$$

Hence, assuming $j_{||} = enu$, we find the relative velocity of the motion of the electrons and ions to be

$$u = \frac{1}{2en}\left(\frac{m_i}{m_e}\right)^{1/3}\omega_{pe}E_{||}. \tag{31}$$

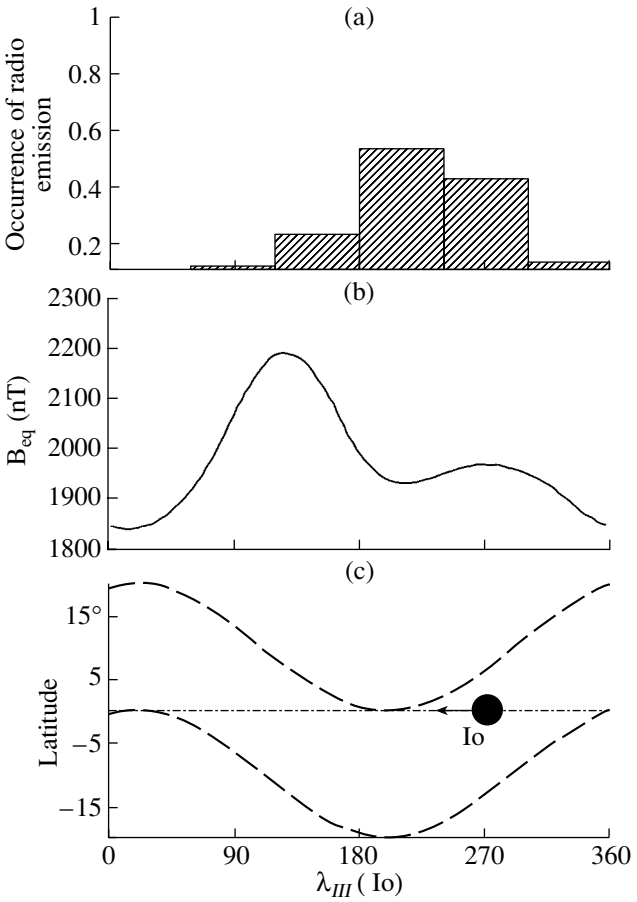

Fig. 3. (a) Probability of decameter radio emission controlled by Io as a function of Io's longitude in the λ_{III} system. (b) Magnetic-field variations along the trajectory of Io (plot taken from [11]). (c) Deviations of the plasma torus from Io's orbital plane. The torus boundaries (plotted by dashed curves) were taken at a distance of $1R_J$ from the torus center.

Using (17), we obtain the estimate $u \simeq 1.3 \times 10^7$ cm s^{-1}. The rate of electron heating can be derived from (30):

$$q_e = j_{||}E_{||} = \frac{1}{2}\left(\frac{m_i}{m_e}\right)^{1/3} \omega_{pe}E_{||}^2. \qquad (32)$$

The most efficient channel for electron cooling in Io's ionosphere is the electron thermal conductivity. The corresponding energy loss can be estimated by the formula (for more details, see [25])

$$q_T \simeq 2\frac{nT_e^2}{m_e\nu_e' L_{||}^2}, \qquad (33)$$

where $L_{||}$ is the characteristic scale for temperature variations along the magnetic field. If we assume that electron heating is compensated by cooling due to the electron thermal conductivity and that $L_{||} \sim 10^8$ cm, then relations (32) and (33) yield $T_e \simeq 3 \times 10^5$ K. Finally, we obtain the estimate of the density of runaway electrons $n_r \sim 5 \times 10^{-2}$ cm^{-3}. Further, if the energy of accelerated electrons is equal to the mean energy $\overline{E} \simeq 80$ keV and $n_r \sim 5 \times 10^{-2}$ cm^{-3}, the flux of fast electrons can be estimated to be $F_e \sim 10^2$ erg cm^{-2}s^{-1}, which corresponds to a power for the source of the accelerated electrons $P \simeq F_eS \sim 10^{11}$ W if the area of the stream cross-section is $S \sim 10^{16}$ cm^2. This power is sufficient to produce the observed electromagnetic radiation at decameter wavelengths $\sim 10^9$ W. However, we note that the density of runaway electrons depends substantially on the intensity of the magnetic field and the neutral-gas density in the acceleration region. This is associated with the strong dependence of the argument of the exponent, Z^2, on these quantities in the formula for n_r:

$$Z^2 \propto B^{-11/7}n_a. \qquad (34)$$

For example, when $n_a \sim 6 \times 10^9$ cm^{-3} and $B \simeq 1.2 \times 10^{-2}$ G [7], the density of runaway electrons will be only $n_r \sim 2 \times 10^{-5}$ cm^{-3}, which corresponds to a flux of $F_e \sim 0.05$ erg cm^{-2} s^{-1}, in agreement with the *Galileo* observations [8]. Note also that these measurements were carried out far from the region of optimal acceleration.

4. ACTIVE LONGITUDES

As was noted in the previous section, the density of accelerated electrons depends substantially on the magnetic field in the acceleration region. Variations of the magnetic field along the trajectory of Io could be associated with the presence of so-called active longitudes—specific parts of Io's orbit where the probability of decameter outbursts from Jupiter is maximum. This probability is shown as a function of Io's longitude in the λ_{III} system in Fig. 3a, which we have drawn using the data of [26].

Io rotates about Jupiter in the plane of its geographic equator, which does not coincide with the plane of its magnetic equator, since the axis of Jupiter's magnetic dipole is inclined to its rotational axis by approximately 10° in the direction of longitude $\lambda_{III} \simeq 200°$, whereas the dipole's center is shifted by $0.1R_J$ from the center of mass in the direction of longitude $\lambda_{III} \simeq 149°$ (where $R_J \simeq 71\,000$ km is Jupiter's radius) [11]. This results in a periodic variation of Jupiter's magnetic field along the orbit of Io, which is shown in Fig. 3b as a function of longitude in the λ_{III} system. In addition, for the same reason, Io is periodically immersed in the plasma torus, which is symmetric about the magnetic equator (or, more exactly, about the centrifugal equator, which

is inclined at $\simeq 7^\circ$ to the plane of the geographic equator). Figure 3c shows the deviation of the torus (in degrees) from Io's orbital plane (denoted by the solid line) as a function of longitude in the λ_{III} system. The torus boundaries (represented by dashed curves) correspond to the characteristic scale for variations in the torus density, which is $1R_J$. We can see in Figs. 3a and 3b that the probability of decameter radio bursts increases when the position of Io in its orbit ($\lambda_{III} \simeq 120^\circ$–$300^\circ$) is such that (1) the magnetic field is fairly high (1.95×10^{-2}–2.2×10^{-2} G) and (2) the electrons accelerated in the vicinity of Io can reach the northern hemisphere of Jupiter without entering Io's plasma torus.

The acceleration mechanism proposed here is consistent with these properties. The first of these can be justified by the following arguments. The increase in the magnetic field near Io should lead to an increase in the charge-separation electric field and, consequently, to an increase in the number of runaway electrons, which are in a regime of continuous acceleration. Formally, this follows from expression (34) for Z^2 and formula (27) for n_r. Since $Z^2 \gg 1$, even a small decrease in Z^2 combined with an increase in the magnetic field B results in a substantial increase in the density of the accelerated electrons. The increase in the magnetic field in the vicinity of Io from $B_{\min} \simeq 1.85 \times 10^{-2}$ G to $B_{\max} = 2.2 \times 10^{-2}$ G in the course of the orbital motion should lead to an increase in the density of runaway electrons by approximately a factor of 20. Therefore, the fluxes of fast electrons accelerated near Io will be a factor of a few greater at the active longitudes.

Next, let us consider the screening action of the plasma torus. When Io is located beyond the active longitudes, the fast electrons must cross Io's plasma torus to reach the northern hemisphere of Jupiter, where the main sources of emission controlled by Io are located. In this case, the fast electrons experience considerable pitch-angle scattering, due to either collisions with the torus particles or interactions with plasma waves and whistlers in the torus [27]. As a result, a considerable number of fast particles are scattered out of the pitch-angle interval 1.5°–2.5°, within which the electrons can reach the heights where the decameter radio emission is generated, leading to a decrease in the efficiency of generation of this emission. For example, the increment of plasma-wave excitation in the torus of Io is of the order of $\gamma \simeq \left(\frac{n_r}{n}\right)\omega_{pe} \simeq 60\ \mathrm{s}^{-1}$ when $n_r \simeq 5 \times 10^{-2}\ \mathrm{cm}^{-3}$ and $n \simeq 2 \times 10^3\ \mathrm{cm}^{-3}$ [28]. The time for the passage of the fast electrons through Io's plasma torus is $\tau \sim \frac{R_J}{v} \simeq 0.8$ s for particles with energies for their longitudinal motion $E = \overline{E} = 80$ keV. Therefore, $\gamma\tau \simeq 50$, and the fast electrons can be substantially scattered by the excited plasma waves. Note that, if the pitch-angle interval of the accelerated electrons broadens, the southward electron fluxes excited by Io at the active longitudes should be substantially attenuated when they reach the heights where the decameter radio emission is generated, providing an explanation for the fact that such emission is excited primarily in the north hemisphere.

5. CONCLUSIONS

The electron-acceleration mechanism we have considered here is based on the presence of a conductive ionosphere associated with Io and the motion of this ionosphere through Jupiter's magnetic field. Io's ionosphere has a thickness of a few hundred kilometers [10], so that the moon's motion through the magnetic field induces an electric field $\mathbf{E}_i = (1/c)[\mathbf{V} \times \mathbf{B}]$ in the ionosphere. This field generates a Hall current $\mathbf{j} \sim [\mathbf{B} \times [\mathbf{V} \times \mathbf{B}]]$ directed toward Io's surface. Since this current cannot be closed through the surface, a charge-separation electric field is formed, which has a component along the magnetic field, and this component accelerates electrons. The maximum accelerating field, on the order of $(1/2c)V_{\mathrm{Io}}B$, is formed in the upstream part of Io's ionosphere, where the magnetic field is almost parallel to the plasma layer.

The basic parameters of the resulting streams of fast electron can be summarized as follows.

—The maximum energy of the accelerated electrons is about 100 keV.

—The beams propagate in both directions along the magnetic field with approximately equal intensities [see (16) for $E_{||}$ for $\alpha > 0$ and $\alpha < 0$].

—The energy flux carried by the beams is sufficient to feed the sources of electromagnetic radiation located in regions of the Jovian magnetosphere and ionosphere that are intersected by Io's magnetic tube.

The acceleration mechanism can explain the existence of active longitudes associated with the radio emission of Jupiter, as well as the predominant location of most of these sources in the northern hemisphere: the emission probability increases sharply when Io is at longitudes $\lambda_{III}(\mathrm{Io}) \simeq 120^\circ$–$300^\circ$. This is the case when the accelerated streams of electron are increased due to the increased magnetic field in the vicinity of Io, and there is no appreciable pitch-angle scattering of the electrons moving in the northward direction due to the minimum influence of Io's torus in this case.

ACKNOWLEDGMENTS

This work was supported by the Russian Foundation for Basic Research (project codes 02-02-16239 and 01-02-17252), the Program "Nonstationary Phenomena in Astronomy" of the Presidium of the Russian Academy of Sciences, the Program OFN (Russian Academy of Sciences), the Program of Support for Leading Scientific Schools, RFFI–NNIO grant no. 02-0204005, and the Commission on International Cooperation of the Austrian Academy of Sciences.

REFERENCES

1. E. K. Bigg, Nature **203**, 1008 (1964).
2. I. Fillius, in *Jupiter,* Ed. by T. Gerels (Univ. of Arizona, Tucson, 1976; Mir, Moscow, 1979), Vol. 3.
3. D. A. van Allen, in *Jupiter,* Ed. by T. Gerels (Univ. of Arizona, Tucson, 1976; Mir, Moscow, 1979), Vol. 3.
4. L. A. Frank, K. A. Ackerson, J. H. Wolfe, and J. D. Mihalov, J. Geophys. Res. **81**, 457 (1976).
5. S. M. Krimigis and E. C. Roelot, *Physics of the Jovian Magnetosphere*, Ed. by A. J. Dessler (Cambridge Univ. Press, Cambridge, 1983), p. 106.
6. L. A. Frank, W. R. Paterson, K. L. Ackerson, *et al.*, Science **274**, 394 (1996).
7. M. G. Kivelson, K. K. Khurana, R. J. Walker, *et al.*, Science **273**, 337 (1996).
8. D. J. Williams, B. H. Mauk, R. E. McEntire, *et al.*, Science **274**, 401 (1996).
9. F. Bagenal, Geophys. Res. Lett. **24**, 2111 (1997).
10. D. P. Hinson, A. Kliore, F. M. Flasar, *et al.*, J. Geophys. Res. **103**, 29343 (1998).
11. M. H. Acuna, K. W. Behannon, and J. E. P. Connerney, *Physics of the Jovian Magnetosphere*, Ed. by A. J. Dessler (Cambridge Univ. Press, Cambridge, 1983), p. 1.
12. D. A. Gurnett, Astrophys. J. **175**, 525 (1972).
13. S. D. Shawhan, J. Geophys. Res. **81**, 3373 (1976).
14. R. A. Smith and C. K. Goertz, J. Geophys. Res. **83**, 2617 (1978).
15. F. Crary, J. Geophys. Res. **102**, 37 (1997).
16. A. F. Cheng and C. Paranicas, Geophys. Res. Lett. **25**, 833 (1998).
17. V. V. Zaitsev and A. V. Stepanov, Solar Phys. **140**, 149 (1992).
18. C. K. Goertz and A. Haschick, Planet. Space Sci. **21**, 1399 (1973).
19. S. Kumar and D. M. Hunten, *Satellites of Jupiter,* Ed. by D. Morrison (Univ. of Arizona, Tucson, 1982), p. 783.
20. M. E. Summers and D. F. Strobel, Icarus **120**, 290 (1996).
21. A. F. Aleksandrov, L. S. Bogdankevich, and A. A. Rukhadze, *Foundations of Plasma Electrodynamics* [in Russian] (Vysshaya Shkola, Moscow, 1978).
22. I. E. Golant, A. P. Zhilinskiĭ, and S. A. Sakharov, *Foundations of Plasma Physics* [in Russian] (Atomizdat, Moscow, 1977).
23. *Handbook of Mathematical Functions with Formulas, Graphs, and Mathematical Tables,* Ed. by M. Abramowitz and I. Stegun (Dover, New York, 1965; Nauka, Moscow, 1979).
24. S. A. Kaplan and V. N. Tsytovich, *Plasma Astrophysics* [in Russian] (Nauka, Moscow, 1972).
25. A. V. Gurevich and A. B. Shvartsburg, *Nonlinear Theory of Wave Propagation in the Ionosphere* [in Russian] (Nauka, Moscow, 1973).
26. F. Genova and W. Calvert, J. Geophys. Res. **93**, 979 (1988).
27. D. A. Gurnett, W. S. Kurth, A. Roux, *et al.*, Science **274**, 391 (1996).
28. V. V. Zheleznyakov, *Radiation in Astrophysical Plasmas* [in Russian] (Yanus-K, Moscow, 1997).

Translated by Yu. Dumin